POSSuMUS
A Position Sensitive Scintillating Muon SiPM Detector

Dissertation der Fakultät für Physik

der

Ludwig-Maximilians-Universität München

vorgelegt von

Alexander Ruschke

geboren in München

27.10.2014

Erstgutachter: Prof. Dr. Otmar Biebel
Zweitgutachter: Prof. Dr. Wolfgang Dünnweber

Tag der mündlichen Prüfung: 8.12.2014

Gewidmet meiner Mutter,
in Liebe und Dankbarkeit.

Abstract

The development of a modular designed large scale scintillation detector with a two-dimensional position sensitivity is presented in this thesis. This novel PO*sition* S*ensitive* S*cintillating* MU*on* S*iPM* Detector is named POSSuMUS.

The POSSuMUS detector is capable to determine the particle's position in two space dimensions with a fast trigger capability. Each module is constructed from two trapezoidal shaped plastic scintillators to form one rectangular shaped detector module. Both trapezoids are optically insulated against each other. In both trapezoids the scintillation light is collected by plastic fibers and guided towards silicon photomultipliers (SiPMs). SiPMs are light sensors which are capable to detect even smallest amounts of light. By combining several detector modules, position sensitive areas from $100\,\mathrm{cm}^2$ to few m^2 are achievable with few readout channels. Therefore, POSSuMUS provides a cost effective detector concept.

The position sensitivity along the trapezoidal geometry of one detector module is achieved by the path length dependent amount of detected light for crossing particles. The ratio of the light yields in both trapezoids is calculated. This value corresponds to the position of the particle traversing the detector. A spatial resolution in the order of several mm is foreseen. The position sensitivity along the scintillator module is determined by the propagation time of light to the SiPMs located on opposite sides of the detector. A spatial resolution of few cm is expected for this direction.

The POSSuMUS detector is applicable as large area trigger detector with a two dimensional position information of crossing particles. This is suitable in detector tests of large area precesion detectors or for measuring the small angle scattering of cosmic muons.

At the beginning of this thesis, the determination of important SiPM characteristics like the breakdown voltage is presented. In the course of this work the detector principle is proven by the test of the first prototype detector with straight tracks during an experiment at CERN. In particular, a position sensitivity in both directions is demonstrated. After this experiment the detector development focuses on the enhancement of the amount of detected light per event. Here several studies with results are presented.

The gained knowledge is realized in a second prototype detector, whereby the results of straight and inclined tracks are presented. A position sensitivity due to the trapezoidal geometry is obtained, with a spatial resolution of up to 13 mm.

This thesis concludes with an outlook on the ongoing developments and to the future use of the POSSuMUS detector.

Kurzfassung

In dieser Arbeit wird die Entwicklung eines großflächigen, ortsauflösenden Szintillationsdetektors beschrieben. Dieser modulare Detektor, genannt POSSuMUS, hat die Fähigkeit, den Ort von minimal ionisierenden Teilchen in zwei Raumrichtungen zu bestimmen. Jedes Modul besteht aus zwei trapezförmigen Plastikszintillatoren, die gemeinsam ein quaderförmiges Detektormodul bilden. Hierbei sind die beiden Szintillatoren optisch isoliert voneinander. In beiden Trapezen sind Plastikfasern eingeklebt, welche das erzeugte Szintillationslicht aufsammeln und zu Silizium-Photomultipliern (SiPMs) leiten. Diese Sensoren messen die Weglängen abhängige Lichtmenge. Silizium-Photomultiplier sind Sensoren zur Detektion kleinster Lichtmengen. Mehrere Detektor Module können zu einem großflächigen Detektor kombiniert werden, wobei eine sensitive Fläche von 100 cm^2 bis zu einigen m^2 möglich ist.

Die Ortssensitivität des Detektors entlang der Trapezgeometrie wird mittels der Weglängen abhängigen Lichtmenge bestimmt. Hierzu wird das Verhältnis der in beiden Trapezen detektierte Lichtmengen berechnet. Dieses entspricht dem Ort des hindurchfliegenden Teilchens, wobei eine Ortsauflösung im Bereich von wenigen mm angestrebt wird. In der dazu senkrechten Raumrichtung, entlang des Plastikszintillators, wird der Ort des Teilchen durch die Lichtlaufzeit im Szintillator bestimmt. Hierbei ist eine Ortsauflösung im Bereich von wenigen cm das Ziel.

Der POSSuMUS Detektor ist beispielsweise einsetzbar als Triggerdetektor mit zwei-dimensionaler Ortsvorhersage für den Test von neu entwickelten großflächigen Präzisionsdetetektoren oder zur Bestimmung der Kleinwinkelstreuung kosmischer Myonen in einem ATLAS-Teststand. Hierbei kann eine sehr große Fläche mit relativ wenigen Auslesekanälen abgedeckt werden, wodurch ein kostengünstiges System zur Verfügung steht.

Zu Beginn der Arbeit wird die Charakterisierung von Silizium-Photomultipliern beschrieben. Hierzu werden Verfahren vorgestellt, um wichtige Eigenschaften von SiPMs, wie z.B. die Durchbruchspannung, zu bestimmen. Im weiteren Verlauf der Dissertation wird im Zuge eines Experiments am CERN der Nachweis des Detektorprinzips erbracht. An dieser Stelle wird die Ortssensitivität in beiden Raumrichtungen gezeigt. Bei der Weiterentwicklung des Detektors liegt das Hauptaugenmerk auf der Optimierung der detektierten Lichtmenge pro durchfliegendem Teilchen, wobei verschiedene Studien hierzu vorgestellt werden. Deren Resultate sind in den Bau und Test eines zweiten Prototyp-Detektors eingeflossen, dessen Ergebnisse am Ende der Arbeit beschrieben werden. Dabei wird eine Ortssensitivität aufgrund der Trapezgeometrie für gerade und schräge Spuren gezeigt, mit einer Ortsauflösung im Bereich von bis zu 13 mm.

Die Arbeit schließt mit einer Zusammenfassung der Ergebnisse und einem Ausblick zur Weiterentwicklung und zum Einsatz des hier vorgestellten Detektors POSSuMUS .

Contents

Chapter 1

Introduction

1.1 The LHC, The ATLAS Detector and Small Wheel Upgrade

1.1.1 The LHC Collider

The LHC injection complex
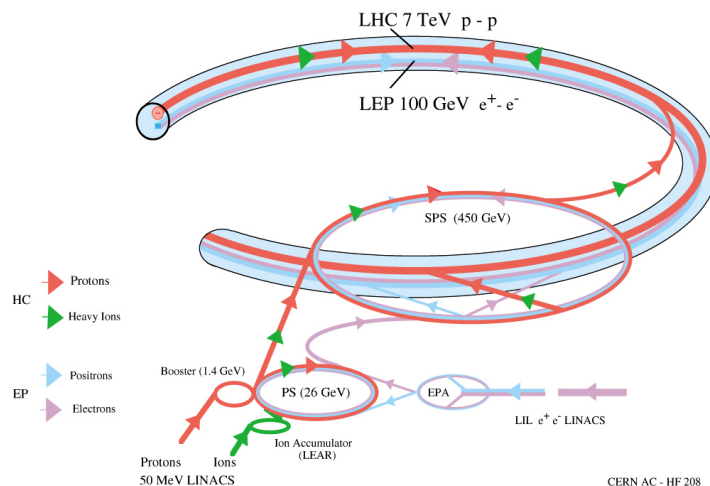
Figure 1.1: The main pre-accelerators of the LHC injection complex are the proton synchrotron (PS), and the super proton synchrotron (SPS). The LHC is proposed for proton-proton, lead-lead and proton-lead collisions. Protons can be accelerated up to a center of mass energy of $\sqrt{s} = 14$ TeV with a design luminosity of $1.0 \cdot 10^{34} \text{cm}^{-2} \text{ s}^{-1}$. Figure taken from reference [8].

The Large Hadron Collider (LHC) is located at CERN. It is installed in the former LEP tunnel with 26.7 km in circumference and up to 175 meters beneath the border of Switzerland and France. The LHC is a high energy synchrotron for either proton-proton collision, lead-lead, or proton-lead collisions.

The proton beam can be accelerated up to a center of mass energy of $\sqrt{s} = 14$ TeV with a design luminosity of $1.0 \cdot 10^{34} \text{cm}^{-2} \text{ s}^{-1}$. For lead ions the center of mass energy is $\sqrt{s} = 1150$ TeV and the design luminosity is $1.0 \cdot 10^{27} \text{cm}^{-2} \text{ s}^{-1}$. [40] [41] and [42].

The LHC started operation in 2009. During Run I the accelerator was operated at a center of mass energy of $\sqrt{s} = 7$ TeV in 2011 and at $\sqrt{s} = 8$ TeV in 2012 for proton-proton collisions. In total the maximum luminosity of $7.7 \cdot 10^{33} \text{cm}^{-2} \text{ s}^{-1}$ has been achieved.

From February 2013 until early 2015 the accelerator system is refurbished and upgraded. At the beginning of Run II a center of mass energy of $\sqrt{s} = 13$ TeV is foreseen. The luminosity will be

gradually increased to its design value. This is also valid for the center of mass energy.
In total four large detectors are installed at crossing points of the beam. These are:

- ATLAS: A Toroidal LHC AperatuS

- CMS: Compact Muon Solenoid [11]

- LHCb: LHC beauty [20]

- ALICE: A Large Ion Collider Experiment [12]

ATLAS and CMS are two large multi purpose detectors. LHCb investigates CP-violation in the B-meson sector and ALICE is optimized for investigating lead ion collisions and is focusing on the physics of strongly interacting matter at extreme energy densities. Three smaller detectors are operated close to the large detectors. These are

- TOTEM: TOTal Elastic and diffractive cross section Measurement

- LHCf: LHC forward

- MoEDAL: Monopole and Exotics Detector At the LHC

The TOTEM experiment will measure the total proton-proton cross section and study elastic scattering and diffractive dissociation at the LHC [23], LHCf detector investigates photons and neutral pions in the forward region of LHC [21], and MoEDAL searches for magnetic monopoles and other exotic particles [22]. One aim of the ATLAS detector was to complete the standard model of physics. This was achieved by the discovery of a particle in 2012 [17] and [19], that seems to be the long proposed Higgs-Boson. After fulfilling this first aim, other aspects of interest are physics beyond the standard model, determination of the top mass and more.
The investigation of the characteristics of the new found Higgs Boson and the search for new physics will start with the collection of new data at a center of mass energy of $\sqrt{s} = 13$ TeV in 2015.

1.1.2 The Atlas Detector
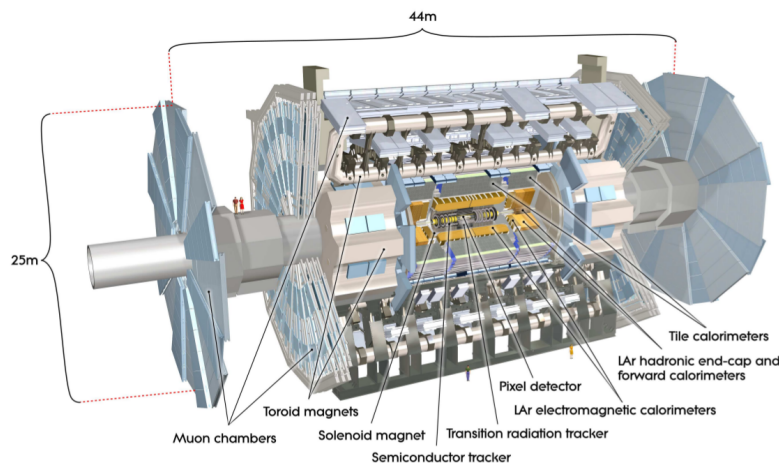
Figure 1.2: Cut away view of the ATLAS detector. The dimensions of the detector are 25 m in height and 44 m in length. The overall weight of the detector is approximately 7000 tonnes. The detector consists mainly of three subsystem, the inner tracking detector, the calorimeter and the muon system [16].

ATLAS is a multi-purpose detector with almost complete angular coverage. In Figure 1.2 a schematic drawing of the whole detector can be found. In reference [9] a complete and detailed description of all detector systems can be found.

The interaction point of protons is at the center of the ATLAS detector and is surrounded by an onionskin like structured detector with several technologies.

The detector consists of three major sub systems, namely:

- the inner tracking detector

- the calorimeter

- the muon system

The inner detector consists mainly of three components, the pixel detector (PD), the semiconductor tracker (SCT) and the transition radiation tracker (TRT).

The pixel detector is designed to provide a very fine-granular, high-precision set of measurements as close to the interaction point as possible. The system provides three of the precision measurements over the full acceptance, and determines the impact parameter resolution and the ability of the Inner Detector to find short-lived particles such as b-hadrons and τ-leptons.

The SCT system is designed to provide four precision measurements per track in the intermediate radial range, contributing to the measurement of momentum, impact parameter and vertex position, as well as providing good pattern recognition by the use of high granularity.

The TRT is based on the use of straw detectors, which can operate at the very high rates needed by virtue of their small diameter and the isolation of the sense wires within individual gas envelopes. Electron identification capability is added by employing xenon gas to detect transition-radiation photons created in a radiator between the straws [15].

The complete inner detector is enclosed in a super conducting 2 T solenoidal magnet. Therefore, the precise measurement of curved tracks from charged particles is possible and thus the determination of the momentum.

The energy of almost all crossing particles is measured by the sampling calorimeter system. It
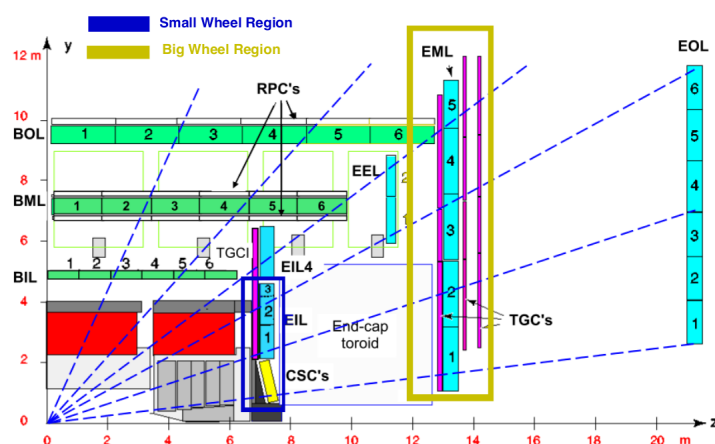
Figure 1.3: Cut through of one quarter of the ATLAS detector. The MDT-chambers are marked with green boxes in the outer Barrel region and with cyan boxes in the end cap regions for the small and big wheel regions. The yellow box illustrates the positions of the CSC-chamber. The small and big wheel are marked by blue and yellow rectangles, respectively [18].

consists of the electro-magnetic lead liquid argon and the hadronic steal scintillator calorimeter [13], [14].

The only particles that cross the inner detector and the calorimeter system are neutrinos and muons. To measure muon tracks and momenta the stand alone muon spectrometer is used. The muon spectrometer consists of Monitored Drift Tubes (MDT), Cathode Strip Chamber (CSC), Resistive Plate Chambers (RPC) and Thin Gap Chamber (TGC) trigger detectors. The momentum measurements is realized by bending the muon tracks in toroidal magnetic fields in the barrel and the two end cap regions.

The end cap muon system consists of three so called wheels:

- the small wheel, directly outside the hadronic end calorimeter

- and two big wheels at 13 m and 21 m distance from the interaction point.

This structure of the muon spectrometer is displayed in Figure 1.3.

1.1.3 New Small Wheel Upgrade

In Figure 1.4 a schedule for upcoming run and upgrade periods is presented. With the Phase I up-
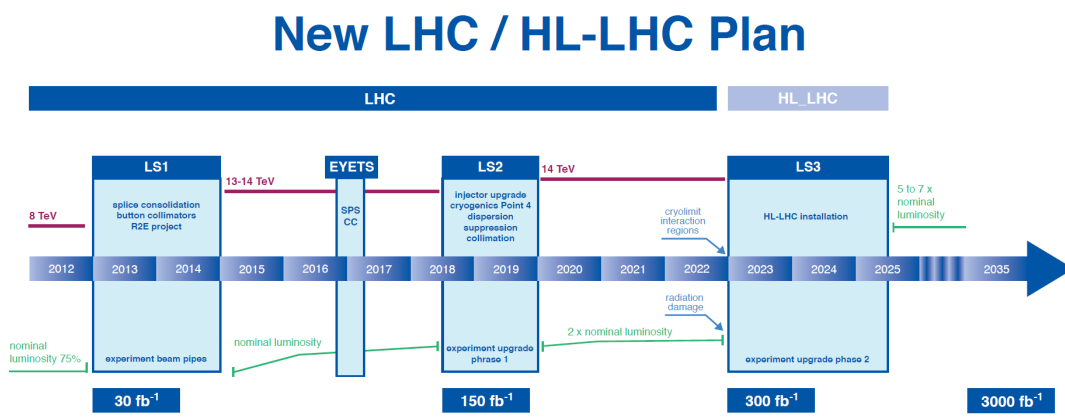
Figure 1.4: Foreseen LHC schedule, beginning with the end of RUN I in 2012 up to Long shutdown 3 (LS3) for High Luminosity LHC in the year 2025. At the moment the pre-accelerator are started after (LS 1). Early 2015 proton beam is back in the LHC for physics. Figure taken from reference [10]

grade of the ATLAS Detector before the start of RUN III, see Figure 1.4 the peak luminosity will be increased beyond the design luminosity of $1.0 \cdot 10^{34} \text{cm}^{-2} \text{ s}^{-1}$ up to instantaneous luminosity of $5.0 \cdot 10^{34} \text{cm}^{-2} \text{ s}^{-1}$. For an operation period of ATLAS for another 5-10 years after this upgrade, the accumulation of 3000 fb^{-1} of integrated luminosity is foreseen.

Due to the increased luminosity the background hit rates in the detector systems close to the interaction point and close to the beam pipe increase accordingly. The background hit rates in the muon spectrometer arise primarily from low energy photons and neutrons, whereby the background rates are both correlated and uncorrelated to triggered events. Increased background hit rates in the muon detectors in the small wheel region limit the overall ATLAS performance due to two dominant effects [18].

Firstly the efficiency decreases linearly with increasing hit rate. Moreover a high background rate also causes a degradation of the position resolution due to space charge effects [62] and [82].

Secondly, the Level 1 muon trigger in the end cap region is based on track segments in the TGC chambers of the middle muon station located in the EML (end cap middle large), see Figure 1.3. Therefore, low energy particles, mainly protons produce fake triggers by hitting the end cap trigger

chambers at an angle similar to that of real muons. In the analysis of 2012 data approximately 90 % of the muon trigger in the end caps are fake. As a consequence the rate of Level 1 muon trigger in the end cap is eight to nine times higher than in the barrel region [18].

In Figure 1.5 measured and extrapolated hit rates after the upgrade of Phase 1 are presented. The
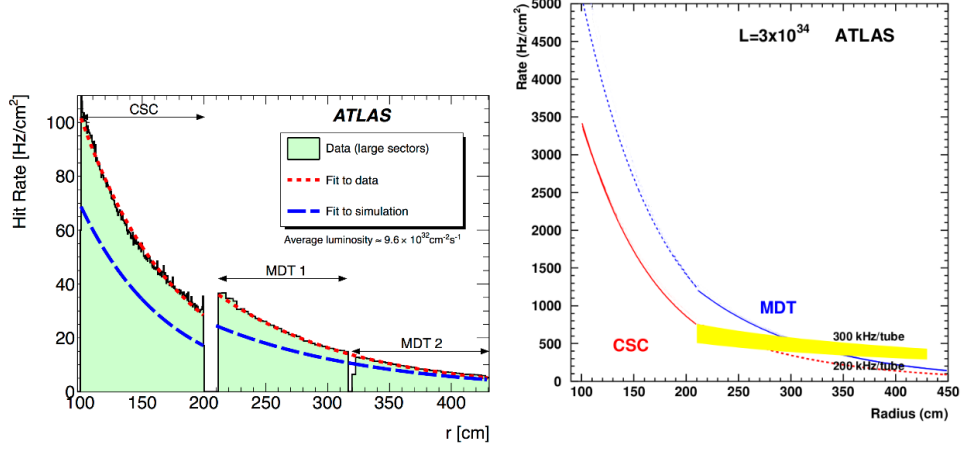
Figure 1.5: Left: Measured hit rate in the region of the Small Wheel for a luminosity of $9.6 \cdot 10^{32}$ cm^{-2} s^{-1} at $\sqrt{s} = 7$ TeV in the CSC and MDT chamber as radial distance from the beam line. Right: Extrapolated hit rate in the CSC and MDT region for a luminosity of $3 \cdot 10^{34}$ cm^{-2} s^{-1} at $\sqrt{s} = 7$ TeV as a function of the radial distance from the beam line. Also indicated is the range of tube rates of 200-300 kHz. [18]

expected rates for luminosities beyond the design luminosity distort the behavior of the currently used detectors. Hence, an upgrade with high rate capable Micromegas tracking detectors and thin gap chamber triggering detectors is foreseen. A detailed description of the new detector technologies can be found in [18].

Large area micromegas are developed and investigated in Garching. For testing and commissioning these detector the Cosmic Ray Facility (CRF), located in Garching is used. This test-facility will be upgraded and this upgrade is the topic of this thesis.

1.2 The Cosmic Ray Facility (CRF)

In Figure 1.7 a schematic of the CRF is displayed. The coordinate system is defined, so that the y-axis is in the direction of the drawing plane and the x-axis proceeds horizontally. The CRF consists of two reference chambers. Both chambers are built from 30 mm monitored drift tubes (MDT). In between the reference chambers a detector under test (DUT) is mounted to be investigated. The task of the reference chamber is to measure precisely crossing muons and provide a track prediction for the DUT. This is observable in Figure 1.6.

Above and below the reference chamber a hodoscope is installed, which triggers on traversing muons. Moreover it predicts the track of the muon with an accuracy of 3 cm in the x-direction. The lower hodoscope measures the time of the crossing muon.

The accuracy of the track prediction is limited by multi scattering of low energy muons. Therefore, above the lower trigger hodoscope an iron absorber is installed to stop muons with an energy less than 600 MeV and prevent that these muon create a trigger signal.

Below the lower hodoscope streamer tubes are installed. The streamer tubes measure the y-position of crossing muons at the lower end of the test facility with a granularity of 1 cm. The multiple scattering angle of muons in the iron absorber can be determined by the streamer tubes together with the lower
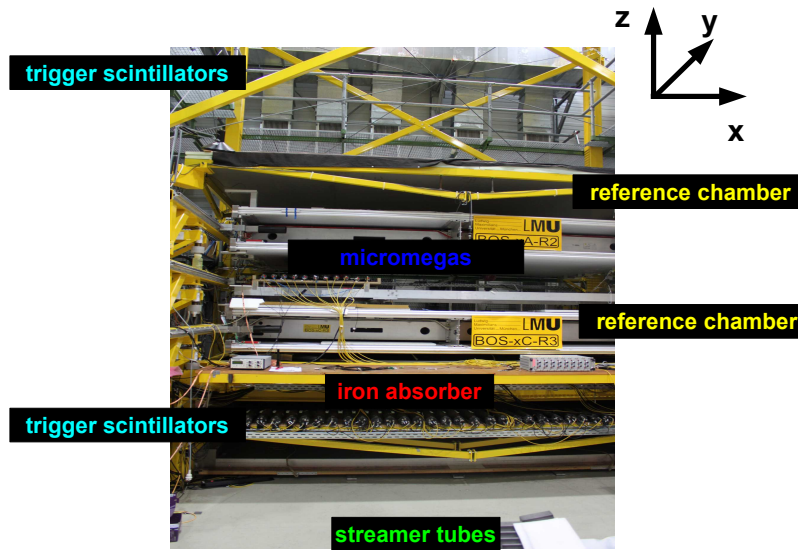
Figure 1.6: The Cosmic Ray Facility consists of two reference chambers, where in between a detector under test (DUT) is installed. Above and below the reference chambers a hodoscope is installed to indicate crossing muons. To minimize the error of multiscattering an iron absorber is installed between the lower reference chamber and the lower hodoscope. Below the iron absorber streamer tubes are installed to measure the multiscattering of muons at the iron absorber. The CRF was used for testing and commissioning of BOS-chambers for the ATLAS-experiment.

reference chambers.

From this angle and the multscattering angle at the DUT, which is measured by both reference chambers the energy of crossing muons can be estimated with a method described in reference [46]. The prediction is used for the event selection and the prediction of the error due to multiple scattering.

The CRF was used to test and for commissioning the (barrel outer small) BOS-chambers of the ATLAS experiment.

A more detailed description of the CRF can be found in reference [59].

1.2.1   Upgrade of Cosmic Ray Facility

In the future the Cosmic Ray Facility will be used for testing and commissioning large area micromegas which are foreseen for the Small Wheel Upgrade of the ATLAS Detector. The upgrade is scheduled during Long Shutdown 2 in 2018, see Figure 1.4. [18].

Therefore, an upgrade of the Cosmic Ray Facility is foreseen, where the streamer tubes, located on the ground of the test facility are replaced by a new developed large area position sensitive scintillating detector. This detector will determine the position of crossing muons in two dimensions. The detector idea is presented in Chapter 2 and the development of this detector is described in this thesis.

In Figure 1.7 a schematic for the upgraded CRF is presented. The new developed detector resides on the ground of the CRF. The task of the scintillation detector is to measure the deflection of muons, which traverse the iron absorber and provide a cut criterion for high energetic muons.

In the following an estimation for the small angle scattering of cosmic muons in the iron absorber is made.
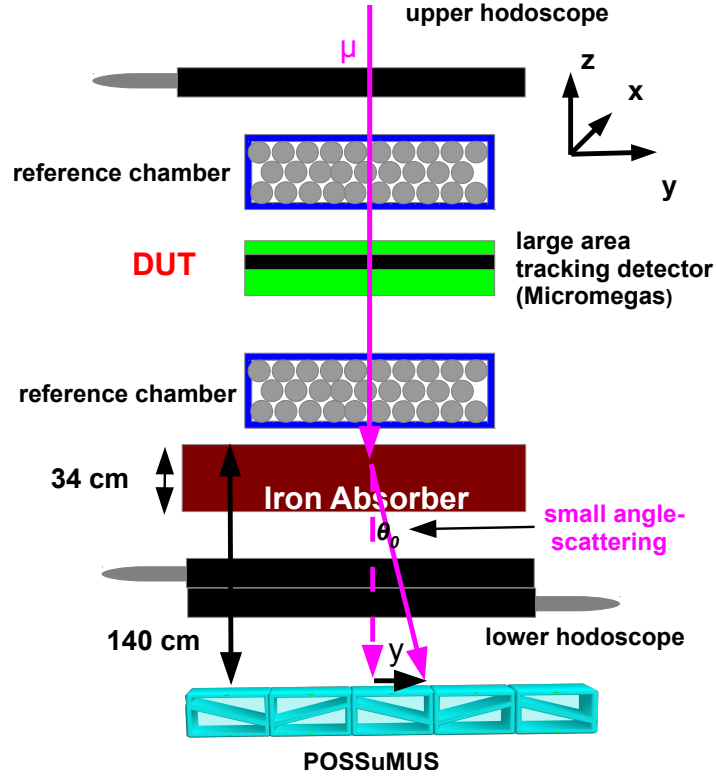
Figure 1.7: Upgrade of the Cosmic Ray Facility: A newly developed scintillation detector will replace the streamer tubes at the bottom of the test facility. This detector will be capable to determine the position of crossing particles in two space dimensions. The task of the detector is to measure the small angle scattering of cosmic muons and provide a cut criterion for high energy muons

A charged particle in a medium is deflected by many small angle scatters. Most of the deflection is due to Coulomb scattering from nuclei. The so called Coulomb scattering distribution is well represented by the theory of Molière. It is roughly Gaussian for small angle deflection. If we define the deflection angle θ_0 [57].

$$\theta_0 = \theta_{\text{plane}}^{\text{rms}} = \frac{1}{\sqrt{2} \cdot \theta_{\text{space}}^{\text{rms}}} \tag{1.1}$$

then it is usually sufficient to use a Gaussian approximation. Thus, the mean of the scattering angle is given by:

$$\theta_0 = \frac{13.6\,\text{MeV}}{\beta \cdot c \cdot p} \cdot Z \cdot \sqrt{\frac{x}{X_0}} \cdot [1 + 0.038 \cdot \ln\left(\frac{x}{X_0}\right)] \tag{1.2}$$

where p, β, c and Z are the momentum, velocity and charge number of the incident particle and $\frac{x}{X_0}$ is the thickness of the scattering medium in radiation length.

The radiation length for iron is $X_0 = 1.76$ cm [56]. Therefore Equation 1.2 can be written as:

$$\theta_0 = \frac{66.5\,\text{MeV}}{\beta \cdot c \cdot p} \tag{1.3}$$

With the assumption that the energy of the traversing muon is much larger than the mass of the muon $m_\mu = 105.6 \frac{\text{MeV}}{\text{c}^2}$ and that it travels roughly with the speed of light:

$$\beta = c = 1 \tag{1.4}$$

$$p = \sqrt{E^2 - m^2} \approx E \tag{1.5}$$

The equation 1.3 reads as follows:

$$\theta_0 = \frac{66.50 \text{ MeV}}{E} \tag{1.6}$$

For a vertical track of a cosmic muon, as indicated in Figure 1.7, the deflection due to small angle scattering can be calculated by the following relation, where the distance of the POSSuMUS detector to the iron absorber is $z \approx 140$ cm [28]

$$y = z \cdot \tan(\theta_0) = z \cdot \tan\left(\frac{66.5 \text{ MeV}}{E}\right) \cdot \text{cm} \approx 140 \text{ cm} \frac{66.5 \text{ MeV}}{E}. \tag{1.7}$$

For the last step of Equation 1.7 the small angle approximation was used. In Table 1.1 the deviation of the vertical track for different muon energies is presented.

With the derived range of deflections for different energies of cosmic muons, the requirements are

E_μ in [GeV]	≤ 1	2	3	5	6	7	8	9	≥ 10
deviation y in [cm]	9.31	4.67	3.10	2.33	1.86	1.55	1.33	1.12	0.93

Table 1.1: Deviation of incoming vertical muons, due to the small angle scattering in the iron absorber of the CRF, is presented for different muon energies, by using Equation 1.7.

given for the position sensitivity and the spatial resolution of the new developed detector.

To provide a cut criterion on the energy of cosmic muons in the range from 1 GeV to 10 GeV, based on the deflection in the iron absorber, a spatial resolution in the range of 10 mm or better is needed for both space dimensions.

Chapter 2

Detector Concept

2.1 Detector Design
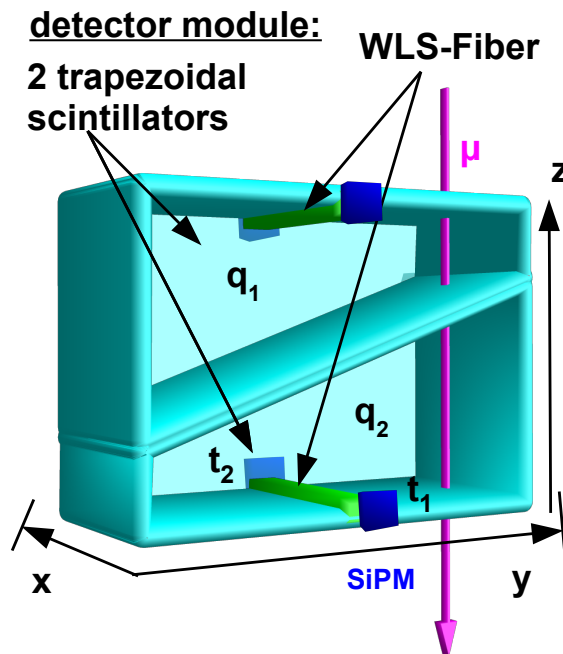
Figure 2.1: One module of the POSSuMUS-detector consists of two trapezoidal shaped scintillators. The trapezoids are optically insulated. The detector concept is to achieve a position information by path-length dependent amount of detected light. Scintillation light is collected via wave length shifting fibers and guided to a Silicon Photomultipliers.

The task of this project is to develop a scintillation detector with the capability to determine the position of crossing particles in two spatial dimensions with a fast trigger information. The **Po**sition **S**ensitive **S**cintillating **Mu**on **S**iPM detector (**POSSuMUS**) is based on a modular concept to reach large detector areas of up to several m^2 with few readout channels. It is therefore a cost effective detector.

In Figure 2.1, a sketch of one POSSuMUS module is shown. The detector consists of two trapezoidal shaped plastic scintillators (type BC 400 [32]), which are forming a rectangular rod. The trapezoids are optically insulated from each other. To collect the scintillation light, created by traversing minimal ionizing particles (e.g. cosmic muons), **w**ave-**l**ength-**s**hifting WLS-fibers (type BCF 98 [34]) are used.

One or more WLS fibers are glued into each trapezoid and guide the collected amount of scintillation light to Silicon-Photomultipliers (SiPMs). SiPMs are semiconductor devices, which are capable to measure extreme low light quantities in the range from 1 to 1000 photons. These devices are used to measure the detected amount of light.

The scintillation process and the process of wavelength shifting is described in Section 3.1 and 3.2. The functional principle and the characteristics of SiPMs are described in Section 3.3.
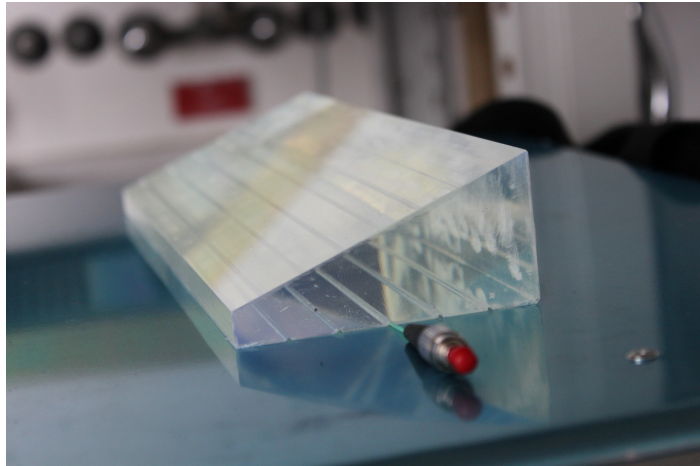
Figure 2.2: One trapezoidal plastic scintillator, is presented without wrapping: The scintillator is equipped with grooves, where the WLS-fibers are glued into.

Motivation for Trapezoidal Geometry
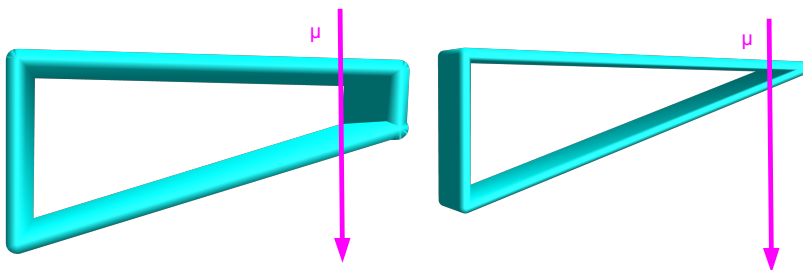
Figure 2.3: The advantage of a trapezoidal geometry compared to a triangular geometry of the scintillator arises from a sufficient long path length over the whole detector surface. Therefore, the detection of a path length dependent amount of light is possible for all tracks.

The motivation for a trapezoidal geometry of the plastic scintillators, instead of a triangular shape, is to ensure that the detection of a path length dependent amount of light is possible for the whole scintillator surface, see Figure 2.3. For the triangular shape the path length within the scintillator becomes zero at the thin side and the detection of a particle is not possible.

Position Sensitivity in the Transverse Direction (y)

In the transverse direction (y), along the trapezoidal geometry (see Figure 2.1), the position sensitivity for traversing particles is determined due to the geometric shape of both scintillators. The vertical traversing particle in Figure 2.1 creates a path length dependent amount of scintillation light in each scintillator, where $q_1(y)$ and $q_2(y)$ are the detected amounts of light in the upper and in the lower trapezoid.
The position of crossing particles is determined by the normalization of the detected amount of light $q_1(y)$ in the upper trapezoid, by the sum of detected amounts of light in the upper and in the lower lower trapezoid. This light ratio is:

$$\text{pos(y)} \; = \; \frac{q_1(y)}{q_1(y) + q_2(y)} \tag{2.1}$$

This idea is also applicable for inclined tracks of traversing particles, which are not shown in Figure 2.1.

Position Sensitivity in the Longitudinal Direction (x)

In the longitudinal direction (x), along the scintillator, (see Figure 2.1) the position of crossing particles is determined by the propagation time of light within the scintillator. The SiPMs are located at both front sides of the trapezoid and connected to the ends of a WLS-fiber. Both SiPMs determine the starting point of the light response for each side t_1 and t_2. By calculating the time difference of both starting points a position information for the traversed particle is achieved for the longitudinal direction. This is described by the following Equation 2.2.

$$\text{pos(x)} \propto \; t_1 \; - \; t_2 \tag{2.2}$$

Large Area Detector
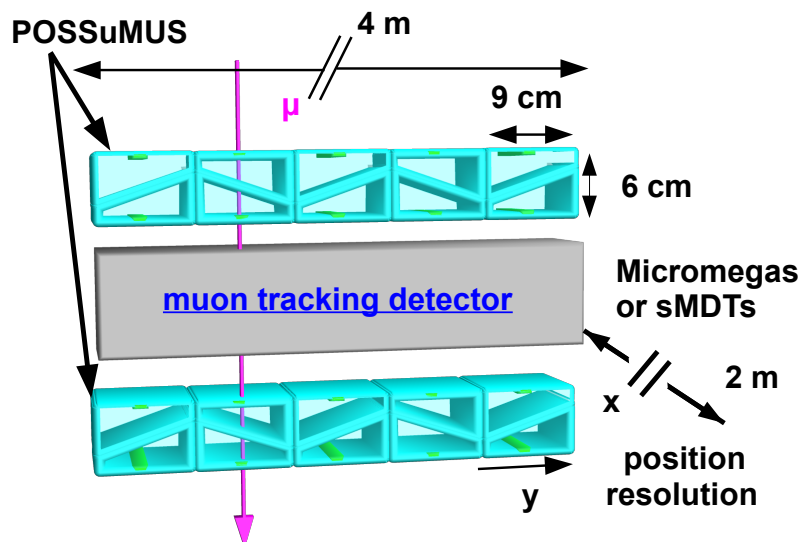
Figure 2.4: The modular concept of POSSuMUS is realized by combining several scintillator modules to cover areas in the order of m^2. Thus, a POSSuMUS detector, consisting of several modules above and below a large area micromegas detector can provide a fast trigger information and a two-dimensional position information.

To cover large areas, several modules are combined to form a large area detector of several m², see Figure 2.1. Each module consists of two trapezoidal shaped scintillators with a length of 2 m. In Figure 2.4 a sketch for an application of the large area detector is displayed. The modular POSSuMUS detector can be used for example to cover new developed large area micromegas [43]. POSSuMUS provides a fast trigger information, which is feasible by the scintillation process. Besides the trigger information, POSSuMUS provides a position information in two spatial dimensions.

A second application for the detector concept has already been discussed in Section 1.2. Here the position sensitivity of the detector can be used to determine the deflection of cosmic muons at an iron absorber by the small angle scattering. The aim is to provide a selection criterion for cosmic muons in an energy range from 600 MeV to 10 GeV.

The envisaged spatial resolution for the longitudinal-coordinate (x) due to the propagation time of light is about 5 cm. For the transverse-coordinate (y) the required spatial resolution is about 5 mm due to the light ratio in both trapezoids. The fast trigger capability is already accomplished by using a scintillating detector, where the time spread is in the order of ns.

2.1.1 Limitation for the Spatial Resolution of POSSuMUS

Energy Loss Distribution for Thin Absorbers
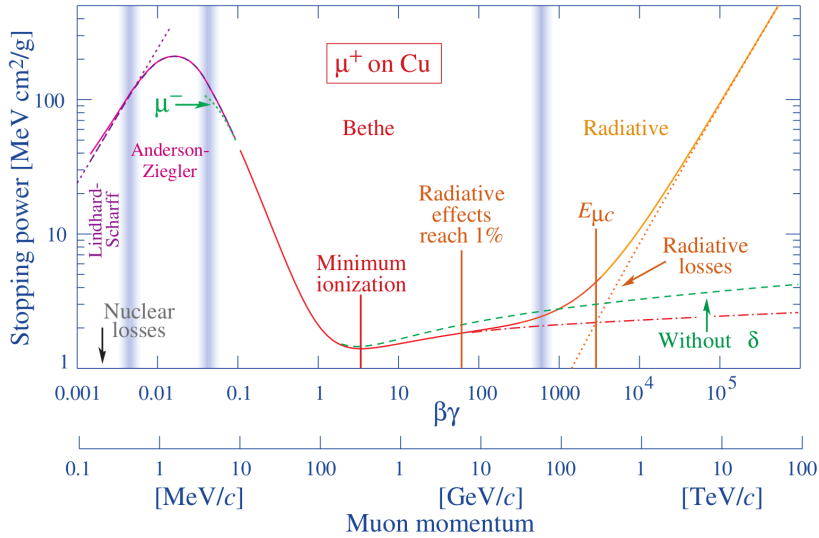
Figure 2.5: Stopping power ($\langle \frac{dE}{dx} \rangle$) for positive muons in copper as a function of ($\beta \cdot \gamma = \frac{p}{Mc}$) over nine orders of magnitude in momentum. Solid curves indicate the total stopping power. Figure taken from reference [57].

The interaction of particles and photons with matter is described by the Bethe Bloch formula. In the calculation the energy transfer is parametrized in terms of momentum transfer. In Equation 2.3 the Bethe Bloch formula is presented, whereby two correction, the shell correction [4] and the density correction [76], are added.

$$-\frac{dE}{dx} = 2\pi \, N_A \, r_e^2 \, m_e c^2 \, \rho \, \frac{Z}{A} \frac{z^2}{\beta^2} \left[\ln \left(\frac{2m_e \, c^2 \, \beta^2 \, \gamma^2 \, W_{max}}{I^2} \right) - 2\beta^2 - \delta - 2\frac{C}{Z} \right] \qquad (2.3)$$

with:

r_e : classical electron radius m_e : electron mass

ρ : density of absorbing material,   z: charge of incident particle

N_A = Avogadro number β : velocity of incident particle

I: mean excitation energy δ : density correction

Z: atomic number of absorbing material   C: shell correction

A: atomic weight of absorbing material γ = Lorentzfactor

W_{max} = maximum energy transfer in a single collision

The maximum energy transfer is that produced by head on or knock on collisions. For an incident particle of mass M, kinematics gives:

$$W_{max} = \frac{2\,m_e\,c^2\eta^2}{1 + 2s\sqrt{(1 + \eta^2)} + s^2} \tag{2.4}$$

whereby s $= \frac{m_e}{M}$ and $\eta = \beta\gamma$.

In Figure 2.5 the stopping power ($\langle\frac{dE}{dx}\rangle$) for positive muons in copper is displayed as a function of ($\beta \cdot \gamma = \frac{p}{Mc}$) over nine orders of magnitude in momentum, whereby solid curves indicate the total stopping power.

The POSSuMUS detector is proposed for traversing minimum ionizing particles (MiPs), like muon or pions with a ($\beta \cdot \gamma$) between 1 and 10.

In the following the energy loss distribution is discussed for the case of thin absorbers, where the number of collisions N is too small for the Central Limit Theorem to be applied and therefore the distribution is not Gaussian shaped. For heavy particles W_{max} is kinematically limited to the expression given in Equation 2.4, while for electrons as much as one half of the initial energy can be transferred. In the latter case, there is also the possibility of a large energy loss from bremsstrahlung. While these events are rare, their possibility adds a long tail to the high energy side of the energy loss probability distribution, which is displayed in Figure 2.6. Note that the mean energy loss no longer corresponds to the peak but is displaced because of the high energy tail. In contrast, the position of the peak now defines the most probable energy loss [48].
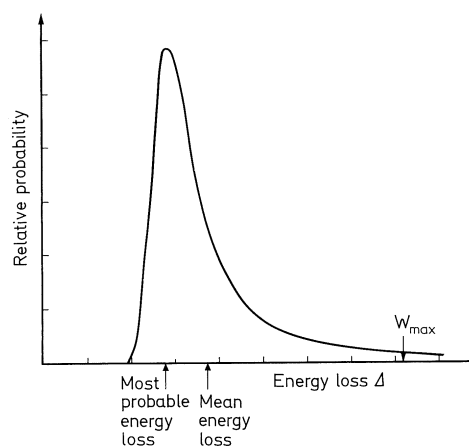
Figure 2.6: Typical distribution of energy loss in a thin absorber. It is asymmetric with a long high energy tail. Figure taken from reference [48].

Basic theoretical calculations of this distribution have been carried out by Landau, Syman and Vavilov. To distinguish several theoretical descriptions of energy losses in thin absorbers, a parameter

$$\kappa = \frac{\Delta E}{W_{max}} \tag{2.5}$$

is introduced, where ΔE is the mean energy loss in the detector and W_{max} is the maximum energy transfer allowed in a single collision [48]. Absorbers with $\kappa < 10$ are classified as thin, the Landau theory is applicable for $\kappa \lesssim 0,05$. Details about the theoretical descriptions can be found in references [47] and [64].

2.1.2   Limitation of the Spatial Resolution in the y-Direction

In the following section, two aspects are discussed which limit the spatial resolution of the POSSuMUS detector in the y-direction. The influence of both aspects are not investigated in detail in this thesis, but both are worth to be discussed for the ongoing development of the detector.

Systematic Error of the Spatial Resolution in y-Direction
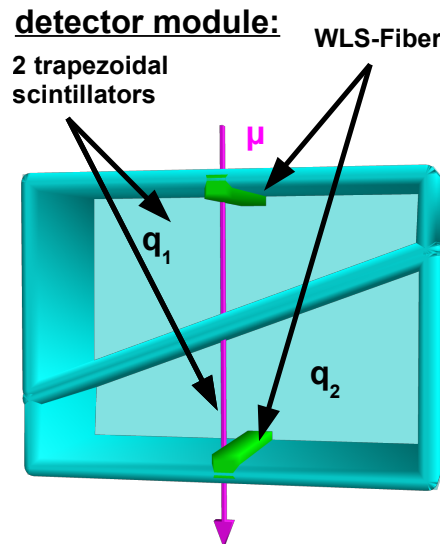
Figure 2.7: The PoSSMUS detector is shown with a traversing muon in the center of the detector, therefore the path length and the detected amount of light in both trapezoids are equal. In the following two limitations for the spatial resolution are discussed. Firstly, the influence by the asymmetric energy loss of minimum ionizing particles and secondly the statistical error which arises from the number of detected photons per event.

A systematic error on the spatial resolution of the POSSuMUS detector arises due to the above described Landau like energy loss of minimum ionizing particles in the scintillator, which is shown in Figure 2.6.

Assume, that a cosmic muon crosses the detector at the central position, as indicated in Figure 2.7. The path length of the muon is equal in both scintillators. If all other influences such as light absorption or statistical variation in the amount of detected light are neglected, the amounts of detected light in both trapezoids ($q_1(y)$ and $q_2(y)$) are equal, too. Therefore, the light ratio pos(y) results in:

$$\text{pos(y)} = \frac{q_1(y)}{q_1(y) + q_2(y)} \underbrace{=}_{q_1(y)=q_2(y)} \frac{q_1(y)}{2 \cdot q_1(y)} = \frac{1}{2} \tag{2.6}$$

In the following, the influence of the asymmetric energy loss of minimum ionizing particles is discussed for two extreme cases. If the energy loss in the upper scintillator is at the most probable value of the distribution and the energy loss in lower scintillator is at the high energy tail, see Figure 2.6, the amount of detected light in both trapezoids differs, $q_1(y) < q_2(y)$, despite of equal path lengths in both scintillators. Therefore, the light ratio pos(y) results in:

$$\text{pos(y)} = \frac{q_1(y)}{q_1(y) + q_2(y)} \underbrace{=}_{q_1(y)<q_2(y)} \frac{q_1(y)}{q_1(y) + q_2(y)} < \frac{1}{2} \tag{2.7}$$

For another crossing muon the energy loss is at the high energy tail for the upper trapezoid and at the most probable value for the lower trapezoid, then the light ratio pos(y) reads like:

$$\text{pos(y)} = \frac{q_1(y)}{q_1(y) + q_2(y)} \underbrace{=}_{q_1(y)>q_2(y)} \frac{q_1(y)}{q_1(y) + q_2(y)} > \frac{1}{2} \tag{2.8}$$

Therefore, the asymmetric energy loss of minimum ionizing particles systematically broadens the light ratio distribution pos(y).

Statistical Error on the Spatial Resolution in y-Direction

A second aspect which determines the spatial resolution of the detector is the detected number of photons per event. In the following, the error of the light ratio pos(y) is estimated, again for a traversing muon in the center of the detector, where the path lengths are equal in both trapezoids, as indicated in Figure 2.7. For this estimation, q_1 and q_2 are the number of detected photons in the upper and lower trapezoids. Moreover, a symmetric energy loss in both trapezoids is assumed and the error of the spatial resolution due to the photon statistics is calculated applying the Gaussian error propagation to the light ratio.

$$\text{light ratio}: \quad \text{pos}(q_1, q_2) = \frac{q_1}{q_1 + q_2}, \tag{2.9}$$

which gives:

$$(\Delta \text{pos}(q_1, q_2))^2 = \left(\frac{\delta \text{pos}}{\delta q_1}\right)^2 \cdot (\Delta q_1)^2 + \left(\frac{\delta \text{pos}}{\delta q_2}\right)^2 \cdot (\Delta q_2)^2 \tag{2.10}$$

Assuming $\Delta q_1^2 = \Delta q_2^2$ results in:

$$(\Delta(\text{pos}(q_1, q_2))^2 = \frac{(q_1)^2 + (q_2)^2}{(q_1 + q_2)^4} \cdot (\Delta q_1)^2 \tag{2.11}$$

For muons traversing the center of the detector and i.e. for equal light yields in both trapezoids ($q_1 = q_2$) and $\Delta q_1 = \sqrt{q_1}$ one gets:

$$\frac{(\Delta \text{pos}(q_1, q_2))^2}{(\text{pos}(q_1, q_2))^2} = \frac{1}{q_1 + q_2} = \frac{1}{N} \tag{2.12}$$

whereby N is the number of photons detected by the detector. The error of the light ratio pos(y) is given by:

$$\text{poserr}(q_1, q_2) = \frac{\Delta \text{pos}(q_1, q_2)}{\text{pos}(q_1, q_2)} = \frac{1}{\sqrt{N}} \tag{2.13}$$

In Table 2.1, the statistical error on the light ratio is presented for different amounts of detected photons. The number of detected photons per event is one important property which determines the spatial resolution. Therefore, maximizing the amount of detected light per event is crucial to improve the spatial resolution.

detected photons (N)	10	20	30	60	100	200
$\mathrm{poserr}(q_1, q_2) = \frac{1}{\sqrt{N}}$	0.32	0.22	0.18	0.13	0.10	0.07

Table 2.1: For muons traversing the center of the detector and equal path length and energy loss in both trapezoids, the error for the light ratio pos(y) is presented for different amounts of detected photons. The error decreases with increasing amount of detected photons.

2.1.3 Limitation of the Spatial Resolution in x-Direction
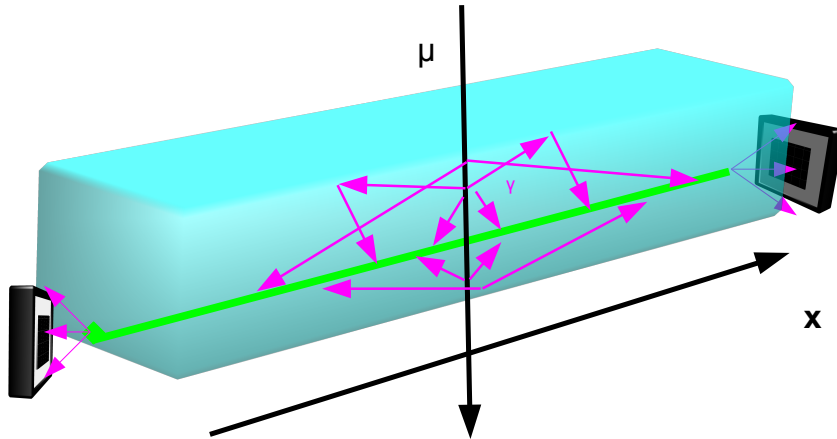
Figure 2.8: A rectangular scintillator module is presented with a WLS-fiber and two SiPMs located at opposite sides of the scintillator. A muon traverses the scintillator and creates photons on its track through the detector. The position sensitivity along the scintillator (x-direction) is achievable by the propagation time of light. The main limitation of the spatial resolution arises due to the collection of the scintillation light by the WLS fiber, as it is not predictable where the created photons are collected by the fiber, either close to the track of the muon or further away, as indicated in this schematic.

To discuss the limitation of the spatial resolution in x-direction, a rectangular scintillator with a WLS-fiber and two SiPMs is presented in Figure 2.8. A muon traverses the scintillator and photons are emitted isotropically along its track. The position sensitivity along x-direction is achieved by the propagation time of light.

The photons are created in the scintillator and collected by WLS-fibers and then guided to the SiPMs. The main limitation for the spatial resolution in x-direction arises from the propagation of the photons in the scintillator, which may not always travel directly to the WLS fibers, as indicated by the **magenta** arrows in Figure 2.8. The light can thus be collected by the WLS-fiber at a position close or far away from the actual muon track. The light collected by the WLS-fiber can either be close to the position of the muon or far away. This effect is more pronounced, if the detected number of photons is small due to the small area of the WLS-fiber in comparison to the whole scintillator volume.

Other limitations for the spatial resolution in x-direction are the time for absorption and remission of photons in the WLS-Fiber and the time resolution of the SiPM.

Chapter 3

Scintillation Process and Semiconductor Devices

3.1 Scintillation Process in Organic Materials

In this section, the origin and the principal features of scintillation in organic systems is presented. Luminescence, the emission of light with a characteristic spectrum is a property associated with conjugated and aromatic organic molecules.

These organic molecules form molecular crystals in which the molecules are loosely bound together by van der Waal forces and retain their individual identity, electronic structure and luminescence. The configuration of the C-atom is a sp^2 hybridization, where one of the original p-orbitals (p_z) is unchanged and three equivalent hybrid orbitals are produced by mixing s, p_x, p_y.

These three sp^2 hybrid orbitals lie in the same plane (x-y-plane) and are inclined at equal angles of
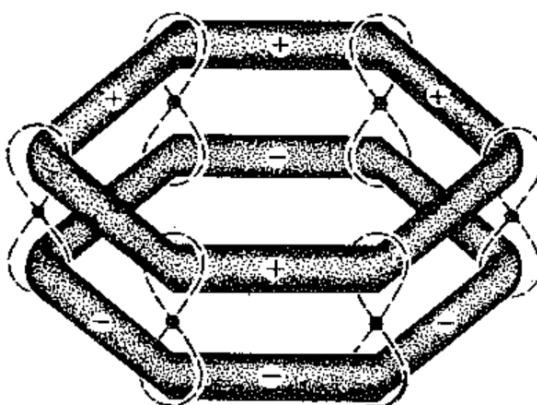
Figure 3.1: Schematic of the orbital structure of Benzene C_6H_6. The σ hybrid orbitals produce the localized C-H and C-C σ bonds. The six π atomic orbitals interact to produce a common nodal plane, that of the molecule. Figure taken from reference [5].

$120°$ to each other. It is this configuration which provides the hexagonal ring structure of benzene and the polycyclic aromatic hydrocarbons, which are also planar molecules. The hybrid orbitals which are symmetrical about their bonding axis and about the plane of the molecule are known as σ electrons and the bonds are called σ bonds. The unchanged p_z atomic orbital is mirror symmetric about the nodal x-y plane and is known as π orbitals.

The simplest compound containing trigonal hybridized carbon is ethylene C_2H_4. The σ orbitals provide the C-H and C-C σ bonds, which are at $120°$ to each other. In addition the two π orbitals

interact, achieving maximum interaction when their nodal planes are co-planar, producing an additional C-C-bound, known as π bond

In benzene C_6H_6, see Figure 3.1, the σ hybrid orbitals produce the localized C-H and C-C σ bonds. The six π atomic orbitals interact to produce a common nodal plane, where the π electrons are completely delocalized. Similar systems of delocalized π electrons occur in other aromatic and conjugated molecules like anthracene $C_{14}H_{10}$ or Polyvinyl-toluene $C_{27}H_{30}$, and it is the excited states of these π electron systems which are responsible for the luminescence [5]. Energy levels for
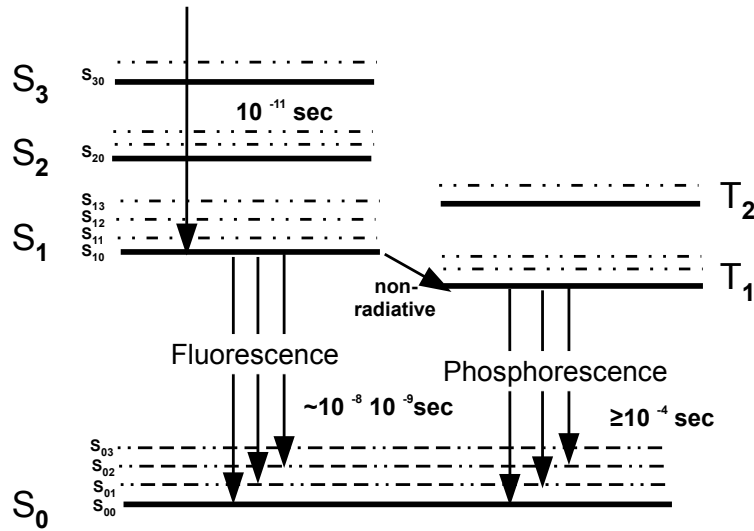
Figure 3.2: Fluorescence corresponds to a radiative transition from S_1 to S_0 after absorption. It is the fast component of the luminescence with a typical lifetime 10^{-11} s. The triplet states of π electrons can be populated by various means such as recombinations and non radiative conversion. The phosphorescence is constituted by the slow transition ($\geq 10^{-4}$ s) from T_{10} to S_{0x}. Figure taken from [81].

π electrons in an organic molecule are represented schematically in Figure 3.2. Each principal level S_{i0}, is accompanied by vibrational sub levels S_{ij}. The first principal level is usually a few eV above the singlet ground state S_{00}. The vibrational levels have a spacing of typically 0.16 eV. There is also a sequence of excited π electron triplet states with their vibrational levels, but lower in energy, than the corresponding singlet states.

The fast emission of scintillation light when a photon or a charged particle passes through an organic scintillator eventually results from excitation of electrons in the ground state to the higher singlet states, see Figure 3.2. Thermal equilibrium is rapidly established in 10^{-11} s populating predominately the lowest electronic state at normal temperature. Then the radiative transition form S_{1x} to S_{0x} occurs with a typical lifetime of 10^{-8} s to 10^{-9} s. This scintillation light is called fluorescence. The intensity of the fluorescence emission decays exponentially with time according to,

$$I = A \cdot \exp(-t/\tau) \tag{3.1}$$

where A and I are the intensities at $t_0 = 0$ and t respectively and τ is the fluorescence decay time, This fluorescence is modified by absorption in the material and possible re-emission by other substances dissolved in the medium, which constitutes the scintillation light in efficient organic scintillators.

The triplet states of π electrons can be populated by various means such as recombination and
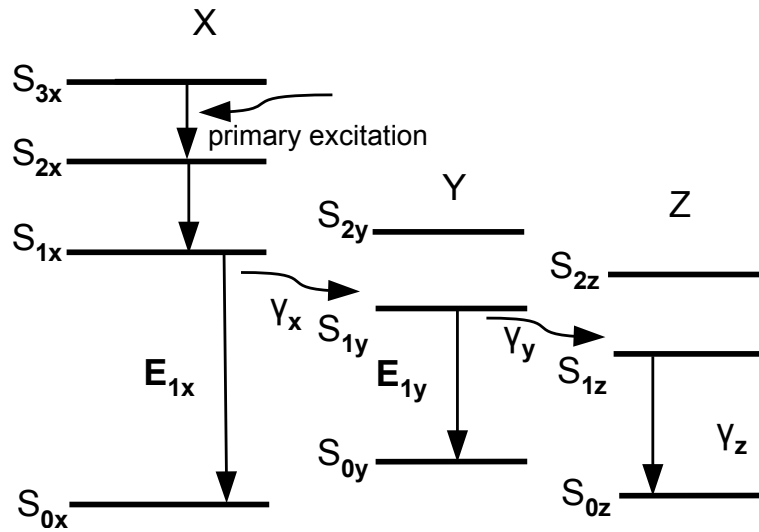
Figure 3.3: Scintillation Process with a solvent with two solutes: The resulting primary fluorescence γ_x is absorbed by the solute Y, itself an organic scintillator which is excited to some state S_{iy}. The secondary fluorescence γ_y from the $S_{1y} \rightarrow S_{0y}$ transition is then wave-length-shifted by the second solvent Z, leading to the final emission γ_z which is detected by an external photoelectric device, e.g. a SiPM. Figure taken from reference [81].

non radiative conversion. Slow transition ($\geq 10^{-4}$ s) from T_{1x} to S_{0x} constitutes phosphorescence. Therefore, the intensity can be described by a two component exponential decay:

$$I = A \cdot \exp(-t/\tau_f) + B \cdot \exp(-t/\tau_s) \tag{3.2}$$

Where τ_f is the decay time of the fluorescence and τ_s is the decay constant of the phosphorescence and A and B are the emitted photons for each process. [48]

In addition, electrons in triplet states may acquire sufficient thermal energy to return eventually to S_1. This produces the 'delayed fluorescence', characterized by a non-exponential period of $\geq 10^{-6}$ s and an intensity of 10 % of the fast component [81].

Practical solid organic scintillators are currently made of plastic. The main emission of fluorescence and phosphorescence in organic scintillators is in the ultra-violett region, where the transparency of those organic materials is low. Therefore, further organic solvents are solved in the scintillator which are used as wavelength shifter. For an optimal adaption to the spectral sensitivity of, for example Silicon photomultipliers, several solvents are included in the scintillator.

The scintillation process for such a solution of at least three components is shown in Figure 3.3. Since the solute concentrations are rather small ($\leq 1\%$) energy loss by incident particles excites mainly molecules of the solvent X. The resulting primary fluorescence γ_x is absorbed by the solute Y, itself a organic scintillator which is excited to some state S_{iy}. The secondary fluorescence from $S_{1y} \rightarrow S_{0y}$ transition γ_y is then wave-length-shifted by the second solvent Z, leading to the final emission γ_z which is detected by an external photoelectric device. The solvent is usually an aromatic vinyl polymer, like Polyvinyltoluene $C_{27}H_{30}$ with solutes, like POPOP (2,2-p-phenyle in toluene), and their concentration is chosen to optimize the ratio of the useful light out to the energy lost by the incident radiation [81].

The first π-singlet excitation energy E_{1y} must be lower than E_{1x}, so that absorption of any primary
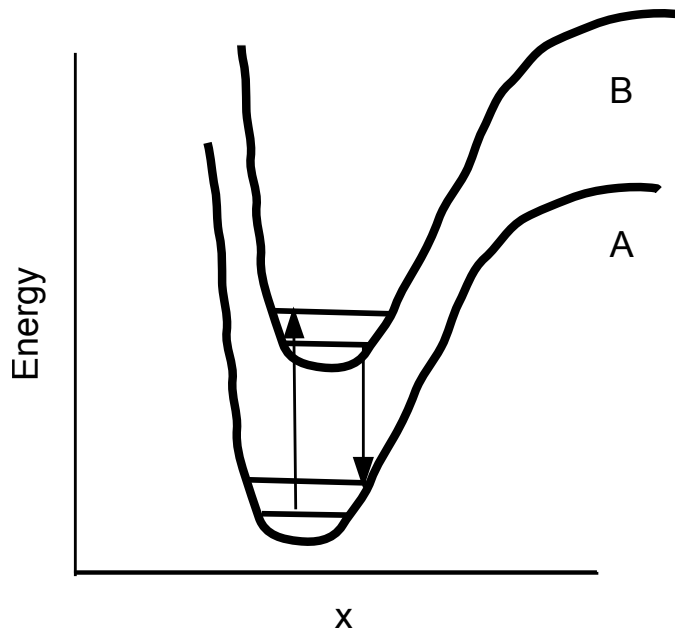
Figure 3.4: Frank Condon Principle: The excitation of the center by the absorption of a photon is shown by the transition upward from the ground state. The subsequent decay of the state occurs after thermal dissipation of energy to neighboring atoms. Thermal losses continue after the transition, bringing the center back to the bottom of the ground state A. Clearly the emission spectrum is on average of longer wavelength than the absorption spectrum. Figure taken from [81].

fluorescence can eventually leave a solvent molecule with excitation energy E_{1y}. Similarly the absorption spectrum of Z must overlap that of Y with the added requirement that the emission spectrum of Z needs to be matched to a suitable external photon detecting device.

Wavelength-shifters like POPOP absorb light with a shorter wavelength and emit it with a longer wavelength. This effect can be explained by the Frank Condon principle with reference to the Stoke shift [52], displayed in Figure 3.4.

To gain insight into the mechanism the simple model shown in Figure 3.4 can be used. Here the potential energies of the ground state A and the first excited electronic state B of a luminescence center are shown as a function of some position coordinate with respect to the center. Some vibrational levels are shown in each electronic state, though they usually merge into one band. The excitation of the center by the absorption of a photon is shown by the transition upward from the ground state. The subsequent decay of the state occurs after thermal dissipation of energy to neighboring atoms. Thermal losses continue after the transition bringing the center back to the bottom of the ground state A. Clearly the emission spectrum has longer wavelength than the absorption spectrum, with the extend of overlap depending on details of the potential energy curves. In the region where the curves are close to another complete de-excitation can take place non-radiatively and this internal quenching process competes with the emission of light [81]. The magnitude of the wavelength shift is known as Stokes-shift [52] and is given by:

$$E_{shift} = \frac{1}{2} \cdot \left(E_{absorption} - E_{emission} \right) \tag{3.3}$$

In Figure 3.5, the emission spectrum of the plastic scintillator BC 400 is shown, this kind of scintillator is used for the realization of the POSSuMUS-detector. A selection of properties for this scintillator is presented in Table 3.1.

Emission Spectra

BC-400
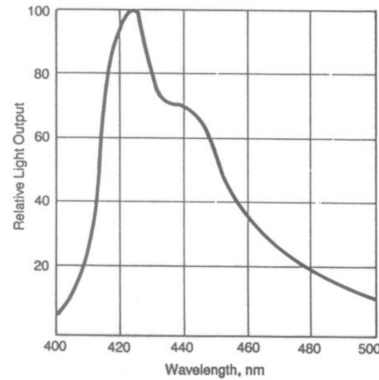
Figure 3.5: Emission spectrum of the plastic scintillator BC 400: The peak emission is in the range of blue wavelength of 423 nm. The emitted photons fit to the absorption spectrum of the WLS-fiber, see Figure 3.7. Figure are taken from reference [32].

Light Output Anthracene %	Wavelength of Maximum Emission, [nm]	Decay Constant Main Component, [ns]	Refractive Index	H:C Ratio
65	423	2.4	1.58	1.103

Table 3.1: A selection of properties for the scintillator BC400 used to construct the POSSuMUS detector. The maximum emission wavelength is at 423 nm and the refractive index is at 1.58. Data are taken from [32].

3.2 Wavelength Shifting (WLS) Fiber
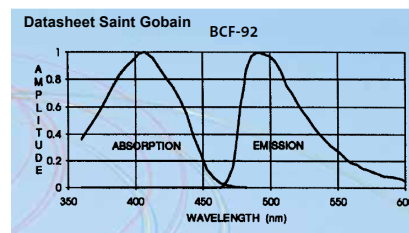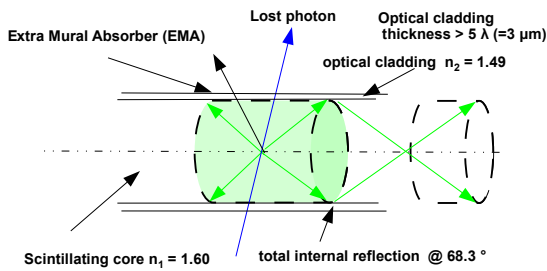
Figure 3.6: The principle structure of a WLS-fiber is presented: The scintillating core material is clad with a non-scintillating material of lower refractive index, which is at least several wavelengths thick. This in turn may or may not be surrounded by a thin opaque extra mural absorber (EMA) [34] and [81].

Figure 3.7: Absorption and emission spectrum of the WLS-fiber BCF-92. The absorption spectrum fits to the emission spectrum of the plastic scintillator BC 400 used in the POSSuMUS detector, see Figure 3.5. Figure taken from reference [34].

In Figure 3.6 the principle structure of a wavelength-shifting fiber (WLS) is shown. The scintillating core material is clad with a non-scintillating material of lower refractive index, which is at least

several wavelengths thick. This in turn may or may not be surrounded by a thin opaque extra mural absorber (EMA).

The refractive indices are such that the fraction of scintillator light trapped by a fiber is only a few percent. So most scintillation light leaks out and this can scatter or lead to further excitation. For this reason the EMA is essential for fibers which track charged particles. The scintillation light is emitted isotropically within the fiber [81].

In Figure 3.7, the absorption and emission spectra of the WLS fiber, type BCF-92 [34] are shown. The absorption spectrum of the fiber matches to the emission spectra of the plastic scintillator BC 400, see Figure 3.5, and can therefore collect the created scintillation light by minimal ionizing particles within the scintillator and guide it to a photon detection device.

For the POSSuMUS-detector WLS-fiber are essential to collect the path length dependent amount of light and guide it to the SiPMs, where the light yield is measured. In Table 3.2 a collection of properties is presented for the WLS-fiber BCF-92, used in the POSSuMUS detector.

Emission color	Wavelength of Max. Emission [nm]	Decay time [ns]	Absorption Length [m]	Wavelength of Max. Absorption [nm]
green	492	2.7	> 3.5	405

Table 3.2: A selection of properties for WLS fiber BCF-92 used in the POSSuMUS detector is presented. The maximum emission wavelength is at 492 nm and the absorption length is larger than 3.5 m. Data are taken from reference [34].

3.3   Silicon Photomultiplier (SiPM)

3.3.1   Theory of Semiconductors

Energy Band Structure

Semiconductors are crystalline materials, whose outer shell atomic levels exhibit an energy band structure. Figure 3.8, schematically illustrates this basic structure consisting of a valence band, a forbidden energy gap, and a conduction band. The energy bands are originally regions of many discrete levels which are spaced closely enough to be considered as a continuum, while the forbidden energy gap is a region in which there are no available energy levels at all. This band structure arises because of the close, periodic arrangement of the atoms in the crystal which causes an overlapping of the electron wave functions. Since the Pauli principle forbids more than one electron in the same state, the degeneracy in the outer atomic shell energy levels breaks and many discrete levels are formed only slightly separated from each other. As two electrons of opposite spin may reside in the same level, there are as many levels as there are pairs of electrons in the crystal. This degeneracy does not affect the inner atomic levels, however, which are more tightly bound.

The highest energy band is the conduction band. Electrons in this region are detached from their parent atoms and are free to move around the entire crystal. The electrons in the valence band levels, however, are more tightly bound and remain associated to their respective lattice atoms. The width of the gap and bands is determined by the lattice spacing between the atoms. These parameters are thus dependent on the temperature and the pressure. In a semiconductor, the energy gap is intermediate such that only a few electrons are excited into the conduction band by thermal energy.

At $T = 0\,K$, the lowest energy state, all electrons in the valence band of the semiconductor participate in covalent bonds between lattice atoms. Silicon has 4 valence electrons and forms four covalent bonds.

At normal temperatures $T = 300\,K$, the action of thermal energy can excite a valence electron into the conduction band leaving a hole in the valence band. Hence an electron from neighboring atoms
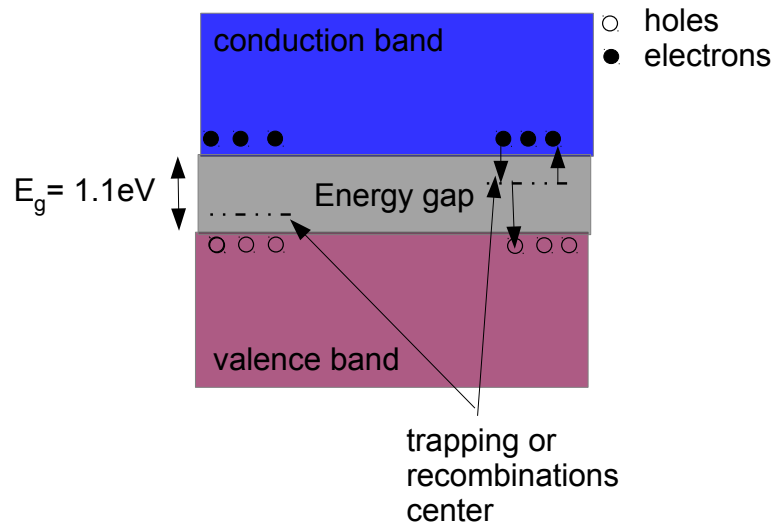
Figure 3.8: Energy band structure of silicon: The band structure arises because of the close, periodic arrangement of the atoms in the Si-crystal which causes an overlap of the electron wave functions. There exists a valence band, a conduction band and a forbidden zone for charge carries, the energy gap. Impurities of the silicon lattice lead to trapping and recombination centers. This results in additional levels within the energy gap,where electrons can be captured and this leads to recombination.

can jump into the hole and so on. Since the hole is positive relative to the sea of electrons in the valence band, the hole acts like a positive charge carrier and the movement constitutes to the electric current [48].

Mobility

Under the influence of an externally applied electric field, the drift velocity of the electrons and holes in a semiconductor can be written as:

$$v_e = \mu_e \cdot E \tag{3.4}$$

$$v_h = \mu_h \cdot E \tag{3.5}$$

where E is the magnitude of the electric field and μ_e and μ_h are the mobilities of the electrons and holes respectively. For a given material the mobilities can be written as a function of E and the temperature T. For silicon at normal temperature μ_e and μ_h vary as a function of $\frac{1}{E}$ for electric fields above $10^4 \frac{V}{cm}$. For these E-field strengths the velocity of electrons and holes saturates and approaches a constant value of about $10^4 \frac{cm}{s}$. Saturation occurs because a proportional fraction of the kinetic energy acquired by the electrons and holes is drained by collisions with the lattice atoms.
At temperatures between 1 and 400 K μ also varies with T^{-m}, where m = 2.5 for electrons and m = 2.7 for holes in silicon [48].
The mobilities determine the current in a semiconductor, since the current density $J = \rho \cdot v$, where ρ is the charge density and v is the velocity. In a pure semiconductor J is given by :

$$J = e \cdot n_i \cdot (\mu_h + \mu_e) \cdot E \tag{3.6}$$

Moreover $J = \sigma \cdot E$, where σ is the conductivity. By comparison with Equation 3.6 this gives the relation

$$\sigma = e \cdot n_i \cdot (\mu_h + \mu_e) \tag{3.7}$$

where the resistivity is given by the inverse of σ. In Table 3.3 a selection of properties of silicon is presented [48].

Atomic Number	Atomic Weight	Energy gap	Energy gap	Electron mobility	Hole mobility
Z	A	(0 K) [eV]	(300 K) [eV]	$[\frac{cm^2}{Vs}]$	$[\frac{cm^2}{Vs}]$
12	28.1	1.1	1.21	1350	480

Table 3.3: A collection of physical properties of silicon. The temperature dependence of silicon arise due to the variation of the energy gap. The different electron and hole mobilities explain the trigger probability for avalanches in an avalanche photo diode. Data taken from reference [48].

Recombination and Trapping

An electron may recombine with a hole by dropping from the conduction band into an open level in the valence band with the emission of a photon. This process is known as direct recombination and is the exact opposite of electron hole generation. Due to energy and momentum conservation the electron and hole must have exact the right energy value in order for this to occur. Therefore, such processes are very rare and lead to lifetimes as long as a second if these were the only processes.

The most important mechanism is through recombination centers resulting from impurities in the crystal. These elements perturb the energy band structure by adding additional levels to the center of the forbidden energy gap, as shown in Figure 3.8. These states may capture an electron from the conduction band and then do one of two things:

- after a certain holding time, the electron is released back into the condition band.

- during the holding time, it may also capture a hole which is then recombined with the trapped electron.

The second effect which arises from impurities is trapping. Some impurities are only capable of capturing one kind of charge carrier, that is electrons or holes but not both. Such centers simply hold the electron or hole and then release it after a certain characteristic time. If the trapping time is on the order of the charge collection time, then obviously charges will be lost and resulting in incomplete charge collection. If the trapping time is very much smaller, then little or no effect occurs.

The third effect are structural defects in the lattice. These may also give rise to similar states in the forbidden band. Such defects include simple point defects such as vacancies in the lattice or atoms which occupy positions in between lattice points and dislocation in which an entire line of atoms is displaced [48].

Doped Semiconductors

In a pure semiconductor, the number of electrons in the conduction band and holes in the valence band is small. This balance can be changed by introducing a small amount of impurity atoms having one more or one less valence electron in their outer atomic shell. For silicon which is tetravalent, this means either pentavalent atoms or trivalent atoms. These impurities integrate themselves into the crystal lattice to create doped semiconductors.

If the dopant is pentavalent a donor impurity level is created as indicated in Figure 3.9. In the ground state the electrons fill up the valence band which contains just enough room for four valance electrons per atom. Since the impurity atom has five valence electrons an extra electron is left, which does not fit into this band. This electron resides in a discrete energy level created in the energy gap by the presence of the impurity atoms. Doped semiconductors in which electrons are the majority charge
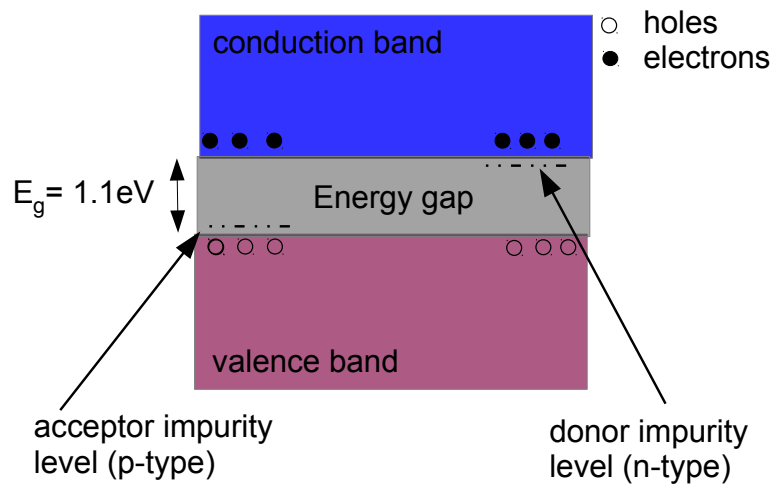
Figure 3.9: Doped semiconductors are produced by the introduction of pentavalent and trivalent atoms into the periodic silicon-lattice. This leads to a donor impurity level close to the conduction band (n-type) for pentavalent atoms and to an acceptor impurity close to the valence band (p-type) for trivalent atoms.

carriers are called n-type semiconductors.

If the impurity is trivalent with one less valence electron, there will not be enough electrons to fill the valence band. There is thus an excess of holes in the crystal, also indicated in Figure 3.9. The trivalent impurities also perturb the band structure by creating an additional states in the energy gap, but this time close to the valence band. Such materials are referred as p-type semiconductors.

Donor elements, for n-type semiconductors, are for example arsenic or phosphorous, while gallium boron and indium are most often employed as acceptor impurities for p-type materials.

The amount of dopant used is generally very small with typical concentrations in the order of $10^{13} \frac{\text{atoms}}{\text{cm}^3}$, whereby the densities of silicon are in the order of $10^{22} \frac{\text{atoms}}{\text{cm}^3}$.

Heavily doped semiconductors are particularly used as electrical contacts for semiconductors. Impurity concentrations are given here:

- p^+ corresponds to a heavily doped p-layer with $10^{20} \frac{\text{atoms}}{\text{cm}^3}$ and

- n^+ corresponds to a heavily doped n-layer with $10^{20} \frac{\text{atoms}}{\text{cm}^3}$

This whole section is taken from references [48] and [3].

3.3.2 Avalanche Photo Diode (APD)

PIN Photo Diodes

The doping profile of a PIN diode is presented in Figure 3.10. A high ohmic intrinsic layer (i or π), with almost no charge carriers is placed between to heavily doped p^+ and n^+ layers. The advantage of a large intrinsic layer is, that only small bias voltages are required for full depletion. Moreover there is a large sensitive volume for the absorption of photons of different energy, from low energy (red wavelength) to high energy (blue wavelength). The electrons created in the intrinsic layer have a large lifetime, since there exists no space charges for recombination within the intrinsic layer. The thick depletion layer reduces the intrinsic device capacitance, which leads to faster rise and decay times.

Due to the missing amplification mechanism, the device sensitivity is not changed by variation of
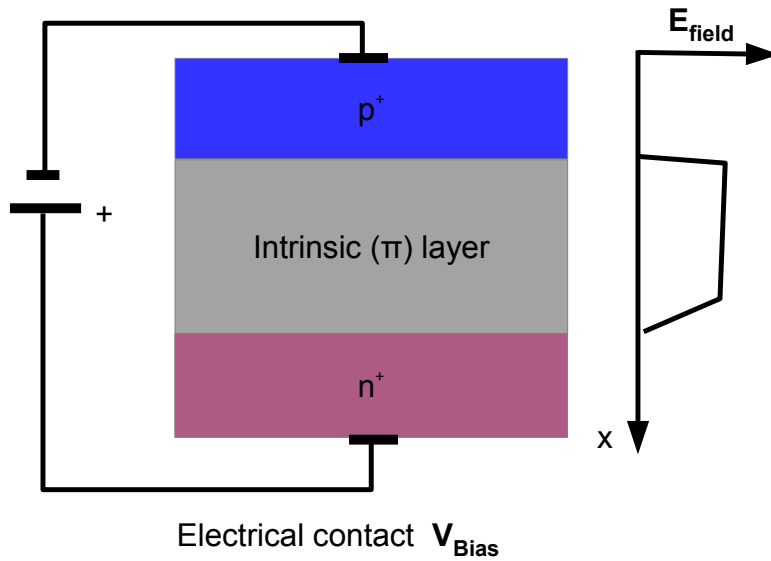
Figure 3.10: Schematic of a PIN-Diode, which consists of two heavily doped p^+ and n^+ layers and an intrinsic i or π layer with almost no charge carries in between.

temperature and bias voltage. Therefore, PIN-diodes are suitable for all kinds of light calibration and monitoring processes. On the other hand the missing internal amplification leads to insensitivity to small light signals, because the detected signals can not be discriminated from electronic background noise. [48]

Avalanche Photo Diode

In contrast to PIN-Diodes avalanche photo diodes (APDs) have a modified doping structure and a higher reversed bias voltage U_{bias} is applied. A typical doping profile of a Silicon APDs is $p^+ - \pi - p - n^+$, as indicated in Figure 3.11. The low doped π-layer serves as depletion layer and has a width of 5 μm. The subsequent narrow (0.5 μm) and high doped n^+ layer creates an area of extreme high electric field (in the order of $10^6 \frac{V}{cm}$ [7]), due to the space charge distribution and the applied bias voltage U_{bias}. This layer forms an avalanche region for electrons, created by photo electric absorption in the intrinsic low doped π-layer.

Due to the high electric field electrons obtain in between two collisions sufficient energy to lift additional electrons into the conduction band by means of impact ionization. Therefore, an avalanche like electron multiplication takes place, which is called Geiger mode and a breakdown of the diode is initiated. This is possible, if the APD is biased above the breakdown voltage U_{bd}.

Below the avalanche region a layer of n^- doped silicon is inserted. This layer serves as drift space for electrons created in the avalanche region and improves the detector characteristics by reducing the detector capacitance for better timing and noise performance.

For the POSSuMUS detector p on n devices are used, which are sensitive to light in the blue wavelength region. Photons of blue wavelength are absorbed in the depletion layer. Due to the electric field the electrons move downward in the direction of the avalanche region and the electron multiplication takes place there.

The holes move upwards, but do not cross the area of extreme high electric field. Therefore, the trigger probability for initiating a breakdown is small for holes.

Lower energetic light (red wavelength) penetrates deeper into the silicon and the electron hole pair is created below the avalanche region, indicated in Figure 3.11. Hence the electrons move downwards
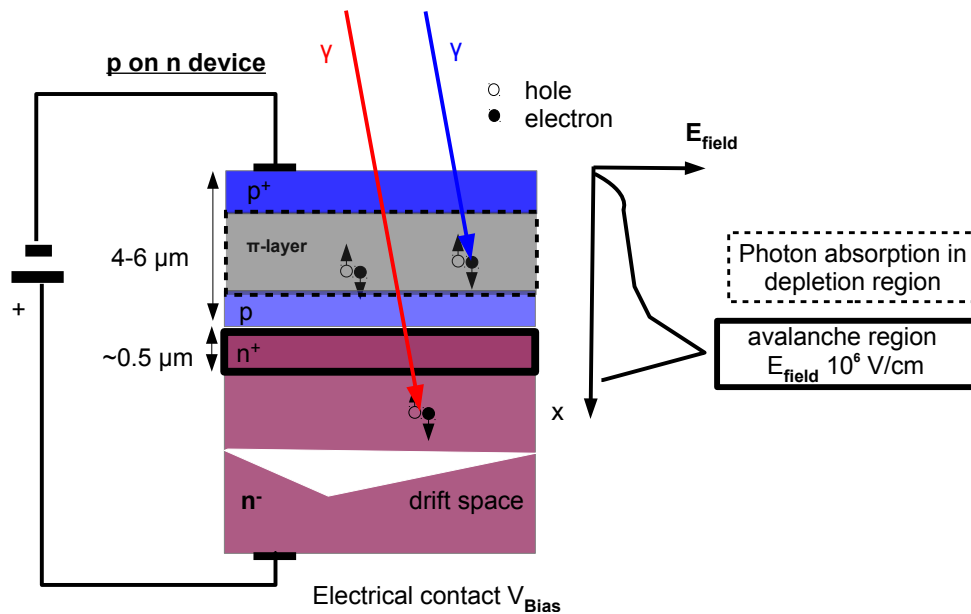
Figure 3.11: The doping profile of an APD, which is sensitive for the blue wavelength spectra is p^+, π, p, n^+. Therefore, the incoming photons are absorbed in the low doped p-layer and create electrons due to photon absorption effect. By the combination of the doping profile and the reversed biased voltage a avalanche region is created. The electrons move towards this avalanche region and are multiplied due to impact ionization.

but do not cross the avalanche region and therefore no breakdown is triggered by the created electrons. The holes move upwards and cross the avalanche region. However, due to the smaller hole mobility the trigger probability for starting a breakdown is low. To stop the avalanche process and prevent the APD from destruction, each APD is equipped with a high ohmic quenching resistor in series (not shown in Figure 3.11).

3.3.3 Silicon Photomultiplier

Silicon photomultipliers consist of a large number of APD pixels operated in Geiger mode. Each pixel (APD) operates like a binary device and creates a standardized signal with high gain, when it is hit by a photon. The pixels are in a parallel circuit and the signal measured at the device connectors is the sum of the individual binary pixels.

In Figure 3.12 a Silicon photomultiplier from Hamamatsu with an active area of 3×3 mm^2 is displayed. At the lower edge of the sensitive area the device connectors are visible, where the sum of firing pixels is measured, at the right side the bias voltage U_{bias} connection is observable. The presented SiPM consists of pixels with an active area of $(25 \ \mu m)^2$ resulting in 900 pixels within the active area of the SIPM. This device is capable of measuring simultaneously arriving photons and therefore can perform measurements with low light intensities.

A SiPM can be described by a simple electric model, presented in Figure 3.13. A SiPM corresponds to an array of reversed bias diodes with a quenching resistor in series. This situation corresponds to point 1 in a U-I characteristic presented in Figure 3.14. The SiPM is biased at U_{over} above breakdown voltage U_{bd} and no charge carrier is present in the depletion layer. Hence, no current flows through the device and the SiPM stays in ready mode.

After a photon absorption, the avalanche process is started and the internal pixel capacitance C_{pixel}
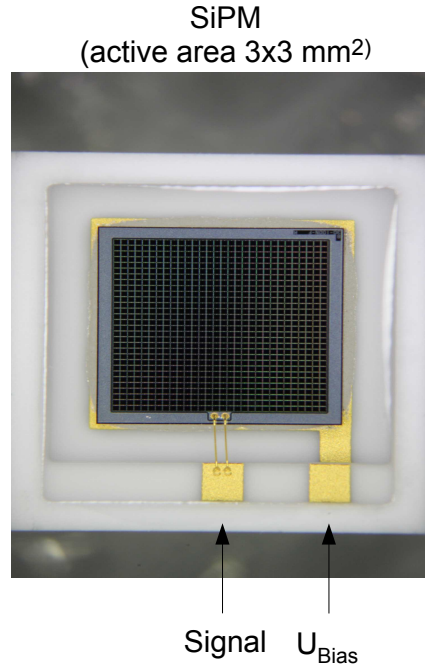
Figure 3.12: Hamamatsu SiPM with an active area of 3×3 mm^2 and a pixel size of $(25\mu\text{m})^2$. This corresponds to 900 pixels within the sensitive area. Each Pixel is capable to detect one photon. At the lower end the device connectors are visible, where the sum of firing pixels is measured, at the right side the bias voltage U_{bias} connection is observable.

starts to discharge over the internal resistance R_{int} until it falls below the breakdown voltage U_{bd}. For an successful quenching of the pixel, the resistor R_{quench} must be chosen large enough so that the discharge time of the pixel is determined by the time constant $\tau_d = R_{int} \cdot C_{pixel}$ and is much smaller than the pixel recovery time constant $\tau_r = R_{quench} \cdot C_{pixel}$. This corresponds to point 2 in Figure 3.14, where a current I_{Av} flows through the device.
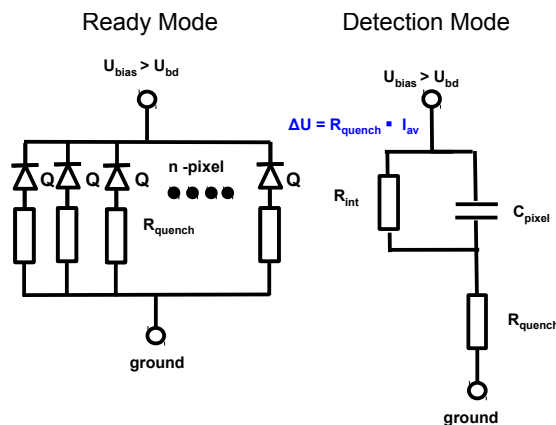
Figure 3.13: Simple electric model to describe a SiPM: The working principle corresponds to an array of parallel reversed biased APDs, where each APD has a quenching resistor in series. If an electron is created by photon absorption in the avalanche region, an avalanche current flows through the APD. Hence, a voltage drop arises at the quenching resistor. After the voltage drops below the breakdown voltage U_{bd} the avalanche process is stopped and the APD is recharged.
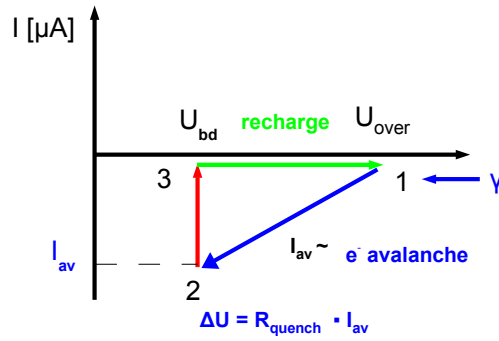
Figure 3.14: SiPM U-I characteristic: At point 1, the pixel is in ready mode and no charge carrier is present in the depletion region. After photon absorption (2) a breakdown takes place within the APD and an avalanche current proportional to the applied over voltage flows through the device. Due to the quenching resistor, the avalanche current causes a voltage drop. Once the applied voltage has reached a value below the breakdown voltage U_{bd} the avalanche current is stopped and the pixel is recharged.

The rising current I_{Av} induces an increasing voltage drop ΔU at the quenching resistor R_{quench} whereby $\Delta U = R_{quench} \cdot I_{Av}$. The voltage across the diode starts to decrease until the breakdown voltage is reached and the avalanche breakdown is stopped. This corresponds to point 3 of Figure 3.14.
After the avalanche is quenched, the capacitance of the APD is recharged again and the diode goes back in the initial state (1) and is ready for further detection of photons.
The released charged Q by each pixel is proportional to the Gain G, which depends on the applied over voltage $U_{over} = U_{bias} - U_{bd}$,

$$Q = G \cdot e = C_{pixel} \cdot (U_{bias} - U_{bd}) = C_{pixel} \cdot U_{over} \tag{3.8}$$

SiPM Characteristics

The following section summarizes characteristics of SiPMs detailed in [60].

Dark Counts

Besides electrons created via photon absorption any electron hole pair created in the depletion region of an APD, see Figure 3.11 can cause an avalanche process, which is indistinguishable from a photon event. The latter produces dark counts with a rate of 100 kHz to several MHz per mm^2 with a threshold at half of the one photon amplitude. There exist two main mechanisms for creating dark counts. The first one is thermally generated free charge carrier. An electron from the valence band is lifted to the conduction band due to phonon interaction.
This contribution to the dark rate can be reduced by cooling. The dark counts are reduced by a factor of two every 8 °C. The dark counts can also be reduced by minimizing the number of generated recombination centers, the impurities and crystal defects.
The second mechanism for the creation of dark rate events is the field assisted charge carrier production, where an electron tunnels through the band gap of silicon. This effect is only possible due to the presence of the high electric field.
This effect can only be reduced by minimizing the electric field and therefore the gain of the APD.

Optical Crosstalk and Afterpulsing

In an avalanche breakdown there are on average three photons emitted from recombination processes per 10^5 charge carriers with a photon energy larger than 1.14 eV, the band gap of silicon.

When these photons travel to neighboring pixels they can trigger a breakdown there. This optical crosstalk acts like shower fluctuations in an APD. It is a stochastic process and introduces an excess noise factor like in a usual APD or in a photomultiplier.

Carrier trapping and delayed release cause afterpulses during a period of several microseconds after a breakdown. Afterpulses with short delay contribute little because they are not fully recharged but have an effect on the recovery time. Operation at low temperatures elongates the delayed release by a factor of 3 when the temperature is reduced by 25°C.

Recovery Time and Timing

$$\tau_{\text{recovery}} = C_{\text{pixel}} \cdot R_{\text{quench}} \tag{3.9}$$

The time needed to recharge a cell after a breakdown has been quenched depends mostly on the cell size due to its capacitance and the individual resistor (RC), as described in Section above. Afterpulses can prolong the recovery time because the recharging starts anew. To reduce these effects the operation at low gain is favored. The smallest value for the recovery time is obtained for APDs with small cells and small resistors/Polysilicon resistors are used for quenching the avalanche process. They change their value with temperature. Therefore, there is a strong dependence of the recovery time on the temperature.

Since the active layer of silicon are very thin $(2 - 4\mu\text{m})$ the avalanche process is fast and the signal amplitude is big. Thus, very good timing properties even for single photons can be expected. A time resolution with a standard deviation of 42 ps is achievable.

Photon Detection Efficiency
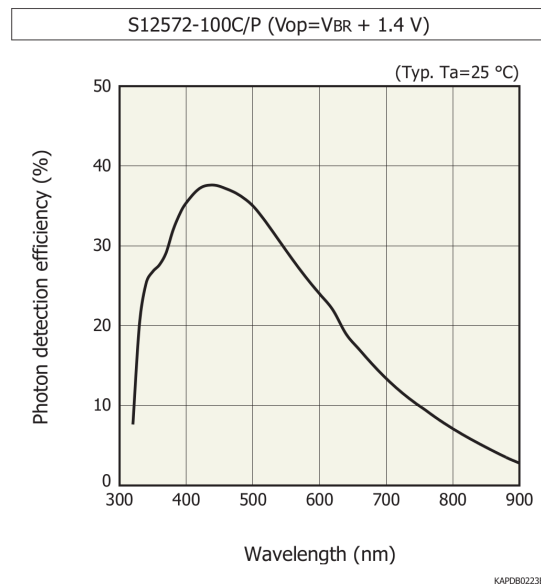
Photon detection efficiency does not include crosstalk or afterpulses.

Figure 3.15: The photon detection efficiency (PDE) for the Hamamatsu SiPM type S12572-100C is presented: The peak of the PDE is in the blue wavelength spectrum at 450 nm. This fits with the emission spectrum of the WLS-fiber, presented in Figure 3.7. By using the combination of the BC-400 plastic scintillator, BCF-92 WLS-fiber and SIPMs sensitive in the blue wavelength region it is possible to measure the amount of scintillation light.

The photon detection efficiency (PDE) is given by the product of quantum efficiency of the active area (QE), a geometric factor P_{geo}, whereby P_{geo} is the ratio of sensitive to total areas and the probability $P_{trigger}$ of incoming photons to trigger a breakdown.

$$PDE(U_{Bias}, \lambda) = QE(\lambda) \cdot P_{geo} \cdot P_{trigger}(U_{Bias}) \tag{3.10}$$

The QE is 80 to 90 % at maximum depending on the wavelength of the incoming photons.

The geometric factor P_{geo} needs to be optimized depending on the application. Since some space is needed between the APD pixel cells for the individual resistors and to reduce optical crosstalk the best filling factor can be achieved with a small number of big cells. The geometric factor is in the range of $20 - 30$ %.

The trigger probability $P_{trigger}$ depends on the position where the primary electron hole pair is generated and on the applied over voltage U_{over}. A high gain operation is favored. Electrons have in silicon a better chance to trigger a breakdown than holes. Therefore, a conversion in the p-layer has the highest probability.

In Figure 3.15 the Photon Detection Efficiency is presented for the range of wavelengths of 300 to 900 nm. In combination with the emission spectra of the scintillator, see Figure 3.5 and the absorption and emission spectra of the WLS-fiber, see Figure 3.7 the PDE of the used Hamamatsu devices matches to the other spectra and it is possible to measure small amounts of scintillation light.

Temperature Dependence
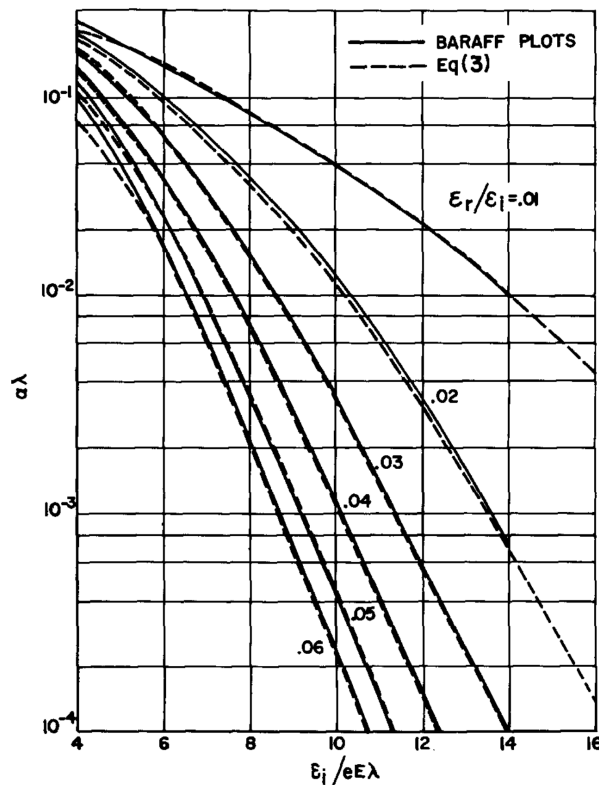
Figure 3.16: The ionization coefficient α_n depending on the electrical field is presented for different temperatures. The ionization coefficient α_n decreases with the increasing temperatures for the same electrical field. Hence, the breakdown voltage increases with increasing temperature. [26]

Silicon photomultiplier are sensitive to temperature variations. More precisely, the device specific breakdown voltage U_{bd} increases linearly with the temperature. If the applied bias voltage U_{bias} is

kept constant, the over voltage U_{over} decreases linearly with increasing temperature. This leads to a linear temperature dependence of the gain with negative slope

$$\frac{dG}{dT} = \frac{C_{pixel}}{e} \cdot \frac{dU_{break}}{dT} \tag{3.11}$$

The breakdown voltage is temperature dependent due to the fact that the impact ionization coefficient α_n of electrons is decreasing with increasing temperature, see Figure 3.16. Qualitatively this follows from the fact that the oscillations of the crystal lattice varies for different temperatures. For low temperatures the oscillations slow down and thus the mean free path for electrons and holes increases. Therefore, the electrons and holes easier gain enough energy for secondary ionization. Thus the breakdown voltage decreases with decreasing temperature and the other way around [26].
The behavior of the breakdown voltage of the SiPM is investigated in Section 4.1 and the breakdown voltage for different temperatures of one SIPM is measured and a temperature coefficient is determined.

Chapter 4

Characterization of Silicon Photomultiplier

After introducing the functional principle of an Avalanche Photo Diode and its application in a Silicon Photomultiplier, the next step is to characterize the used SiPM devices. For that purpose studies have been made to determine several characteristics discussed in Section 3.3. The most interesting characteristic is the breakdown voltage U_{bd} and the temperature dependence of it. Another investigated property is the quenching resistance R_{quench}.

4.1 Determination of Breakdown Voltage

To determine the breakdown voltage U_{bd} of SiPM two different approaches were realized. The first one is to determine U_{bd} via an U-I-characteristic by measuring the current, created by dark rate events, detailed in Section 4.1.1. The second approach is to determine the breakdown voltage U_{bd} with an external light source, see Section 4.1.2.

4.1.1 Determination of Breakdown Voltage with U-I scan
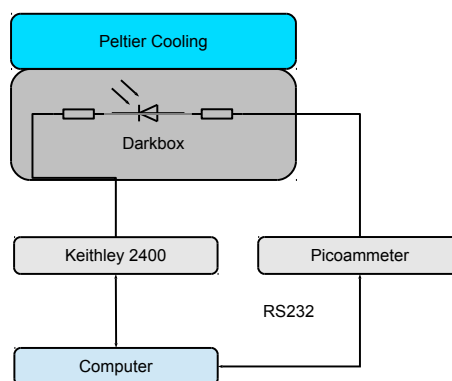
Figure 4.1: Experimental Setup for the characterization of SiPMs with U-I-characteristic: The SiPM under test is soldered and mounted in a temperature controlled light tight box. The SiPM is connected to a voltage source [44] and a programmable electrometer [45] to measure the device current for different bias voltages U_{bias}. Figure taken from reference [35].

The first approach is to determine the breakdown voltage (U_{bd}) by measuring the dark current of a SiPM for different applied bias voltages (U_{bias}). The experimental setup for this measurement

is presented in Figure 4.1. The investigated SiPMs are soldered to a test board and mounted in a temperature controlled light tight box. The temperature stability is provided by a Peltier element, which is used for cooling or heating the box. The temperature control system is described in detail in reference [35].

The SiPM is connected to a programmable electrometer Keithley Model 6514 [45] to measure the device current and to the voltage source Keithley 2400 [44] to provide U_{bias}.

Forward Scan
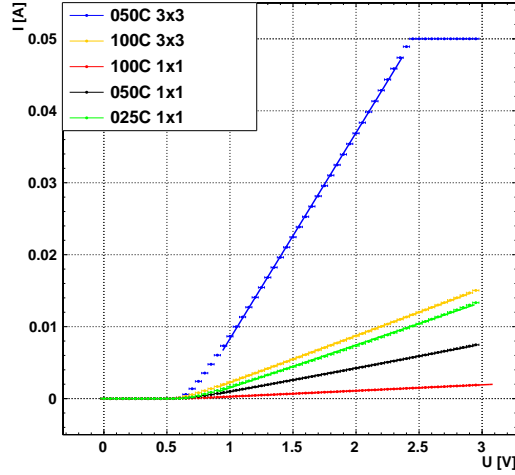
Figure 4.2: Forward Scan of a Ham. $(3x3 \text{ mm}^2)$ 100 C and Ham. $(1x1 \text{ mm}^2)$ 050 C. By measuring the U-I characteristic in a forward scan, the determination of the quenching resistor R_{quench} is possible. Figure taken from reference [35]

To determine the value of the quenching resistance R_{quench} of the SiPM under test, a forward scan of the U-I-characteristic is performed at a constant temperature of 20°C with the described experimental setup. The SiPMs under test are Hamamatsu SiPMs MPPC S12571-50C [36] and Hamamatsu MPPC S12572-100C [37] with an active area of either (1×1) mm^2 or (3×3) mm^2 with different pixel sizes. The U_{bias} is varied from 0 to 3 V and the current is measured. The forward characteristic is determined by the typical diode equivalent resistance for voltages below about 0.7 V, the built in potential of a silicon diode.

The value of the quenching resistor of the SiPM can be determined by fitting a straight line to the

Type	R_{SiPM} [Ω]	R_{quench} [kΩ]
Ham. $(1x1 \text{ mm}^2)$ 050 C	303 ± 2	121 ± 1
Ham. $(3x3 \text{ mm}^2)$ 100 C	153 ± 1	138 ± 1

Table 4.1: The Quenching resistance and SiPM resistance for different SiPM-types are presented. The values are obtained by an linear fit to the forward voltage characteristic, see Figure 4.2. Results taken from Reference [35].

measured points, see Figure 4.2 and multiplying the SiPM resistance with the number of cells n_{cells} of the tested SiPM device. In Table 4.1 the values of the quenching resistor for SiPMs used in the first prototype detector (Ham. $(1x1 \text{ mm}^2)$ 050 C) and second prototype detector Ham. $(3x3 \text{ mm}^2)$ 100 C. In the following sections the characterization is focused on SiPMs of type (MPPC S12572-100C) [37], whereby the method is also suitable for all types of SiPMs.

Reverse Scan

The breakdown voltage U_{bd} is determined with the same experimental setup, see Figure 4.1, whereby a reverse scan of the U-I characteristic is recorded. Therefore, an automatic measurement system was developed which increases the bias voltage until a leakage current of $2\mu A$ is reached. In Figure 4.3 the measured reverse current is presented. A detailed description of the current behavior can be found in [35]. In this work the focus is on the determination of the breakdown voltage. To determine the
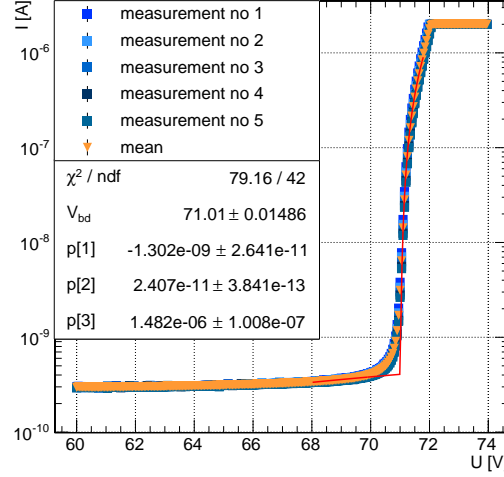
Figure 4.3: Reverse scan for the Hamamatsu SiPM (MPPC S12572-100C) under test: By recording the U-I characteristic with a reverse scan the breakdown voltage U_{bd} is determined. By applying a fit, see Equation 4.1, U_{bd} is determined with an accuracy of 71 ± 0.2 V. Figure taken from reference [35].

value of U_{bd} from the U-I characteristic the following fit function is used:

$$I(U_{bias}) = par[1] + par[2] \cdot U_{bias} + par[3] \cdot \theta(U_{bias} - U_{bd}) \cdot (U_{bias} - U_{bd})^2 \qquad (4.1)$$

This fit holds for U_{bias} as long as the recharging time is far greater than $R_{quench} \cdot C_{cell}$. For higher negative bias voltages the current through the junction approaches the asymptotic value of $I = R_{quench} + R_D$, where R_D is the variable diode cell resistance and the amount of charge contained in a single pulse increases more than linearly because the avalanche quenching time increases with U_{over}. This is also amplified by the increase of afterpulsing processes with higher U_{over}. [35].
From the fit in Figure 4.3 the breakdown voltage can be determined.

$$U_{bd} = 71.0 \pm 0.2 \text{ V} \qquad (4.2)$$

whereby good fit results depend strongly on the preset of the parameters. Moreover the range of the fit region is not clearly defined. Therefore, the fit errors quoted in Figure 4.3 underestimates the complete uncertainty. A realistic error is in the order of 0.2 V

4.1.2 Determination of the Breakdown Voltage External Light Source

In Figure 4.4 the experimental setup is presented to determine the breakdown voltage U_{bd} with an external LED. The SiPM device under test is mounted in a temperature controlled light tight box, soldered on the pre-amplifier board described in Section 5.3. The SiPM is connected to a LED [68] via a clear waveguide. The LED emits 8 ns long light pulses. The signal response of the SiPM is recorded by a standard VME-based QDC-readout. Details of the QDC-readout can be found in
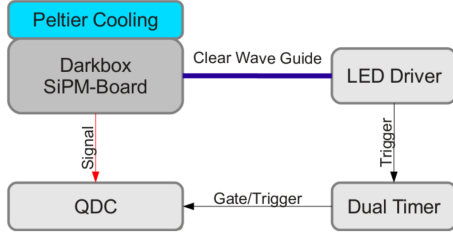
Figure 4.4: Experimental setup for the determination of the breakdown voltage U_{bd} with an external LED [68] . The SiPM device under test is mounted in a temperature controlled light tight box. From a LED, light pulses are sent to the sensitive area of the SiPM by using a clear waveguide. The data acquisition system is a standard VME-based QDC-readout. Figure taken from reference [35].
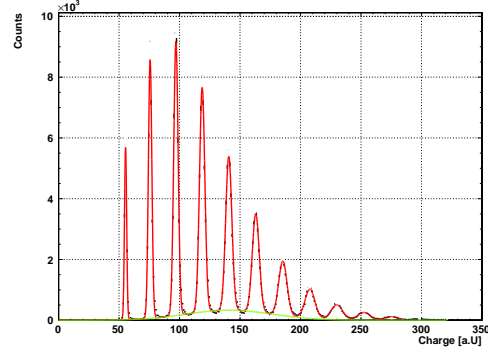
Figure 4.5: Recorded light spectra for the SiPM under test: The first peak is the pedestal peak and correspond to zero detected photons. The following peaks correspond to the number of fired pixels. The spectra is fitted by a multi-Gaussian fit to extract the mean values and standard deviation for further analysis. Figure taken from reference [35].

Appendix A.2. The data acquisition system is started by a trigger, which is sent by the LED after a light pulse is emitted.

For the determination of the breakdown voltage the light output of the LED was chosen to be small, so that the peak spectrum of the SiPM is observable. The applied bias voltage U_{bias} at the SIPM is above the breakdown voltage U_{bd}.

In Figure 4.5 the SiPM response of light pulses, emitted by the LED, is presented. The peaks structure of the SiPM device is visible. Each peak corresponds to the number of fired pixels, whereby the first peak is the pedestal peak and corresponds to zero detected photons. The offset of the pedestal peak arises due to electronic noise at the QDC-channel.

For analysis a multi-Gaussian fit function with Gaussian background was used, described by the following formula:

$$f(x) = A_{bg} \cdot N(\mu_{bg}, \sigma_{bg}^2) + \sum_{i=1}^{n_{peaks-found}} A_i \cdot N(\mu_{bg}, \sigma_{bg}^2) \tag{4.3}$$

where $N(\mu_{bg}, \sigma_{bg}^2)$ is a standard normal distribution. The gaussian background corresponds to surface currents and dark counts, which smear out the gaussian peaks.

In Figure 4.6 the mean values for the peak number one to number nine for thirteen different bias voltages U_{bias} are plotted, measured at the same temperature. Linear functions are fitted to all mean values of each peak number. The interception point of the fits with the x-axis corresponds to the breakdown voltage U_{bd} of the SiPM under test at the adjusted temperature. The slope of the linear fit to peak number one is proportional to the change of the gain with the applied voltage $(\frac{dG}{dV})$.

The exact determination of the breakdown voltage U_{bd} is described in [35] and the results for the tested SiPM is:

$$U_{bd} = (69.44 \pm 0.07)V \tag{4.4}$$

The determination of U_{bd} is repeated at five different temperatures in the range from 6 to 21 °C. The aim is to determine a correction coefficient for the variation of U_{bd} with the temperature.

In Figure 4.7 the result of the temperature variation is presented. A straight line is fitted at the data
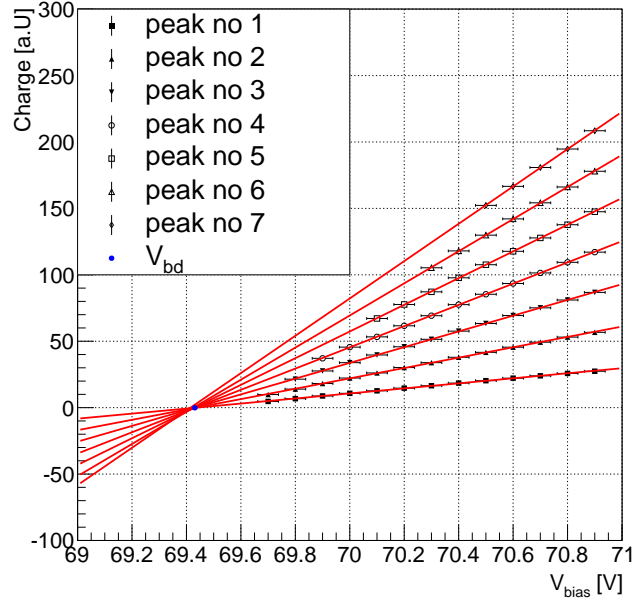
Figure 4.6: To determine the breakdown voltage the peak positions for various charge spectra of the SiPMs are plotted against the bias voltage U_{bias}. Straight lines are fitted to the mean values of various peak numbers. The interception point of the fitted lines with the x-axis corresponds to the breakdown voltage at the adjusted temperature. Figure taken from reference [35].

points and the slope of the fit corresponds to the temperature coefficient τ_{SiPM} of the SiPM under test.

$$\tau_{SiPM} = 60.8 \pm 0.6 \frac{mV}{K} \tag{4.5}$$

For each SiPM, used for at the POSSuMUS detector, U_{bd} is determined. Therefore same over volt-
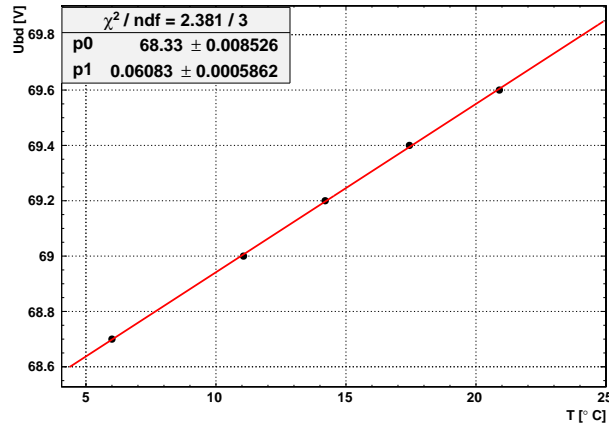
Figure 4.7: Determination of the temperature coefficient τ_{SiPM}: The temperature dependence $\frac{dV_{bd}}{dT}$ is determined by using the measured breakdown voltages of the SiPM at different temperatures. The slope of fit corresponds to the temperature coefficient τ_{SiPM}. Figure taken from reference [35].

ages U_{over} can be adjusted such that the gain values are equal for all used SiPMs. To provide the individual bias voltages a multi channel voltage divider is used, which is described in Section 4.2.1 and used for the first prototype detector.

The measured temperature coefficient τ_{SiPM} is used to adjust the U_{over} correctly for varying ambient temperature. This is realized in an automatic multi channel gain stabilization system in Section 4.2.2, using Equation 4.6.

$$U_{over} = U_{bias} - U_{bd}(T) \tag{4.6}$$

and developed for the second POSSuMUS prototype, described in Chapter 8.

4.2　Multi Channel Voltage Source for POSSuMUS

4.2.1　Voltage Divider I
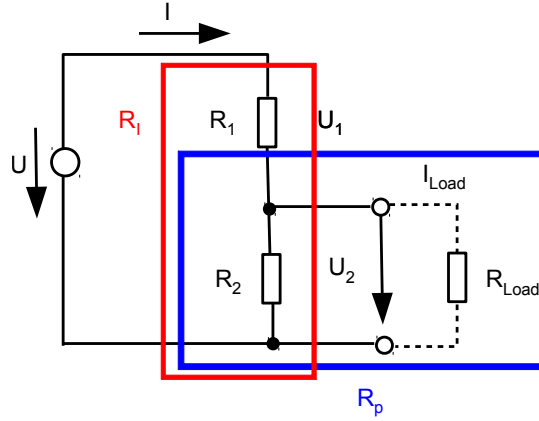
Figure 4.8: Schematic of a loaded voltage divider: For the first POSSuMUS prototype a multi-channel voltage divider was used to set the individual U_{bias} at each SiPM of the detector to work with similar gain values.

The POSSuMUS detector has several readout channels to detect the scintillation light created by crossing minimal ionizing particles. Therefore a multi-channel voltage divider is needed to provide the bias voltage U_{bias} for each SiPM.

The adjustable voltage divider is realized by the use of analog potentiometers, where a sliding or rotating contact forms an adjustable resistor. In Figure 4.8 a schematic of the functional principle of one channel is presented.

The terminal voltage for the voltage divider with resistance R_1 and R_2 is given by

$$U_T = \frac{R_2}{R_1 + R_2} \cdot U = R_I \cdot U \tag{4.7}$$

The resistance of the parallel circuit R_p of R_2 and R_{Load} is smaller than the smallest resistance in the parallel circuit.

$$R_p = \frac{R_2 \cdot R_{Load}}{R_2 + R_{Load}} \tag{4.8}$$

Therefore, the terminal voltage reads with the load resistance as,

$$U_t = \frac{R_p}{R_1 + R_p} \cdot U \tag{4.9}$$

The design value of the inner resistance R_I was chosen to be small in comparison with R_{Load}. Therefore the value of R_I is 20 kΩ. The minimum load resistance is in the order of 700 kΩ, if the SiPM is saturated.

The first voltage divider is equipped with twenty potentiometers to provide adjustable bias voltages for SiPMs. This voltage divider was used for the test of the first prototype. This is presented in detail in Chapter 6.

This voltage divider is usable for measurements of short duration (in the order of 20 minutes), when the ambient temperature is almost constant. It is not applicable for long term measurements of several weeks due to the lacking function to automatically adjust U_{bias} temperature changes of the environment. Therefore, a remotely controllable voltage divider is developed for active gain stabilization.

4.2.2 Voltage Divider II
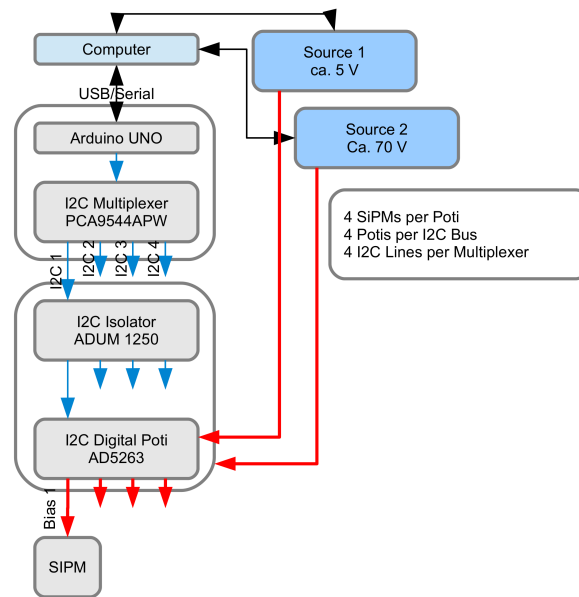
Figure 4.9: The multichannel gain stabilization system uses an arduino and the I^2C protocol to communicate with the digital potentiometer. With this system it is possible to apply a constant U_{over} for varying temperature conditions. The system is capable to supply 64 SiPMs separately. Figure taken from reference [35]

The second voltage divider was developed as a modular voltage source for constant gain conditions at the SiPMs of the POSSuMUS detector. Again, potentiometer were used, whereby the analog potentiometer were replaced by digital potentiometer [27]. Each digital potentiometer is capable to adjust four voltages independently (communication via I^2C-protocol). In parallel a temperature monitoring is installed directly at the SIPM, see Chapter 5. If the temperature variation is larger than $0.3\,^\circ C$ a voltage adjustment with the measured temperature coefficient τ_{SiPM} is automatically applied. In Figure 4.9 the design of the voltage divider is presented. The communication with the digital potentiometer is controlled by an arduino [2]. The present voltage divider is capable to supply 64 channels in parallel, by 16 plug in-cards equipped with one digital potentiometer respectively.

Therefore, this system is capable to supply several modules of the POSSuMUS detector in parallel. A detailed description about calibration measurements can be found in [35].

4.2.3 Gain Stabilization System for SiPMs

In Figure 4.10 the variation of the gain value for one SiPM is presented for the measurement period of three days. The corresponding temperature profile is displayed in the neighboring Figure 4.11. As expected from the described temperature dependence of SiPMs, introduced in Section 3.3, the

gain values decrease with increasing temperature and increase with decreasing temperature due to the variation of the breakdown voltage U_{bd}. The day night cycles are observable in both Figures. The

Figure 4.11: The corresponding temperature profile for three days.
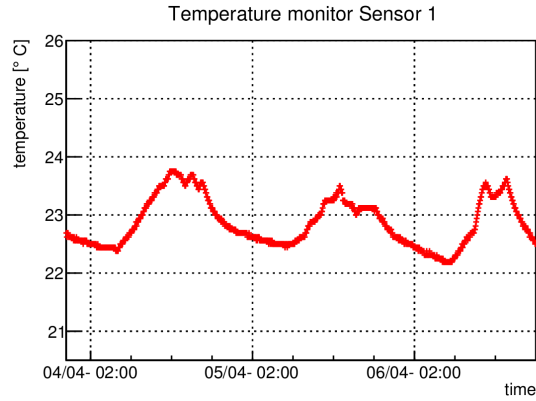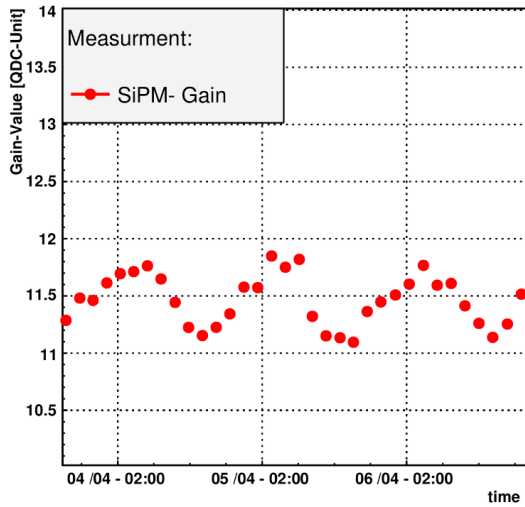
Figure 4.10: The variation of the gain value due to temperature changes at a fixed bias voltage U_{bias} is observable for the period of three days. The gain values increase with decreasing temperature, because of the decreasing value of the breakdown voltage U_{bd} and the other way around.

second voltage divider, described in Section 4.2.2 is used to compensate the bias voltage U_{bias} for temperature changes of the environment. The result is presented in Figure 4.12 and 4.13, where the gain values and the temperature profile are presented for the period of one week. The bias voltage U_{bias} is adjusted by using the correction factor of $60.8 \frac{mV}{K}$, determined in section 4.1.2.

Due to the remote adjustment of the bias voltage U_{bias} the gain values are constant over the period of one week with an accuracy of 2% despite of temperature changes of 3.5°C, observable in Figure 4.13.
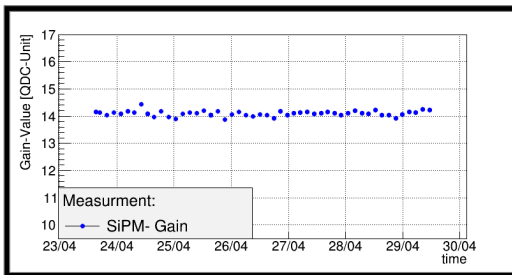
Figure 4.12: By adjusting the Bias voltage remotely according to temperature changes of the environment. It is possible to keep the gain value constant with an accuracy of 2 % for the period of one week despite of temperature change of 3.5°.
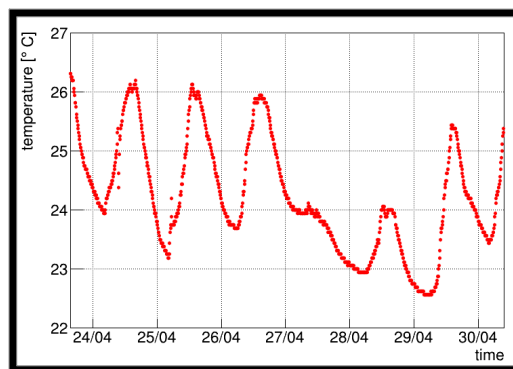
Figure 4.13: Temperature profile for the gain stabilized measurement in Figure 4.12.

Chapter 5

Detector Construction

In this chapter the construction of a POSSuMUS detector is presented. The major construction steps include: the production of trapezoidal shaped plastic scintillators, their equipment with WLS fibers as well as the coupling of the WLS fibers with SiPMs. In particular, details on the gluing of the WLS fibers and the polishing of the fiber ends are discussed.

5.1 Trapezoidal Shaped Scintillators
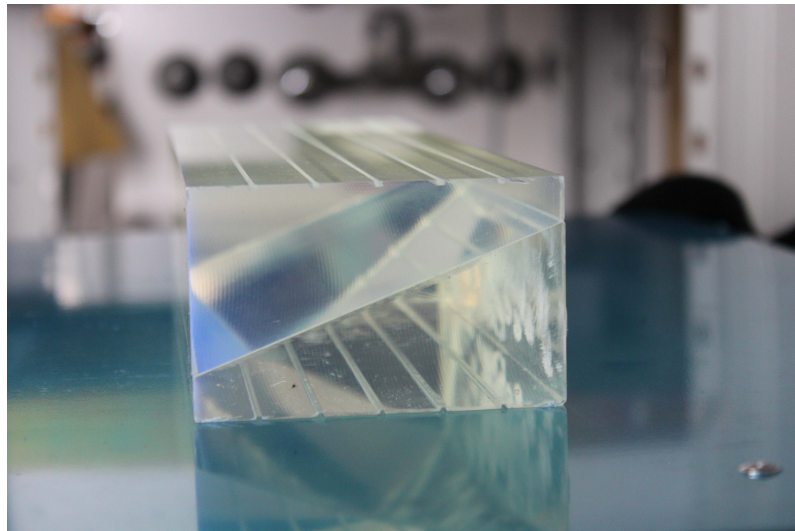
Figure 5.1: The trapezoidal shaped scintillators are obtained from rectangular shaped scintillators and a milling machine to form the wished geometry. At the end of the milling process all surfaces are polished with polishing paste. Grooves are milled out by using of a diamond saw and are located on the top surface of the scintillator.

A rectangular BC 400 [32] scintillator block with a length of 2 m, a width of 88 mm and a height of 46 mm is used. A milling machine changes the rectangular shape to the foreseen trapezoidal shape. The grooves, where the WLS-Fibers are glued in, are milled into the trapezoid with a diamond saw. The entire scintillator surface is cleaned and polished with polishing paste. The first prototype of POSSuMUS is built using two trapezoidal scintillators, mounted on top of each other as demonstrated in Figure 5.1.

5.1.1   The Gluing of Wavelength Shifting Fibers

The grooves within the scintillator trapezoids are used for housing the WLS-Fibers. The grooves are cleaned thoroughly and the scintillator is mounted in a clean room, to minimize the contamination of the grooves with dust.

Before equipping with WLS-fibers, the two component optical cement BC 600 [33] is mixed and put into a vacuum chamber to remove all air bubbles from the glue. After vacuuming, the glue is put into a syringe with cannula, as illustrated in Figure 5.2.

Before the gluing process is started the edges of the grooves are masked with adhesive tape to ensure sharp edges after the gluing process. Each groove is filled with glue whereby the cannula ensures that the glue is put only in the groove and does not contaminate the rest of the scintillator surface. Afterwards, the WLS-fiber is put into the groove and a second layer of glue is put on top of it. The glue cures for 24 hours in a dark environment.
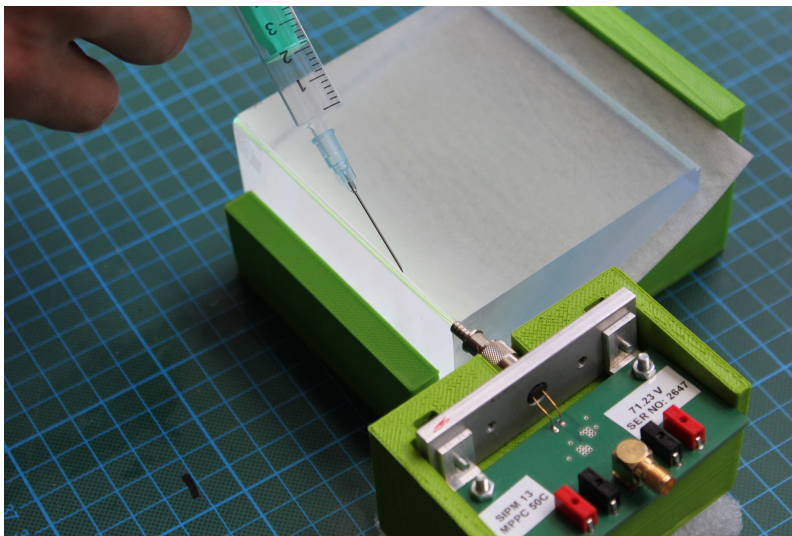
Figure 5.2: The gluing of the WLS-fiber in a groove of the scintillator is presented: The gluing process takes place in a clean room to minimize dust contamination. The glue is inserted in the groove by using a syringe with cannula. Afterwards the WLS Fiber is put into the groove. The scintillator and the WLS-Fiber remain 24 hours in the clean room for curing the glue.

5.1.2   Wrapping of Scintillators

After the gluing of the WLS fibers on the scintillator, the trapezoids are wrapped, either in aluminum foil for directed reflection or in Tyvek [80] for diffuse reflection.

To make the wrapping of the scintillator reproducible and easy to handle, templates for the wrapping materials are used. The template corresponds exactly to the surface area and geometry of the scintillator. The required number of wrapping layers are produced and the scintillator is wrapped.

5.2   Coupling of WLS-Fiber and SiPM

FC-Connector

After the wrapping of the scintillator the WLS-fibers are equipped with FC-connectors [24]. On the surface of the fiber the glue Epotek 353 ND [51] is spread and the FC-connector is mounted and fiber
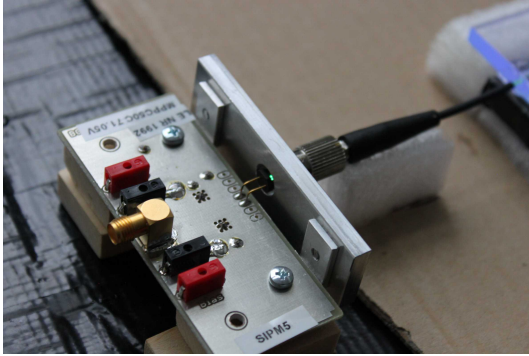
Figure 5.3: The coupling of SiPM and fiber is realized via a FC-connection system. The FC-plug is glued on the end of the WLS-Fiber. A holder with FC-socket is mounted at the edge of the preamplifier board, where the SIPM board is soldered.

Figure 5.4: The preamplifier board with a SiPM and the FC-socket system is displayed. Besides allowing for a reproducible coupling of a SIPM to the fiber, a temperature sensor can also be mounted as close as possible to the SIPM, to monitor the change of ambient temperature.

and plug cure for another 24 hours. The fiber ends of the WLS fiber are polished by using a polishing disc [25] and two abrasive papers with a coarse grain of 1000 and afterwards a fine grain of 10000.

Holder with FC-Socket for SiPM Mounting

The SiPM is soldered on a printed circuit board (PCB) with a preamplifier. The electrical circuit is described in detail in the following Section 5.3. This board is equipped with a FC-socket, visible in silver in Figures 5.3 and 5.4. By the use of the FC-connector system the WLS fiber points directly to the sensitive area of the SiPM, and the distance between fiber and SiPM can be minimized until the WLS fiber is in contact with the SiPM.

Moreover, the holder can also be used to mount a temperature sensor as close as possible to the SiPM, as observable in Figure 5.4.

Instead of a direct coupling of WLS-fiber and SiPM there is also the possibility to add materials with the same refractive index in between fiber and SiPM. Two materials were investigated, namely optical grease [30] and Silicon pads [54]. The influence of a different coupling in comparison with direct coupling has been investigated and the results are presented in Chapter 7.

The advantage of the FC-connection system is the reproducibility and the connection strength of the coupling of WLS fiber and SiPM.

On the other hand the cost per readout channel are increased and the risk, when using a FC-connection system is enhanced to damage the fiber, by means of the weight at the end of the FC-plug.

5.3 The Amplification Board for SiPMs

The preamplifier printed circuit board (PCB) has an amplification factor of 8.9 in the relevant frequency region below 900 MHz. Its core component is an Infineon BGA614 amplifier [39]. The preamplifier can handle the very fast SiPM pulses as the additional capacitance is minimized by mounting the SiPM close to the Infineon amplifier. This is very important, also because the preamplifier itself emits a high frequency signal and any unshielded wiring catches it like an antenna. This would bias the physical signal [65]. Detailed information on the preamplifier board can be found in reference [58].
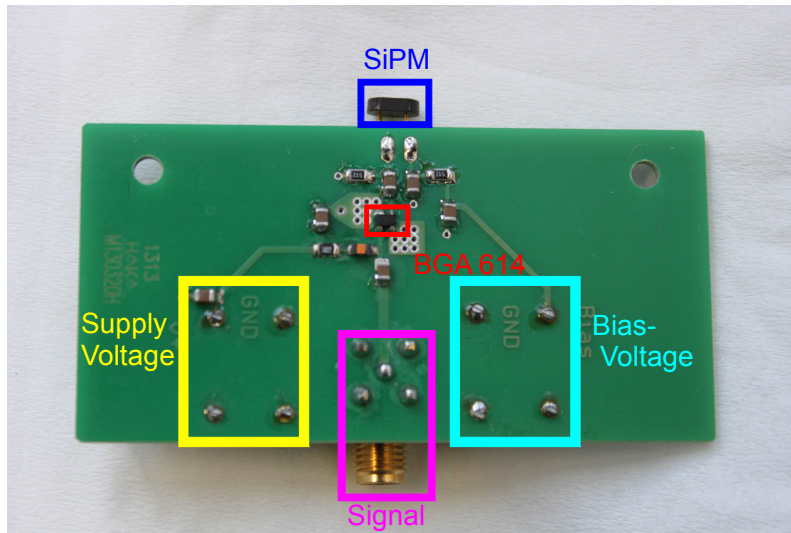
Figure 5.5: The amplification board for SiPMs is a printed circuit board (PCB) with an amplification factor of 8.9. The core component is the BGA614 amplifier from Infineon [39]. Three connectors are visible, on the left side the supply voltage of + 5V for the amplifier and on the right the bias voltage. In between the SiPM-signal readout is done through a SMA connection at the center of PCB board.

In Figure 5.5 the back side of the amplification board is presented. The soldered SiPM is indicated by the **blue** square. The supply voltage of +5 V for the amplifier is applied at the left side, indicated by the **yellow** square. At the right side, indicated by **cyan** square the bias voltage for the SiPM is applied, which varies depending on the individual SiPM and SiPM type. The SiPM signal readout is done through a SMA connection at the center of the PCB, indicated by **magenta** square.

Chapter 6

First POSSuMUS Prototype

The new detector concept was tested for the first time at the experimental site H6, located in the north area of CERN. For that purpose a prototype detector was constructed and ready for measurement. The aim of this experiment was to prove the detector principle and determine the properties of the detector.

6.1 Detector Design of CERN Prototype
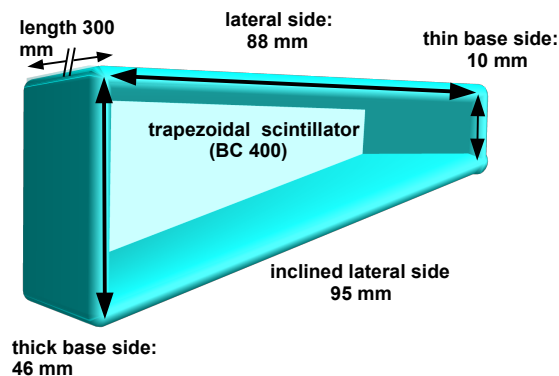
Figure 6.1: Geometry of the trapezoid: The lateral side, which corresponds to the width of the scintillator is 88 mm wide, the inclined side is 95 mm wide. The bases of the trapezoid are 46 mm at the thick side and 10 mm at the thin side. The length of the scintillator is 300 mm. This geometry leads to an active area of 264 cm^2.

The new detector concept is based on the idea of combining two trapezoidal scintillators to determine a two dimensional position sensitivity for traversing minimal ionizing particles, as described in detail in Chapter 2.
For this purpose rectangular plastic scintillators of type BC 400 [32] are cut out to a trapezoidal shape, as described in chapter 5.1. The geometry of the trapezoid is defined as follows, see Figure 6.1:

- the lateral side, which corresponds to the width of the trapezoid is 88 mm wide,

- the inclined side is 95 mm wide,

- the thick base of the trapezoid is 46 mm high,

- the thin base of the trapezoid is 10 mm high,

- the length of the scintillator is 300 mm,

- resulting in a position sensitive area of 264 cm^2.
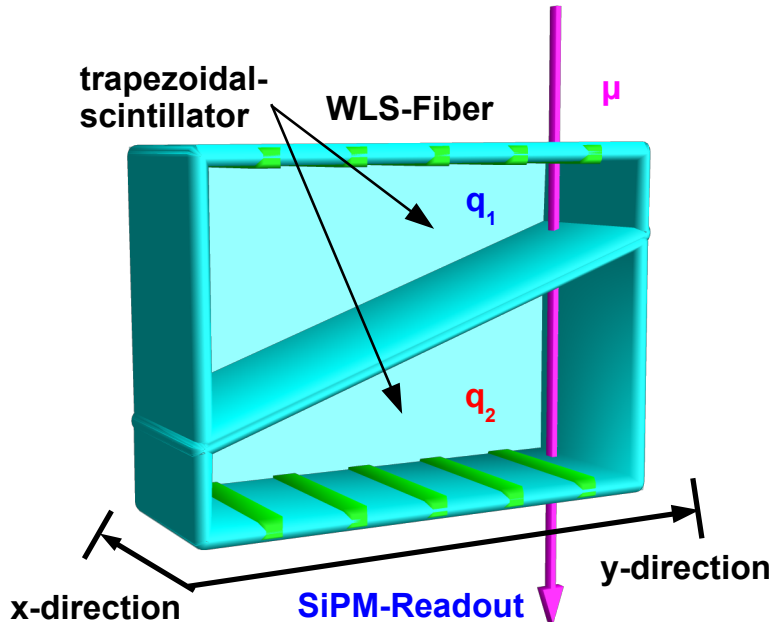
Figure 6.2: The first POSSuMUS prototype consists of two optically insulated trapezoidal scintillators. Each of the trapezoids is equipped with five WLS-fibers, glued into several grooves located at the lateral side of each trapezoid. The scintillation light is measured with SiPMs, located at the end of the WLS-fibers. The spacing between neighbored fibers or the edge of the trapezoid and the fiber is 13.25 mm.

Along the lateral side of 88 mm length, the geometry based position sensitivity is provided by using the ratio of detected amount of light in both trapezoids. The position sensitivity along the lateral side will be referred to as y-direction.

Position sensitivity along the scintillator side of 300 mm is obtained by using the propagation time of light and is referred to as x-direction. In total the position sensitive area of the prototype detector is 264 cm^2.

Each trapezoid is equipped with five WLS-fibers, as indicated in Figure 6.2. This is motivated firstly by the idea of optimizing the collection of the path length dependent amount of light. Secondly, to be able to normalize the detected amount of light in each trapezoid separately and thirdly to investigate the detected amount of light per event with reference to the fiber position in the scintillator.

The fibers are located in grooves, which are milled in the lateral side of the trapezoid. The grooves have a width of 1.7 mm and a depth of 1.5 mm. The spacing between each of the grooves as well as the outermost grooves and the edges of the scintillator is 13.25 mm.

All grooves are equipped with fibers of type BCF 92 [34] with a diameter of 1.0 mm, except for the groove in the middle of each trapezoid. This fiber is 1.5 mm in diameter for both trapezoids.

The WLS-fibers are glued into the scintillator with BC 600 [33] optical cement. All fibers are equipped at one end with a FC-plug [24]. The opposite end is open for all fibers. This leads to a single side readout of each trapezoid. The trapezoids are optically insulated from each other by one layer of aluminum foil. This leads to a directed light reflection at the sides of the scintillator.

In Figure 6.3 one readout side of the POSSuMUS detector is shown, where each fiber is connected to one SiPM to form one readout channel. The coupling is realized with FC-plugs and FC-sockets, whereby all fibers describe a bending radius before they are connected to the photon counter. There
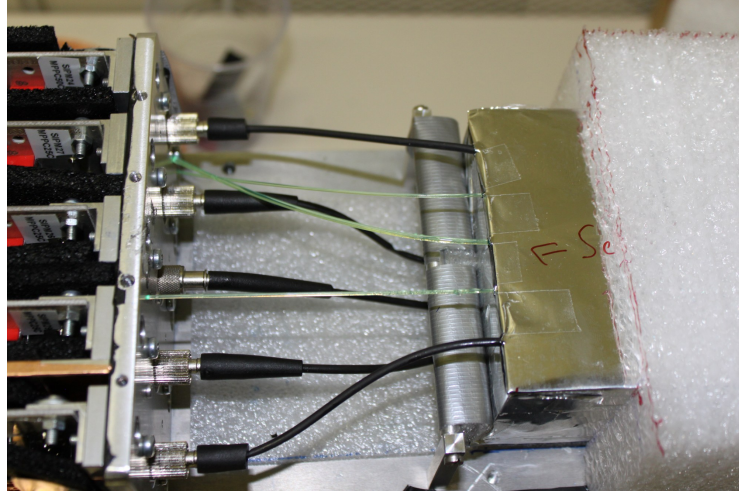
Figure 6.3: A readout side of the POSSuMUS prototype detector is shown: Five fibers are connected to five SiPMs, via FC-coupling. The fibers describe a bending radius before being connected to the SiPMs. The open ends of the WLS-fibers , which are connected to SiPM at the other readout side, are visible. The scintillators are wrapped in aluminum foil for directed reflection.

is no optical grease included between fiber and SiPM. The box contains in total ten SiPMs, whereby five SiPMs are mounted at each side of the detector. The detector is mounted in a light tight aluminum box. On each side of the detector one temperature sensor of type DS18B20 [63] is installed and allows to monitor the temperature during the experiment. The sensor is not visible in Figure 6.3.

Each SiPM within the light tight box is connected to one channel of the serial voltage divider, see Chapter 4.2.1. The serial voltage divider is used to set the bias voltage U_{bias} separately at each SiPM to apply the same over-voltage U_{Over}, ensuring identical gain-values at all SiPMs. The global voltage for the voltage divider was provided by a Keithley 2400 source [44], which was controlled remotely. Each SiPM board receives 5 V supply voltage for the pre-amplifier BGA614 [39] from one output channel of the TL200 [1] power supply.

All SiPMs were characterized before being installed with the method, described in Chapter 4. Hamamatsu SiPMs [36] with an active area of 1×1 mm^2 were used. The pixel size was $(50\,\mu m)^2$, which leads to 400 pixels per mm^2. For this experiment, the gain was determined for each SiPM and measurement, see Section 6.4.1. In contrast to later measurements, there was no active gain stabilization installed.

6.2 Data Acquisition for CERN-Experiment

The data acquisition was realized with a standard VME-based [77] V1729 [71] Flash Analog to Digital (FADC) readout. The FADC is capable to record 2500 data samples consecutively with a sampling rate of either 1 or 2 Ghz. This leads to a time windows of either 2.5 μs or 1.25 μs. Three FADC modules V1729, with four channels each, were combined to record ten SiPM channels of the detector. The remaining two channels were used for the coincidence trigger. The schematic of the data acquisition is displayed in Figure 6.4.

All ten SiPM signals were fed directly from the SiPM to the FADC modules. To trigger the data acquisition two scintillators, consisting of two 100 mm $\times$ 25 mm $\times$ 10 mm (Length $\times$ Width $\times$ Height) plastic-scintillators which are coupled to standard Hamamatsu photomultipliers [38] were used. The photomultiplier signals were fed to a CAEN Low Threshold Discriminator (LTD) [69] to generate standard NIM-Pulses with a signal width of 10 ns. These signals are given to a coincidence unit. A
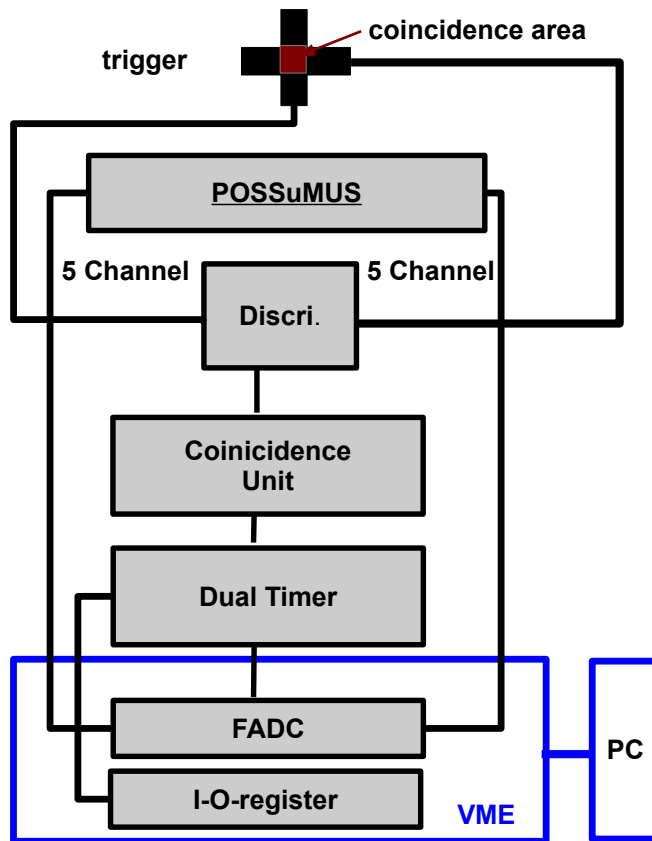
Figure 6.4: The data acquisition for ten readout channels of the detector was provided by a V1729 [71] VME-based Flash-ADC readout in combination with an external coincidence trigger to start the data acquisition. The coincidence area is formed by crossing two plastic scintillators.

coincident signal is given to a dual timer unit [70] to start the data acquisition. After one trigger, the dual timer inhibits further trigger events until the FADC-data are read-out by a PC. After finishing data transmission a reset signal is sent from an input-output register [75] and activates the dual timer again for new event trigger.

The advantage of the FADC-readout is to record the time resolved signal shape of each SiPM-response. On the one hand it is possible to extract the signal height information of the signal shape for each event and determine the detected amount of light for the position sensitivity in the y-direction. On the other hand the starting point of the signal can be extracted from the recorded data to calculate the time differences for the position sensitivity in the x-direction.

6.3   Experimental Setup for Prototype I

6.3.1   Detector Position

In Figure 6.5 the experimental setup at the H6 beam-line in Prévessin is shown. A 120 GeV pion beam was provided at this beam line. Due to the spill structure of the beam only ten seconds out of a minute the beam was guided to the experimental site. The remaining fifty seconds the beam from the SPS synchrotron was used for other purposes like fixed target experiments or filling the LHC. The detector is mounted in an aluminum light tight box and resides on a height adjustable lift table. The particle beam enters from the left side and the white area indicates the sensitive area of the detector, see Figure 6.5. In Figure 6.6 the default position of the detector within the light tight box is shown
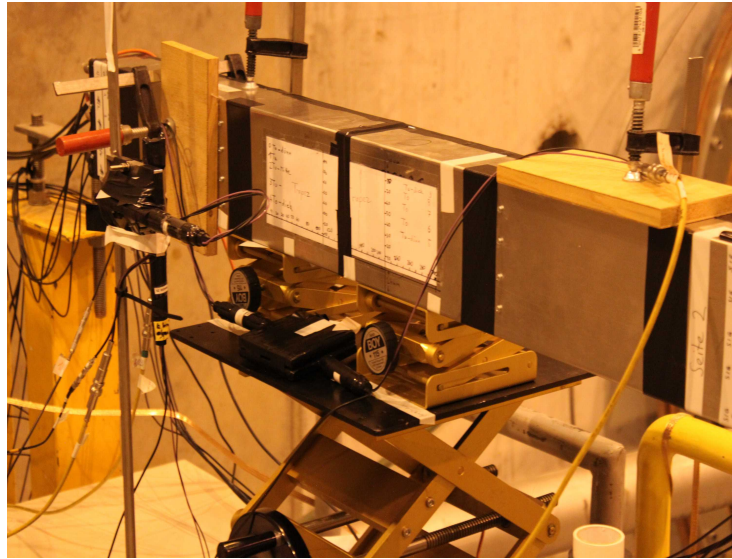
Figure 6.5: Setup at the experimental site H6, located at the north area of CERN: The POSSuMUS detector resides in a light tight aluminum box and is positioned to beam-height. During the experiment, the detector can be moved in vertical and horizontal direction, to test the position sensitivity in the x- and y-direction.
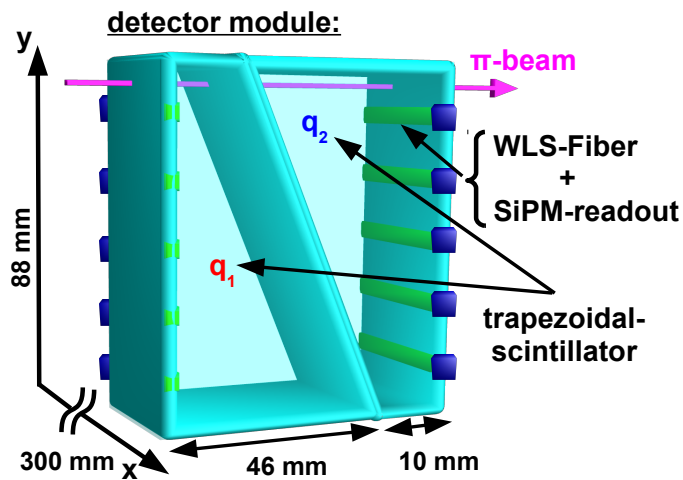
Figure 6.6: The detector is in the default orientation and the particle beam comes from the left side. Hence the pions are traversing both trapezoidal scintillators. The single side readout of all fibers is indicated by blue SiPMs. [61]

to investigate the position sensitivity of POSSuMUS. The coincidence trigger was located in front of the detector on beam height, see Figure 6.5. The trigger area was realized by crossing two trigger scintillators with an active coincidence area of $(10 \text{ mm})^2$. The position of the trigger cross was fixed during the experiment.

The light tight box is moved in vertical and horizontal direction to scan the whole detector and investigate the position sensitivity in two dimensions. In Figure 6.7 a close up look of the sensitive detector area is shown, the colored dots represent different detector positions with reference to the beam position. The red circle indicates the position of the coincidence trigger in front of the detector.
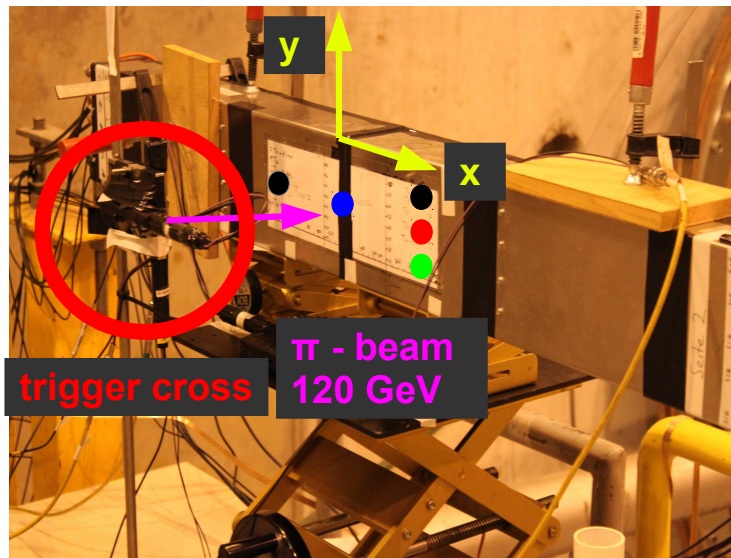
Figure 6.7: Close up look of the light tight box: The white area indicates the sensitive volume of the detector. The colored dots indicate different beam positions to test the position sensitivity either in x- or in y-direction. In front of the detector the coincidence trigger is visible. The 120 GeV pion beam arrives from the left.

An event display for one pion traversing the detector is shown in Figure 6.8. In the left column all signal shapes for channels in trapezoid q_1 are displayed and in the right columns the response of all SiPM connected to trapezoid q_2 are shown. For all channels the characteristic shape of SiPM-signals is observable. The baseline reveals a normal noise level. In the time window dark rate events are observable before or after the pion event. The measurement of one beam position with 10000 Events took about 20 minutes, due to the rate of the FADC-readout of about 50 Hz and the spill structure of the beam, described above.
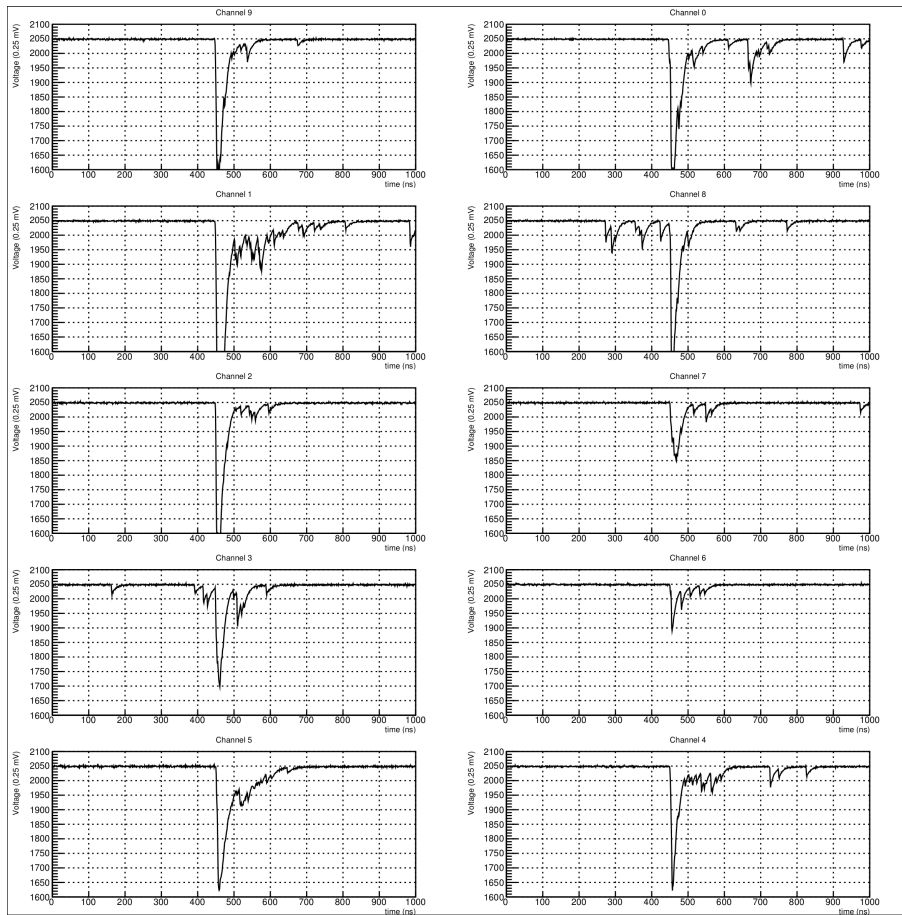
Figure 6.8: Event display for one Pion event in POSSuMUS: In the left column all signal shapes for channels in trapezoid q_1 are displayed and in the right columns all SiPM response connected to trapezoid q_2 are shown. For all channels the characteristic shape of SiPM-signals is observable, For some channels dark rate events are observable before or after the pion event

6.3.2   Verification of the Trigger Position
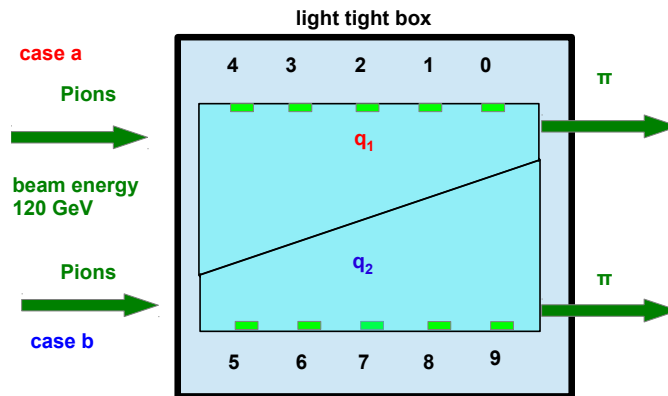
Figure 6.9: Verification of the trigger position: A cross-section of the light tight box is shown, which is rotated by 90° about the x-axis with respect to the default positions. In this position both scintillators face towards the pion beam. This setup is used to verify the position of the trigger cross with reference the to mounted detector.

To test the position of the trigger cross with reference to the mounted POSSuMUS detector, the light tight box was rotated about the x-axis by 90°, so that both trapezoids face toward the Pion beam. After adjusting the correct height of the detector with reference to the trigger cross, pions can traverse only one trapezoid without interacting in the other scintillator. The experimental setup is displayed in Figure 6.9, whereby **case a** corresponds to the setup where scintillation light is only created in trapezoid q_1 and **case b** corresponds to the adjustment that pions traverse trapezoid q_2
In Figure 6.10 and 6.11, for case **case a**, one signal height spectrum of channel four in trapezoid q_1 and one signal height spectrum of channel nine in q_2 are displayed.

As expected from the experimental setup, a continuous signal height spectrum is observable in Figure 6.10, which represents the detected amount of light, which was collected by the WLS-fiber and detected by the SiPM. In contrast, only dark rate events are visible in Figure 6.11, which correspond to the zero, one and two pixel peak.
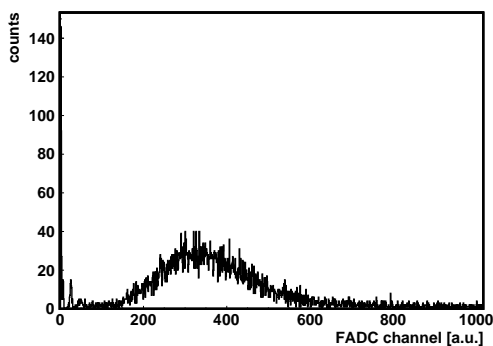
Figure 6.10: The pion beam interacts only in the upper scintillator (**case a**), light is detected in channel four which is located in the upper scintillator at the thick side of the trapezoid.
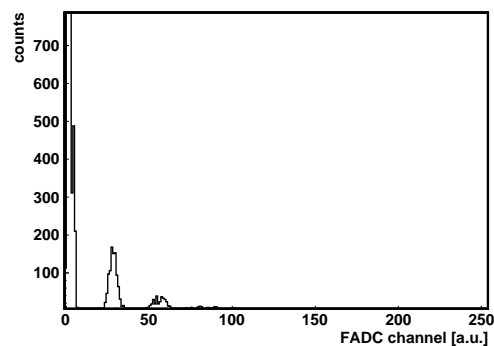
Figure 6.11: The pion beam only traverses the upper scintillator, therefore no light is detected in channel nine which is located on the thick side of the lower scintillator.

For **case b**, these measurements were repeated and showed the same results. In this case scintillation light is created in trapezoid q_2.

By these measurements the position of the trigger cross with reference to the horizontal position of the detector is determined. Moreover these measurements confirm, that the trigger cross selects a part of the pion beam and each coincidence trigger corresponds to one pion which traverses the detector. There are no other pions which are traversing simultaneously the detector. This is also visible in the event display of Figure 6.8.

6.3.3 Temperature Monitoring

The temperature was monitored at both sides of the detector with one temperature sensor each, close to the mounted SiPMs.

The temperature variation recorded on the October 26th 2012 is shown as an example in Figure 6.12. The sensors were only read-out when measurements were recorded.

The temperature changes are in the order of $1.5\,^\circ$C over the whole day. Since, no active gain stabilization system for the SiPMs was available, during this experiment, the gain of each SiPM was determined for each measurement separately, as described in Section 6.4.1.
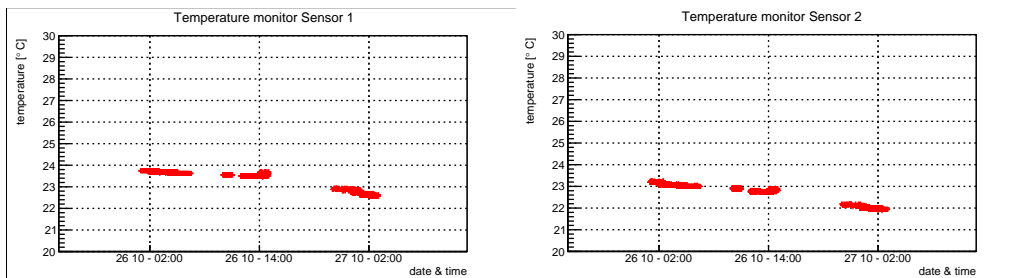
Figure 6.12: The temperature profile for October 26th, at both sides of the detector, close to the mounted SiPMs. The temperature changes over the whole day for about $1.5\,^\circ$C. Within several measurement periods the temperature stays constant. Since no gain stabilization is present for SiPMs, the gain values are determined for each measurement period to correct the signal height information of each SiPM.

6.4 Detector Adjustment

6.4.1 Determination of the SiPM Gain

The signal height is determined by the incoming amount of photons at the SiPM and the gain value of the SiPM.

Before being mounted at the detector each SiPM was characterized. The breakdown voltage U_{bd} was determined via the method, described in Chapter 4.1. By using a serial voltage divider, described in Chapter 4.2.1, the same over voltage U_{over} of 1.0 V was adjusted at each SiPM, whereby the gain values of all SiPMs are expected to be similar when working with the same voltage U_{over}. However, variations in the gain factors between several SiPMs can either be caused by the accuracy of the serial voltage divider, where the accuracy is about 10 mV or by the measurement uncertainty of the U_{bd}-voltage, which is about 70 mV, see Section 4.1.2.

By knowing the gain value it is possible to adjust the signal height information between different channels correctly and to calculate the number of detected photons per SiPM.

Hence it is essential to know the gain value and the variation of the gain for each SiPM during the experiment. As described in Chapter 4, the gain of each SiPM is determined by fitting several

signal height spectra

Gain of Detector Channels
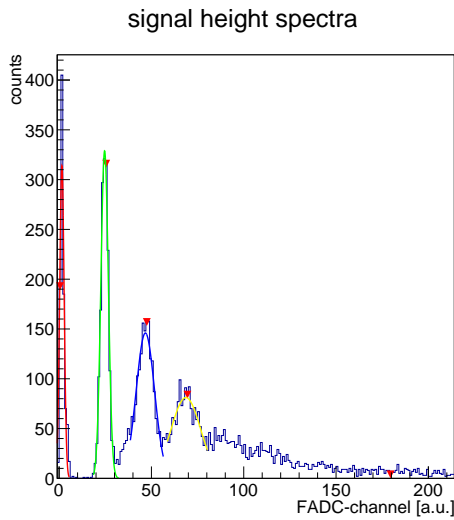
Figure 6.13: Determination of the gain value for one channel of POSSuMUS: The Gain is determined by fitting Gaussian distributions to the first four peaks of the spectrum and calculating the difference between the mean values. This is an example for channel seven, when pions are traversing the detector.
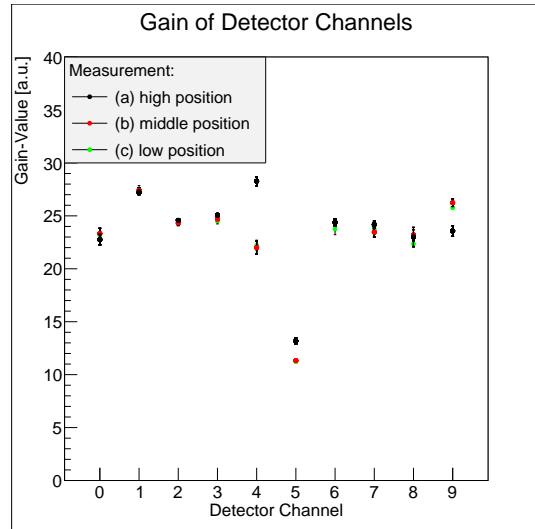
Figure 6.14: Gain values for all ten SiPMs and three different measurements are shown: The gain values are similar for several channels with a spread of 10 %. The colored dots represent three different measurements, which were taken within 24 hours where only a small variation is visible due to small temperature changes of the environment. Channel 5 shows a lower gain, by a factor of two, due to a malfunction at the serial voltage divider.

Gaussian distributions to the peak structure of a signal height spectrum of each SiPM and calculating the difference between neighboring peaks. For that purpose we either use scintillation light spectra, where the peak structure is clearly visible, see Figure 6.13, or dark rate spectra, as visible in Figure 6.11.

In Figure 6.13, four peaks are used to calculate the gain value. This signal height spectrum corresponds to one channel of the POSSuMUS detector for a measurement of 10000 pion events.

In Figure 6.14 the gain values of all ten channels of POSSuMUS are plotted. The error of the gain-value is calculated from the fit error of the Gaussian means, whereby the typical uncertainty is 0.2a.u.. The gain values were determined for three different measurements. This is indicated by the colored dots in **a**, **b** and **c**, whereby each color corresponds to one detector position described in Figure 6.7.

The measurements were recorded over several days. Due to possible temperature changes, as shown in Figure 6.12, the gain values were determined for temperature dependent variations for each measurement and channel.

For measurement **b** and **c** the gain factors vary between $(25 \pm 2.5 \text{ a.u.})$. The variations of only 10 % verify that both the characterization of the breakdown voltage U_{bd} and the voltage adjustment of the serial-voltage divider is reliable.

The low gain with a value of $(11.41 \pm 0.59 \text{ a.u.})$ for channel five is the result of a malfunction of this channel at the serial voltage divider. The adjusted voltage did not correspond to the applied voltage at the SiPM and therefore the gain factor is smaller.

Observable gain variations are obvious at channel four, five and nine for measurement **a**. These are due to a manual change of the bias voltage at the serial voltage divider during the experiment.

6.4.2 Light Collecting Characteristics
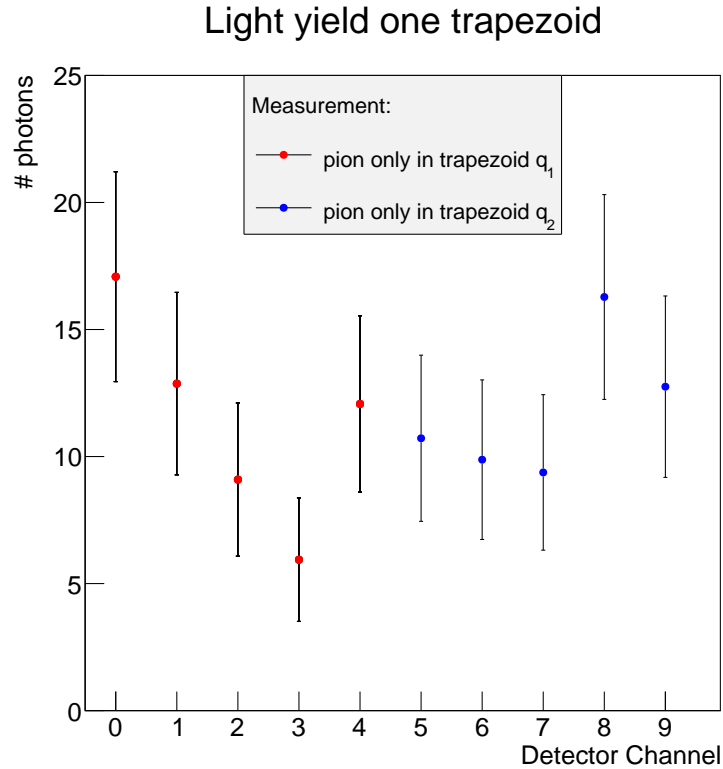
Figure 6.15: Detected light yield in q_1 and q_2, corrected for different gain values, for **case a** and **case b**, when the beam only hits one trapezoid. The trapezoid with no scintillation light is used for gain determination of each SiPM. The detected amount of light per channel varies between 6 to 17 photons. The highest light output is observable for channel zero and eight, whereby the lowest amount of light is measured for channel three.

The measurements presented in section 6.3.2, which were used to verify the trigger position with reference to the detector position, allow to further investigate the light collecting characteristics of all channels of the detector.

For the setup, shown in Figure 6.9, the scintillator path length for pions is 88 mm, about a factor two larger than in the default orientation, see Figure 6.6. Moreover the distance between the path of the pions and the location of the fiber is the same for all fibers in one trapezoids, in contrast to the setup in Figure 6.6. Therefore. fibers located at the same geometric position in the upper and lower trapezoid are expected to detect a similar amount of light with a small variation due to the light reflected from the inclined side of the trapezoid which is collected mainly by channel four and nine.

The gain values of all channels for these measurements were determined out of the dark rate spectra, for an example see Figure 6.11. Therefore the gain values for channels in trapezoid q_1 were determined out of dark rate spectra of measurement **case b**, and gain values of trapezoid q_2 out of dark rate spectra of measurement **case a**. Gain values remain constant between both measurements, since they were recorded within two hours, see Section 6.3.3. To evaluate the number of detected photons the signal height spectra of all channels are fitted by a convoluted Landau Gaussian function. The number of detected photons is given by the most probable value of the fit, divided by the SiPM gain of the channel under investigation.

The number of detected photons for each channel is plotted in Figure 6.15. The detected amount of light differs between 6 to 17 photons for all ten channels. Most of the channels reveal a number of detected photons between 9 to 13 photons. The channels zero and eight show a higher number of

above 16 photons , whereas channel three exhibits the lowest detected amount of only 6 photons.
If one compares channels, which are located at the same geometrical positions in both trapezoids, it
is visible that the largest difference in light detection is found between channel three and eight/zero.
In contrast, channel four and nine reveal a similar light yield.

Differences in the detected amount of light between different channels can originate from an imperfect gluing, a faulty coupling of the fiber to SiPM or from a too tight bending of the fiber.

6.5   Results for the First POSSuMUS Prototype

To validate the geometry based position sensitivity of the detector and to determine the spatial resolution, measurements were performed at three different beam positions, referred to as **a**, **b**, and **c**.
These measurements were located at the right edge of the detector, with reference to the direction of
the pion beam, see Figure 6.16. The POSSuMUS detector is mounted in the default positions. Hence
the pion beam traverses both scintillators, indicated in Figure 6.17.
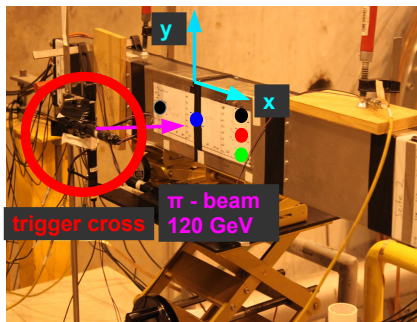
Figure 6.16: The black, red and green dots indicate three different beam positions to test the position sensitivity in the y direction. The 120 GeV pion beam arrives from the left.
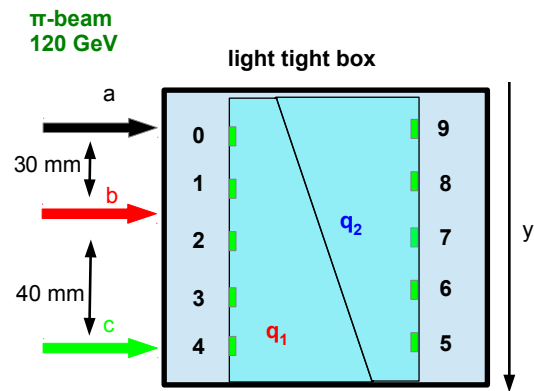
Figure 6.17: Cross section of the aluminum box: The pions traverse both scintillators. By **a**, **b**, and **c** the three different beam positions are indicated to investigate the position sensitivity of the POSSuMUS detector, due to the trapezoidal shape.

The amount of collected scintillation light depends on the amount of created scintillation light
due to the path length in the trapezoid and additionally on the absorption of created photons
in the scintillator.   The absorption of created photons depends on the distance between fiber
and traversing pion.   Fibers at the thick side of the trapezoid reveal a better position sensitivity,
because the created amount of scintillation light decreases and the absorption of created photons
increases with increasing distance to the fiber.   Therefore, the decrease of detected photons with
decreasing path length is enhanced.   On the other hand, the position sensitivity of channels at
the thin side is worse because the amount of created scintillation light increases and the absorption increases with increasing distance to this fiber and therefore the position sensitivity is washed out.

6.5.1   Detected Light per Channel

For each recorded pion event the maximum signal height is determined from the signal shapes, see
Figure 6.8 and filled into a signal height spectrum separately for each channel and position.

In the case of a continuous signal height spectrum which corresponds to a detected amount of light
larger than five photons, the distribution is fitted by a convoluted Landau-Gaussian function, see Figure 6.18. To determine the number of detected photons the **M**ost **P**robable-**V**alue (MPV) of the fit is
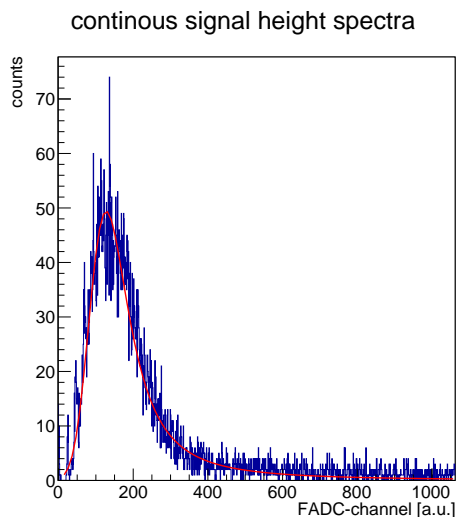
Figure 6.18: Continuous signal height spectrum of one channel of POSSuMUS: This distribution can be fitted with a convoluted Landau-Gaussian function, to determine the number of detected photons.
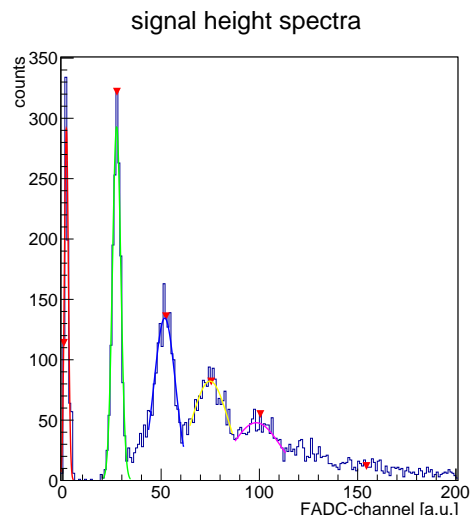
Figure 6.19: Signal height spectrum with multiple peak structure: Each peak corresponds to the number of detected photons. This spectrum can be described by Poisson statistics and the Poisson mean value corresponds to the number of detected photons.

divided by the gain value, evaluated for the channel under investigation, see section 6.4.1.

If the signal height spectrum shows a multiple peak structure, see for example Figure 6.19, the detected amount of light is evaluated by using the Poisson mean value of this distribution. Therefore the light yield can be expressed in number of detected photons. The detected number of photons is displayed for all channels of the POSSuMUS detector in Figure 6.20. The light yield was evaluated separately for each of the three beam positions, indicated in Figure 6.17.

Firstly the behavior of the detected amount of light for channel zero is described. This channel is located at the thin side of q_1, see Figure 6.17. It reveals a detected amount of light of five photons for measurement **a** and **c**. For position **b**, this channel shows a slightly lower light yield. Thus no path length dependent amount of light is observable.

The behavior of the detected light yield is different for channel four. This channel is located at the thick side of trapezoid q_1 and exhibits a detected light yield of 2 photons for measurement **a**. For beam position **b** the detected photon number increases to 4 photons. For case **c** , where the scintillator path length is further increased, the detected light enhances to about 6.5 photons. This channel reveals a path length dependent light output, which is essential to reach a position sensitivity for minimal ionizing particles. The differences are statistically significant, since the presented values correspond to the mean values for 10000 recorded pion events per measurement.

For the second trapezoid, the same characteristics for equivalent channels are observed. Channel five, which is located at the thin side of q_2 shows almost no variation of the light yield, when changing the position of the pion beam. In contrast, the light yield detected by channel nine is path length dependent and varies from 2 to 6 photons for measurements **a**, **b** and **c**.

Thus channel four and nine reveal a path length dependent light output due to the trapezoidal shape of both scintillators.

Similarly, a variation in the detected light yield is observed at channels eight and three, when measuring at different beam position. However, the detected number of photons for channel three is a factor two smaller than for channel eight. Possible reasons for the smaller light output in channel three can be either an imperfect gluing or a faulty coupling of the fiber to the SiPM. The difference in the detected photon numbers for these channels is consistent with the results presented in Figure
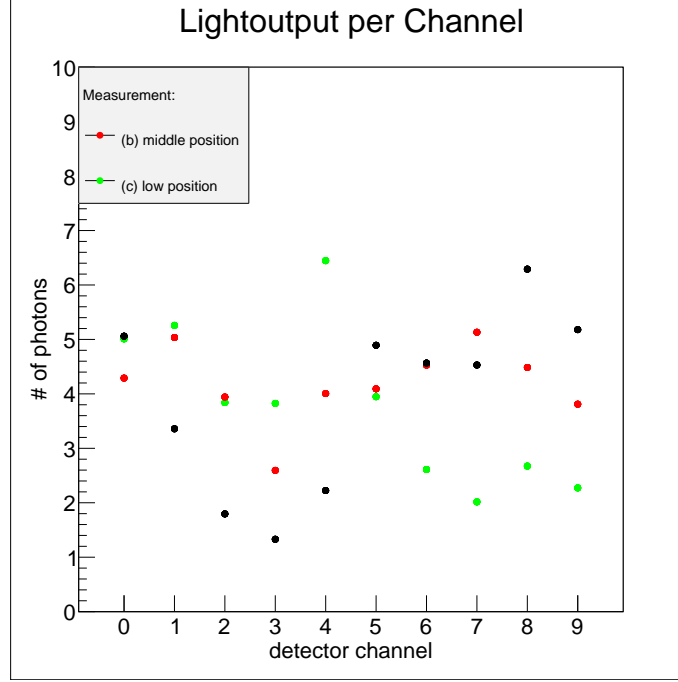
Figure 6.20: Detected number of photons for all channels of the POSSuMUS detector, separately for beam position **a**, **b**, and **c** indicated in Figure 6.16. No path dependent amount of light is observed for channels located at the thin sides of the trapezoidal scintillators of the POSSuMUS detector. Channels at the thick edge (four and nine) detect an increasing number of photons for increasing path length. No error bars are shown, due to the low number of detected photons.

6.15.

Only partial sensitivity of the detected amount of light to the beam positions is observed in the remaining channels one and two, in q_1 and channel six and seven in q_2. The calculated number of photons for channel two and seven must be treated with caution, since these fibers have 1.5 mm in diameter, resulting in a larger active area of the fiber. However, the scintillation light of the fiber is lost, when the photons hit the SiPM outside of the active area of (1×1) mm^2.

In summary, fibers at the thick side of each trapezoid show a path length dependent light output, the number of detected photons increases with the increasing path length. In contrast to this, fibers at the thin side of the trapezoid show almost a constant light output, with no dependence on the path length. The channels in the middle of the detector show a transition from path length dependent to path length independent behavior. The reason for this behavior is the described correlation between the path length dependent amount of created scintillation light and the absorption of photons in the scintillator, which depends on the distance between the fiber and the track of the traversing pion, see section 6.5.

6.5.2   Detection Efficiency per Channel

After the discussion of the detected amount of light per channel the detection efficiency per channel is evaluated in the following.

The detection efficiency of the position sensitive channels is a key characteristic, since the determination of the pion position is only possible, when all position sensitive fibers detect photons for each event. The detection efficiency ε can be determined by the number of detected particles N_{light} in the detector and the number of particles that crossed the detector $N_{particles}$:

$$\varepsilon = \frac{N_{light}}{N_{particles}} = \frac{N_{light}}{N_{light} + N_{no\ light}} \tag{6.1}$$

Since the number of not detected particles $N_{\text{no light}}$ corresponds to the number of entries in the zero pixel peak, see Figure 6.21 and $N_{\text{particles}}$ is the number of entries in the histogram. Therefore the efficiency ε is defined by the following relation:

$$\varepsilon \;=\; 1 \;-\; \frac{N_{\text{no light}}}{N_{\text{particles}}} \tag{6.2}$$

Since the numbers of $N_{\text{particles}}$ and $N_{\text{no light}}$ are independent, its error can be calculated from Gaussian Error propagation assuming Poisson statistics. The error of the efficiency is calculated as:

$$\Delta\varepsilon \;=\; \sqrt{\frac{\varepsilon \;\cdot\; (1 \;-\; \varepsilon)}{N_{\text{particles}}}} \tag{6.3}$$

In Figure 6.22 the efficiencies for each channel are plotted, evaluated at the same beam positions **a**, **b** and **c** used to determine the detected light yield, see Figure 6.17.

For channels at the thin side of each trapezoid, namely channel zero in q_1 and channel five in q_2, the
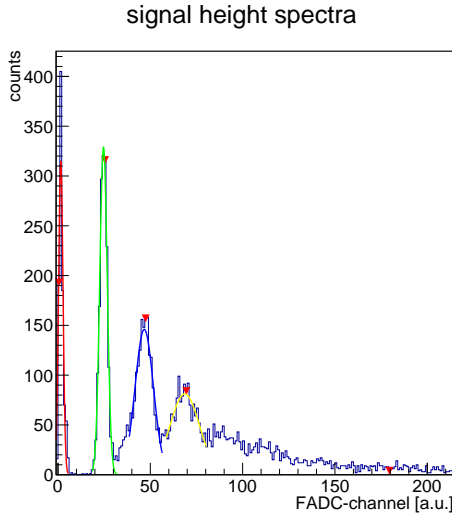
Figure 6.21: Determining the detection efficiency of each channel: To determine the no light events, a Gaussian distribution is fitted to zero pixel peak, and the integral of entries is evaluated.
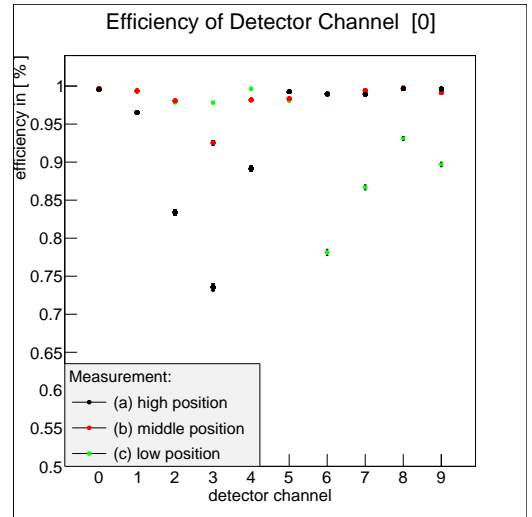
Figure 6.22: Detection efficiency for each channel of POSSuMUS: A decrease in efficiency is visible for position sensitive channels for beam position at the thin side of each trapezoid.

detection efficiency is above 95 % for beam positions **a**, **b** and **c**.

Channels one and two also reveal a detection efficiency above 95 % for beam positions **b** and **c**. However, a decrease of the detection efficiency is observable for beam position **a**. The lower efficiency arises in combination with a lower detected amount of light in comparison to the other beam positions, see Figure 6.20. The same results are observable for equivalent channels in trapezoid q_2 and the corresponding beam positions.

The decrease of the detection efficiency in combination with a lower detected amount of light is also visible for position sensitive channels in both trapezoids. Channels four and nine reveal a detection efficiency above 95 % for beam position **c** and **a**, respectively, and for both channels at beam position **b**. However, a decrease of the detection efficiency below 90 % for beam position **a** and **c** is visible. These characteristics are also observable for channels three and eight, whereby channel three exhibits the lowest detection efficiency of only 74 % because of the lowest detected amount of photons.

The behavior of the detection efficiency for position sensitive channels will lead to a lower efficiency at the beam positions **a** and **c**, when determining the position sensitivity of the detector.

Summarizing this section, the position sensitive fibers in each trapezoid are less efficient when the pion traverses at the far thin side of the trapezoid, due to the small detected amount of light. The efficiency for position insensitive fibers at the thin side remain above 95 % for all trigger positions. The calculated efficiencies are not corrected for dark rate effects, which arise by the SiPM-response. Dark rate effects can be excluded by using only events with more detected photons. This is not applicable to the measurement with this first prototype because of the low light output per event.

6.5.3   Position Sensitivity of the Detector
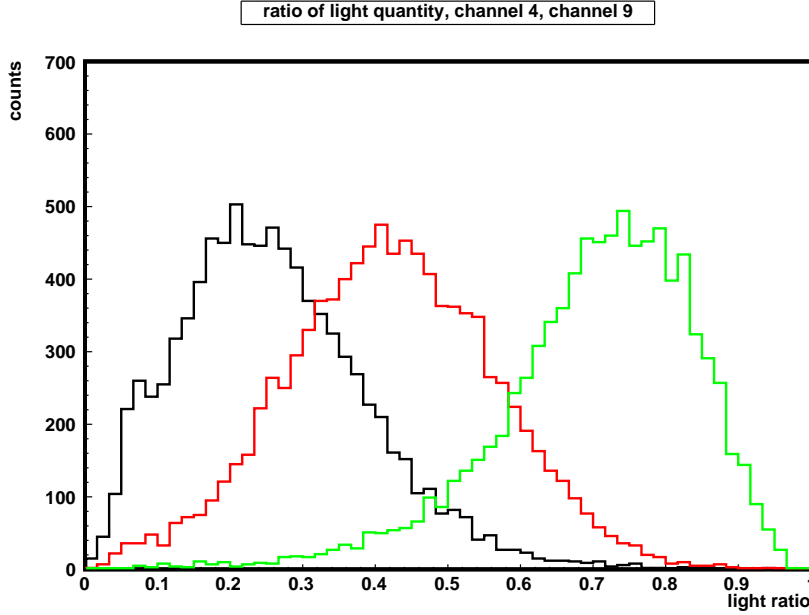
Figure 6.23: Position Sensitivity of the POSSuMUS detector: Calculating the light yield ratio (pos(y)) for three different beam positions leads to three separable peaks. The mean values of the distribution are located in accordance with the beam position **a**, **b** and **c**. The spatial resolution is in the order of 20 mm and mainly limited by the low photon statistics. The number of entries for each distribution differ due to the degradation of detection efficiency at the edges of the detector.

The y position of traversing particles is calculated by normalizing the amount of light in trapezoid q_1 by the sum of the detected amount of light in trapezoid q_1 and q_2, see Equation 2.1.

- amount of light in trapezoid one: $q_1 = \sum$ (position sensitive channels in q_1)

- amount of light in trapezoid two: $q_2 = \sum$ (position sensitive channels in q_2)

$$\text{pos(y)} = \frac{q_1(y)}{q_1(y) + q_2(y)} \tag{6.4}$$

The range of values for the light ratio of both trapezoids, with the given geometry, see Figure 6.1 is:

$$\text{pos(y)} \in [0.18 - 0.82] \tag{6.5}$$

with the assumption of a linear correlation between the path length of the crossing pion and the detected amount of light. A variation of 1 mm in the y-direction corresponds to a variation in the light ratio (pos(y)) of 0.007.

Since only channel four in trapezoid q_1 and channel nine in trapezoid q_2 show a comparable path length dependent light output, the position of crossing pions is calculated by considering only these

channels. The other channels, zero to three in q_1 and five to eight in q_2 are not used, since they either do not reveal a path length dependent light output (channels zero, one, five and six) or the detected amount of light for equivalent channels in both trapezoids, namely channel three and eight, differs largely. For the application of POSSuMUS this is a realistic starting point, since for large area applications of POSSuMUS the number of electronic channels shall be as small as one SiPM per trapezoid only.

In Figure 6.23, the distributions of the light ratio for three different measurements is presented. Three separable peaks are observable, which are in accordance to the beam positions **a**, **b** and **c**, indicating the position sensitivity of the detector.

The mean value and the standard deviation for beam position **b** is determined by fitting a Gaussian distribution. To describe the asymmetric shape of the distributions **a** and **c**, the Crystal Ball-function is used, defined in Appendix A.3 from [53] and [29] for determination of the mean value and the standard deviation.

In Table 6.1 the results of the fit and the detection efficiencies are presented. In the second column

pos(y)	expected value	mean value	$\pm\ \sigma$ error	detection efficiency
measurement **a**	0.22	0.23	0.13	89%
measurement **b**	0.43	0.44	0.15	97%
measurement **c**	0.73	0.74	0.13	88%

Table 6.1: For three measurement **a**, **b** and **c**, the expected value, the mean values, the standard deviation and the detection efficiencies are listed, extracted from Figure 6.23. The expected value is calculated by the path-length ratio within both trapezoid. The assumption is, that there is a linear correlation between path length and detected amount of light.

the expected values of the light ratio for the beam positions, **a**, **b** and **c** are displayed. The third and fourth column correspond to the mean values and standard deviations of the described fits.

The expected value of measurement **b** corresponds well to the measured value. The standard deviation of 0.15 corresponds to a spatial resolution of 21.4 mm for measurement **b**.

The expected values for beam positions **a** and **c** correspond to the mean values presented in Table 6.1 with a discrepancy of about 3%. This discrepancy can be explained by an inexact measurement of the beam position with reference to the detector positions or by the broad spatial resolution. The spatial resolution for these measurements are also in the order of 20 mm.

In the 5th coloumn of Table 6.1 the detection efficiencies for the three measurements are presented. The detection efficiencies decrease between position **b** and position **a** and **c** by about 9 %. This drop of the detection efficiencies is explainable by the drop of the detection efficiency for the position sensitive channels when the pion traverse at the thin side of the trapezoid,see Section 6.5.2 and Figure 6.22.

Due to the fact that only one out of five channels per trapezoid is used for the determination of the position sensitivity and the amount of detected photons per channel is in the order of 2-6 photons per event, the spatial resolution and the detection efficiency is mainly limited by the low amount of detected photons, discussed in Section 2.1.2.

6.5.4 Position Sensitivity of the Complete Detector Area

To investigate the position sensitivity over the whole detector area of 264 cm^2, the measurements presented in Section 6.5.3 were repeated at the center position and at the left edge of the detector with reference to the beam direction, as indicated in Figure 6.24.

At the center position additional measurement points were recorded, whereby the distance between several beam positions is 10 mm or 20 mm as indicated in Figure 6.25. The light ratio (pos(y)) are shown in Figure 6.26, evaluated for all measurements at the center position. The
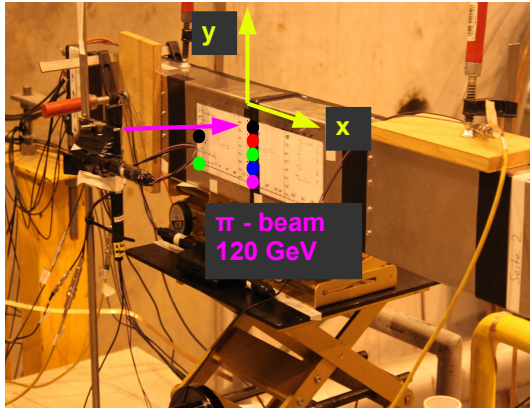
Figure 6.24: The POSSuMUS detector at the H6 experimental site. The colored points indicate a precise scan in y direction at the center of the detector. Also shown are two measurements at the left edge of the detector. The pion beam arrives from the left side.
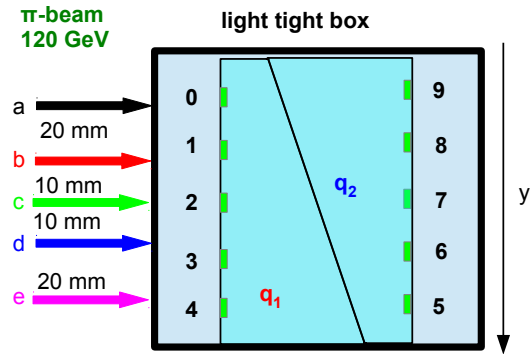
Figure 6.25: Cross section of the aluminum box: The colored arrows indicate beam positions used for a precise scan in y-direction to reveal the position sensitivity of the POSSuMUS detector in the center of the detector.

position sensitivity of the detector is observable, since the mean value of the distributions vary, depending on the y-position of the beam. The distribution of measurement **c** corresponds to the y-position, where the path lengths are equal in both trapezoids and therefore the light ratio, see Equation 2.1 results in the value of 0.5. The mean value of distribution **b** and **d** are located symmetrically around the **c** distribution, as expected from the shift of 10 mm to both sides. This is also valid for the
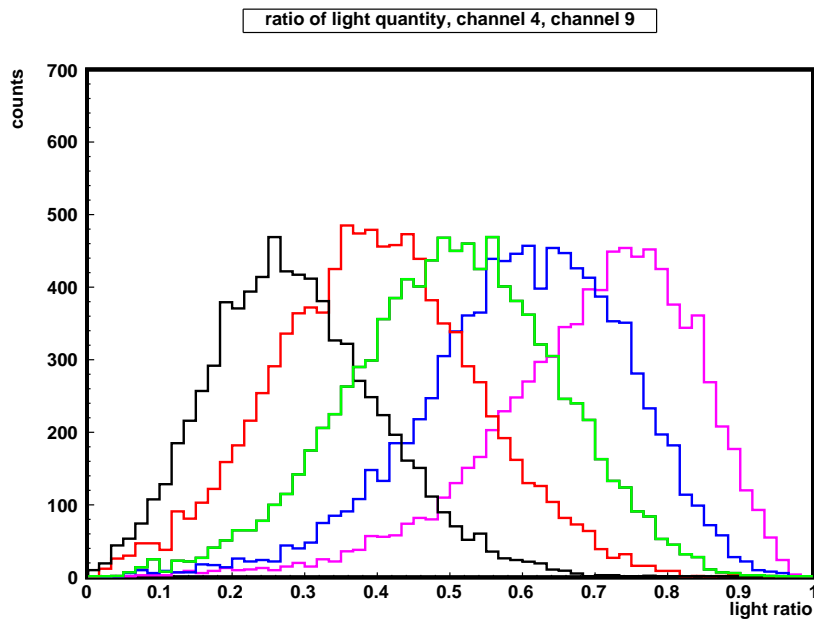
Figure 6.26: Measurements at the middle position of POSSuMUS: Light ratio pos(y) obtained for a precise y-direction scan at the middle detector position. The different colors correspond to the beam positions indicated in Figure 6.24. The position sensitivity of the detector is observable. The mean value of the light ratio depends on the y-position. For measurement **c** the path length in both trapezoids is equal. Therefore the light ratio results in 0.5.

larger shift of 20 mm for measurement **a** and **e**. The standard deviation of measurement **c** is 0.145, which corresponds to a spatial resolution of 20.71 mm.

This is also visible in Figure 6.26, since the distributions of measurement **c**, **a** and **e** are clearly separable and the distance of the beam positions is 20 mm.

The results obtained for two measurement points at the left edge of the detector are consistent with those presented in this Section. The corresponding plot of the light ratio (pos(y)) can be found in Figure A.3 in Appendix A.

6.5.5 Position Sensitivity along the Detector
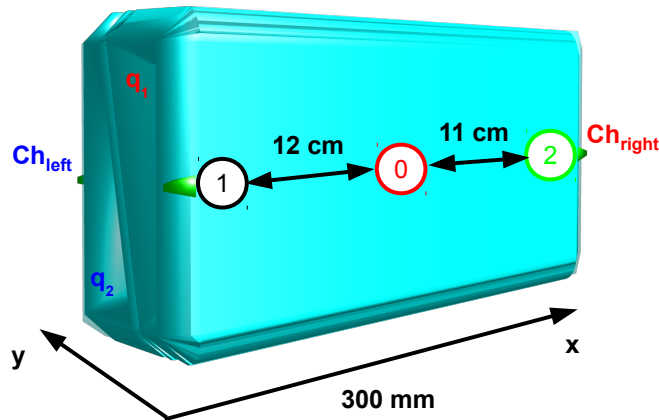
Figure 6.27: Schematic for the test of the position sensitivity along the length of the scintillator (x-direction): The colored points indicate the measurements for testing the position sensitivity due to the propagation time of light, measured by two readout channels which are located at opposite sides and different trapezoids. These measurements correspond to the colored dots in Figure 6.16.

The detector is capable to measure a second position coordinate with the presented detector design, described in section 6.4. The position information is determined using the propagation time of light in the scintillator.

To investigate the position sensitivity in the x-direction, the experimental setup described in Section 6.3 and the data acquisition system described in Section 6.4 were used. The FADC-modules [71] worked with a sampling frequency of 2 GHz, which leads to an active time window of 1.25 μs for 2500 data samples. The time resolution for this readout electronic is 0.5 ns.

Two channels located at opposite sides of different trapezoids are used to measure the time difference, see Figure 6.27. The starting point of the light response is extracted from the signal-shapes of each SiPM , recorded by a FADC-module, see Figure 6.8. The method for determining the starting point is described in Reference [50].

With the known refractive index $n_{BC400} = 1.58$ [32], which determines the propagation time of light in the scintillator, the least achievable spatial resolution due to the available readout electronic can be estimated:

$$x_{\text{spat.res.}} = t \cdot \frac{c}{n_{BC400}} \approx 0.5 \text{ ns} \cdot \frac{c}{1.58} \approx 10 \text{ cm} \tag{6.6}$$

Since the prototype detector is 30 cm wide in the x-direction, see Section 6.1, and the estimated spatial resolution due to the readout electronics is about 10 cm, measurements were performed at three different detector positions with reference to the beam position. These positions are located at the left edge (**Pos 1**), in the center (**Pos 0**) and at the right edge of the detector (**Pos 2**), as indicated in Figure 6.27. The accuracy to determine the starting point depends on the detected amount of light. As described in the subsection 6.5.3, the mean detected light yield is in the order of 5 photons per event. For a sufficient accuracy for the time measurement only events with at least four photons are

used. The zero position of the time measurements is defined to be at the center position **b** of the scintillator. The position of crossing particles is calculated by the time difference between opposite sides of the detector:

$$x_{pos} \ = \ \frac{1}{2} \ \cdot \ (t_l - t_r) \ \cdot \ \frac{c}{n_{BC400}} \tag{6.7}$$

In Figure 6.28 determined positions x_{pos} are presented for three measurements **Pos 1**, **Pos 0** and **Pos 2** calculated with 6.7 from the measured time differences. The mean value and the standard deviation are presented in Table 6.2.
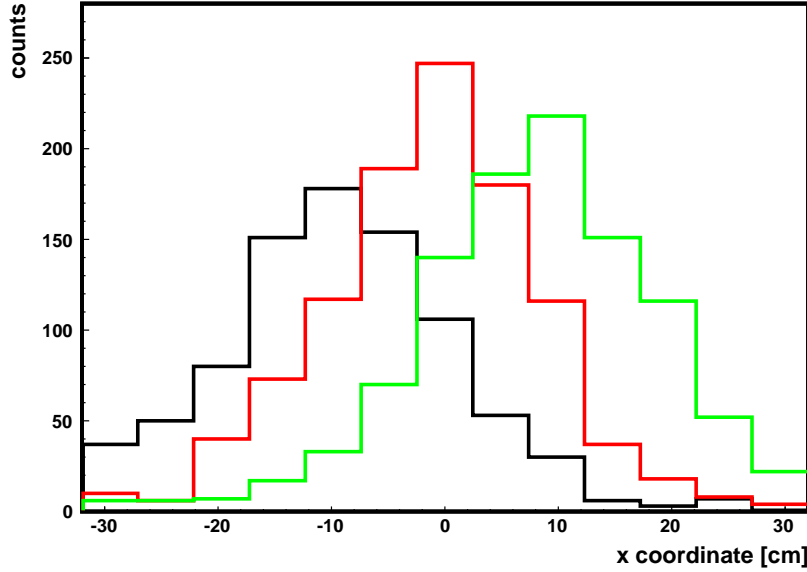
Figure 6.28: The determined positions from the calculated time differences for measurements **Pos 1**, **Pos 0** and **Pos 2** are presented. The mean values of the positions vary in agreement with the location of traversing pions. Figure taken from Reference [50].

Δx	expected value [cm]	mean value [cm]	$\pm \, \sigma$ [cm]
Pos 1	12	8.5	10
Pos 0	0	-1.0	9.2
Pos 2	-11	-9.5	9.9

Table 6.2: For three measurement **Pos 1**, **Pos 0** and **Pos 2**, the expected value, the mean values and the standard deviation are extracted from Figure 6.28.The position sensitivity is observable and the expected positions correspond well to the measured positions, whereby the spatial resolution is limited by the readout electronics and the distribution of light in the scintillator. Results taken from Reference [50].

The mean values of the distribution in Figure 6.28 vary in agreement with the position of the particle beam, The measured position difference between **Pos 1**, **Pos 0** and **Pos 2** is in agreement with the expected positions, see Figure 6.27.

The detection efficiency for all three measurements is on the order of 15 %. This is significant lower than for the position sensitivity in the y-direction, because of the requirement of at least four photons to determine the start of the SiPM signal properly.

For this measurement the limitations of the spatial resolution arise due to the limited time resolution of the readout electronics and the small amount of detected light per event. In general, the small light

collection area of the WLS-fiber in combination with the distribution of the scintillation light in the trapezoid limits the position sensitivity due to the propagation time of light.

The spatial resolution due to the propagation time of light is further investigated with a new prototype detector and a more precise readout electronic with a localized proton beam. The experimental setup and the complete results can be found in reference [35]. To conclude the results of this experiment, a position sensitivity is again observable with a spatial resolution of again 10 cm.

6.6 Measurement with Cosmic Muons

After the first measurements, performed at CERN, the detector was tested again with cosmic muons. This measurement is motivated by two goals:

- To demonstrate that the results obtained with 120 GeV pion beam at CERN are comparable with results of measurements with cosmic muons.

- to perform a reference measurement for comparison of further prototypes which are also tested with cosmic muons.

6.6.1 Experimental Setup for the Cosmic Muon Measurement
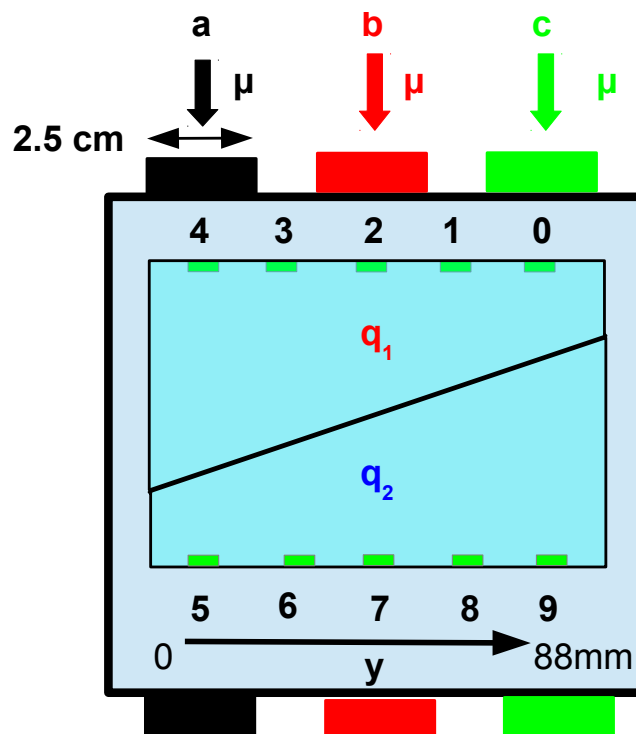
Figure 6.29: Cross section of aluminum box: POSSuMUS is tested with cosmic muons. In **a**, **b** and **c**, three successive measurement positions are indicated for testing the geometry based position sensitivity. The detector is unchanged, from the CERN measurement.

The experimental setup for the measurement with cosmic muons is described in the following section. The aluminum box with the prototype detector was mounted in an air-conditioned laboratory and equipped with the same voltage supplies as for the CERN measurements, see Section 6.4.1. The detector was unchanged, meaning that the aluminum box was not opened after the experiments at CERN.

The data acquisition system was modified. Instead of a FADC-module [71] to record the whole signal shape, a QDC-module [73] was used to measure the light response of all ten SiPMs. A schematic and a description of this data acquisition system is presented in Figure A.4 in Appendix A.2.

The coincidence trigger of cosmic muons is formed by pairs of trigger scintillators, described in Section 6.2. The trigger scintillators are located on top and below of the light tight box, as indicated by the colored rectangles in Figure 6.29. The width of the trigger scintillator is 25 mm along the position sensitive y-coordinate. For this measurement the trigger scintillators form a coincidence area of $(250 \text{ mm})^2$ with an event rate of 0.03 Hz. Therefore, the measurement time increases from 20 min. at CERN to about 55.5 h to record 6000 events for one trigger position in the laboratory. Due to the long measurement time it is essential to work in a temperature stabilized environment, to minimize gain variations of the SiPMs.

The measurements were recorded successively for three different trigger positions, indicated by **a**, **b** and **c**, see Figure 6.29. With this setup the geometry based position sensitivity of POSSuMUS was tested again. The position sensitivity due to the propagation time of light was not tested.

The gain values for all channels and different trigger positions were determined following the method described in Section 6.4.1. Since the temperature of the environment is almost constant, the gain values vary about 10 % between different channels and remain almost constant for each channel between several measurements. The corresponding plot for all gain values can be found in Figure A.5 in Appendix A.2. Here, also channel five worked with the correct bias voltage, and reveals a comparable gain value to all other channels.

6.6.2   Results of Cosmic Muon Measurement
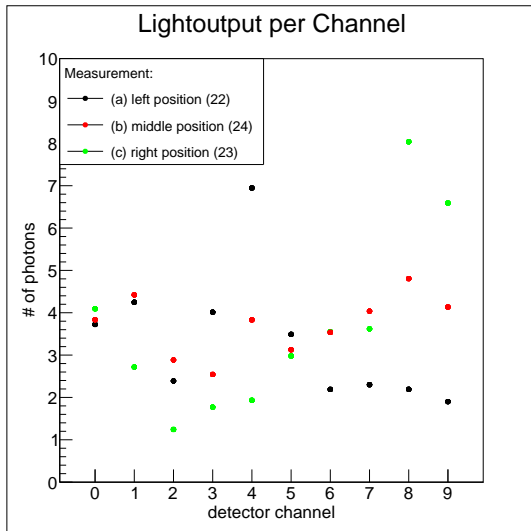
Figure 6.30: Detected amount of light for a measurement with cosmic muons: Channels at the thick side of the trapezoid show a path length dependent light output whereas the channels at the thin side show a constant light output. Channels in between reveal a transition form path length dependent to path length independent. No error bars are shown, due to the low number of detected photons.
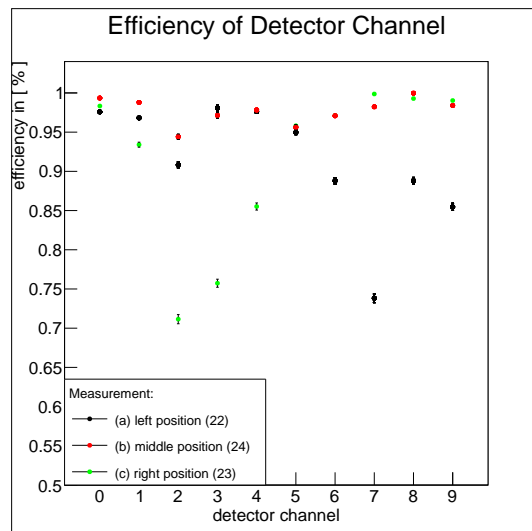
Figure 6.31: The detection efficiency for channels at the thin side of the trapezoid are above 95% for each trigger position. For channels at the thick side of the trapezoid, the detection efficiency drops significantly below 90 % when the path length in the trapezoid is short and the detected number of photons is low.

In Figure 6.30, the detected amount of light for each channel and three successive measurements **a**, **b** and **c** are shown. The number of photons is determined by the same method as described in Section

6.5.1. The results for the detected amount of light are similar to the measurements with 120 GeV pions, see Figure 6.20. The channels at the thick side of each trapezoid, namely channel four and nine reveal a comparable path length dependent light yield, whereas the channels at the thin side of the trapezoid show an almost constant light yield for different trigger positions.

In Figure 6.31 the detection efficiency is presented for all channels and three different measurements. The detection efficiency and the errors are determined as described in Section 6.5.2. At the thin side of the trapezoid the detection efficiency is above 95 % for all channels and measurements. In contrast to that, the detection efficiency decreases for channels at the thick side, when the muon crosses the trapezoid at the thin side, due to a low detected light yield. The results are comparable with the results of the pion beam measurement in Figure 6.22.

The position sensitivity of the detector for traversing particles is determined by calculating the light ratio pos(y), using Equation 2.1. Again, only channel four and nine are used in the analysis.

In Figure 6.32, the distribution of the light ratio pos(y) are displayed for the three different trigger
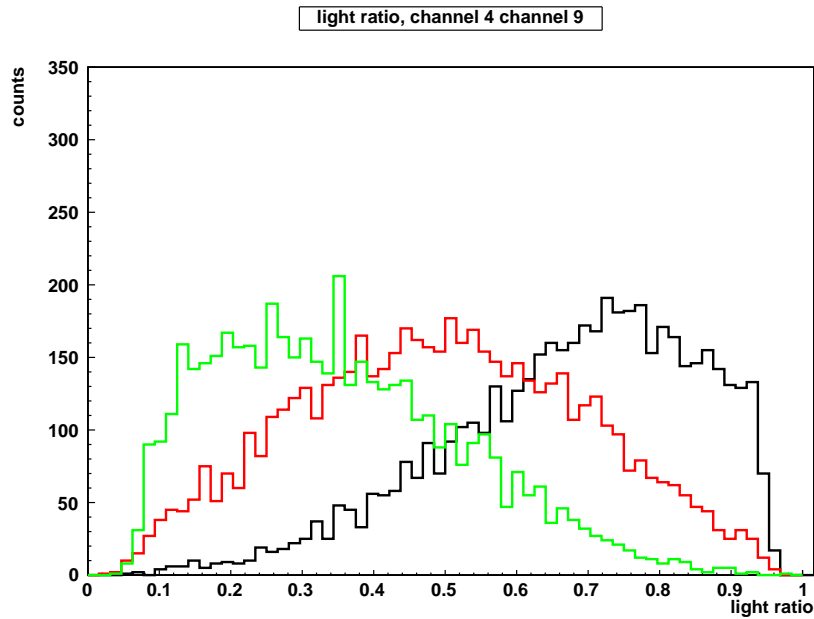
Figure 6.32: Measurements with cosmic muons: The light yield ratio evaluated for three different trigger positions different reveal three clearly separable peaks, whereby the spatial resolution is limited by the low photon statistics. The number of entries in the three distributions differs due to the degradation of efficiency at the edges of the detector.

positions. In Table 6.3, the expected position, the mean value, the standard deviations and the detection efficiencies are presented. The expected value is calculated by the path length ratio within both trapezoid, with the assumption of a linear correlation of detected amount of light and path length of

	expected value	mean value	$\pm \sigma$ error	detection efficiency
measurement **a**	0.27	0.28	0.20	83.2%
measurement **b**	0.50	0.48	0.21	94.8%
measurement **c**	0.73	0.74	0.19	80.3%

Table 6.3: For three measurement **a**, **b** and **c**, the expected value, the mean values, the standard deviation and the detection efficiencies are listed, extracted from Figure 6.32. The expected value is calculated by the path-Lent ratio within both trapezoid. The assumption is, that there is a linear correlation between path length and detected amount of light.

the muon within the scintillator.

Three separable peaks are observable, whereby the variation of the distributions is in agreement with the trigger positions and reveals the position sensitivity of the detector, see Figure 6.32. For trigger position **b**, the expected value for the light ratio pos(y) is 0.5, due to equal track path lengths in both trapezoids. The measured value is close to the expected value with a standard deviation of 0.209, which corresponds to a spatial resolution of 29.9 mm. The mean values of measurement **a** and **c** are also close to the expected value. The detection efficiency is 95 % for measurement **b** and drops to about 80 % for measurement **a** and **c**, because of the decreasing channel efficiency of channel four and nine for these measurements.

The detection efficiency for different measurements are in agreement with the results presented in Section 6.5.3. The spatial resolution is about 10 mm larger than for the measurement with 120 GeV pions. This is explainable by the trigger width of 25 mm in contrast to 10 mm for the measurement at CERN and to lesser extent by the multiple scattering in the aluminum box and scintillator due to the low momenta of cosmic muons.

6.7 Conclusion of Prototype I

The first prototype detector of the POSSuMUS concept was tested at the experimental site H6 located at the north area of CERN. The provided pion beam had an energy of 120 GeV. The detector consists of two trapezoidal shaped scintillators, equipped with five WLS-fiber per trapezoid and a single side SiPM readout per fiber. The two dimensional position sensitivity of the detector was investigated during this experiment.

In the y-coordinate the position sensitivity is achieved by the path length dependent scintillation light of pions which crossed both trapezoids. The experiment revealed a position sensitivity for the whole detector area. For three different horizontal measurement positions, the position sensitivity is presented, in Figure 6.23, in Figure 6.26 and in Figure A.3.

The spatial resolution for traversing particles is in the order of 20 mm. The detection efficiency varies between 82 % for measurements position at the edges of the detector to 97 % for the measurement position in the center of the y-coordinate. The first prototype is tested again with cosmic muons and also revealed a position sensitivity, observable in Figure 6.32.

The position sensitivity for the x-coordinate is achieved by the propagation time of light in the scintillator. The result is presented in Figure 6.28 for three different measurement positions indicated in Figure 6.27. The achieved spatial resolution is in the order of 20 cm. The detection efficiency is 15 %. The global limitation of the detector's properties arise from the low detected amount of light in each channel per pion event. The detected light yield is in the order of 5 photons per event and channel.

Further limitations for the spatial resolution in the y-direction arise from the result that a path length dependent amount of light is only observable for channels located at the thick side of the trapezoid. Moreover only one out of five channels for each trapezoid exhibit a reliable path length dependent amount of light. Therefore, the spatial resolution for the y-coordinate, determined by the light ratio of both trapezoids is mainly limited due to photon statistics.

Channels located at the thin base of the trapezoid reveal no path length dependent amount of light. Hence they are not included in the determination of the particle's position. However, those channels with a constant light output for different path length within the scintillator can be used to minimize the systematic error of the landau-like energy loss of minimal ionizing particles in the scintillator, described in Section 2.1.2. The position insensitive channels can be used to normalize the detected amount of light for position sensitive channels for each trapezoid separately. This is reasonable, when the spatial resolution is not longer dominantly limited by photon statistics.

The detection efficiency drops for position sensitive channels due to the small amount of detected scintillation light when the pion crosses the detector at the thin base of one trapezoid. Therefore the detection efficiencies decreases for measurement positions close to the edges of the detector.

The spatial resolution in the x-coordinate is mainly limited by the timing resolution of the readout electronics and due to the wide distribution of scintillation light within the trapezoid. Moreover a position sensitivity is only achievable for events with a detected amount of photons of at least 4 photons. This condition is needed to specify the starting point of the SiPM-response with a sufficient accuracy for channels involved in the determination of the particle's position. Therefore the detection efficiency drops to a low value.

For the further development and improvement of the detector's properties, the main focus is to enhance the amount of detected photons per event. Hence several steps are considered in the following:

- Optimizing the light distribution in the scintillator, by investigating several wrapping materials.

- Optimizing the light collection properties of WLS-fiber and SiPM.

- Simulation of light propagation in the scintillator to optimize the position of light collecting fibers or trapezoidal geometries.

- Improving the position sensitivity due to the propagation time of light by the use of readout electronics with better timing resolution and double sided readout of each fiber.

The second focus is to facilitate the handling with SiPMs: Therefore, one topic is important:

- Development of a gain stabilization and monitoring system to work independent from temperature changes of the environment.

Chapter 7

Studies for Improving the Light Detection

After the first test of a POSSuMUS Prototype, described in Chapter 6. The further development concentrated on the enhancement of the detected amount of light per event. By increasing the number of detected photons, the detector characteristics, like position sensitivity, spatial resolution and detection efficiency are improved.

7.1 Improving Light Detection Characteristics for Trapezoids

To improve and understand the light collecting properties of the detector and to enhance the detected amount of light, several starting points exist.

Firstly, the amount of detected light is influenced by the kind of reflection at the edges of the trapezoidal scintillator. In the first prototype a directed reflection by aluminum foil was chosen. An alternative option is diffuse reflection. Therefore, several kinds of diffuse reflecting wrapping materials are tested to investigate the variation of the detected amount of light.

Secondly, a Monte Carlo Simulation for the created scintillation light leads to an understanding of the distribution of photons within the trapezoidal scintillators.

Thirdly, the light collection properties of the WLS-Fiber in combination with a SiPM are investigated. For that purpose WLS-fibers, with a larger diameter, and SiPMs, with a larger active area, are tested in combination with a plastic scintillator. Moreover the depth of the groove, where the WLS-Fibers are glued into, are varied to find the optimal composition for collecting scintillation light.

The last point, which is investigated to enhance the detected amount of light are the coupling of SiPM and the WLS-fiber. Therefore, several materials with a comparable refractive index are inserted in between SiPM and fiber and the influence on the detected amount of light is measured.

7.1.1 Test of Different Wrapping Materials

To investigate the influence of different wrapping materials on the detected amount of light the following experimental setup was used. The setup is displayed in Figure 7.1.

A trapezoidal scintillator with the same geometry as the first prototype, see Section 6.1, was used to investigate the influence of different wrapping materials on the detected amount of light.

Two of the PMTs are located at the thick base of the trapezoid, named as Ch 0 and Ch 2. The other two PMTs reside at the thin base of the trapezoidal scintillator.

The measured scintillation light is created by cosmic muons. A coincident signal of traversing cosmic muons is realized by two trigger modules, described in section 6.2. The trigger scintillators are located on top and below the trapezoidal scintillator. For each wrapping material, three different trigger
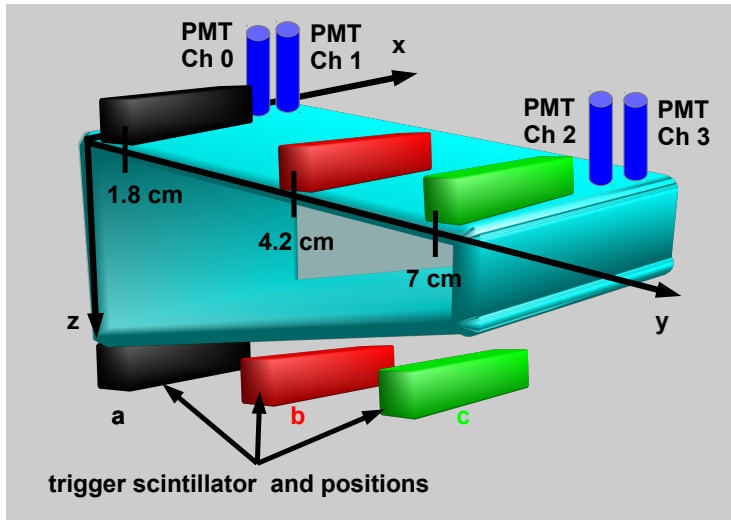
Figure 7.1: Experimental Setup for testing several wrapping materials: A trapezoidal scintillator, with the geometry described in 6.1, was equipped with 4 photomultiplier Tubes, whereby two are located at the thick side and two at the thin side of the scintillator. The detected amount was measured for three different trigger positions, indicated by **a**, **b** and **c** and tested with cosmic muons.

positions **a**, **b** and **c** were measured, to determine the detected amount of light depending on the path length within the scintillator.

The trapezoid is wrapped successively in four different wrapping materials, namely:

- one layer of aluminum foil

- one layer of BC-642 PTFE Reflector Tape [78]

- three layers of BC-642 PTFE Reflector Tape [78]

- BC-620 Reflector Paint (TiO$_2$) [55]

- one layer of Tyvek material [80]

- three Tyvek layers [80]

To minimize diffuse light from outside, in each case a final wrapping with an aluminum foil was added.

The signal response of all four PMT-tubes was recorded by using a standard VME based QDC-readout, see Appendix A.2 for a detailed description of the readout system.

To minimize the influences of the environment on the measurements, the experimental setup was located in a climate chamber [49]. Therefore the temperature and the humidity were constant over the measurement time of several days for one wrapping material and trigger position. The four photomultiplier were calibrated to work with a similar amplification factor, details about the calibration of PMT is described in [50]

In Figure 7.2 the detected amount of light for channel zero is plotted for three different trigger positions, indicated by **a**, **b** and **c** and for five different wrapping materials.

For all wrapping-materials the amount of light is decreasing with decreasing path length in the scintillator, confirming the results of the first prototype, see Figure 6.16, that channels at the thick base of the trapezoid reveal a path length dependent amount of detected photons.

Moreover the highest detected amount of light is observable for wrapping the scintillator in three layers of Tyvek material [80]. This is valid for all three trigger position **a**, **b** and **c** . Therefore, a diffuse reflection at the edges of the scintillator leads to an increased amount of detected photons.

All other diffuse reflecting wrapping materials reveal a lower detected amount of light for all trigger positions. The directed reflection, realized by the aluminum foil wrapping, exhibits the lowest detected amount of light. It is about a factor two lower than for the multi Tyvek wrapping. Since the first prototype was wrapped in one layer of aluminum foil, a multi Tyvek wrapping can lead to a significant higher detected amount of light per event.
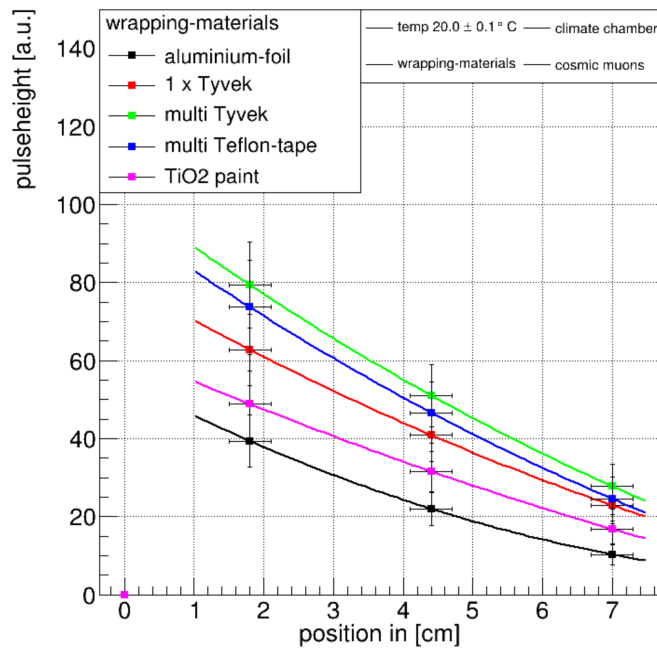
Figure 7.2: Detected amount of light for three different trigger positions, for five wrapping material. The highest detected amount of light is measured for the multi layer wrapping of Tyvek (3 layers) with the trigger position at the thick edge of the trapezoid. For the other material the detected amount of light is lower, for all measurements points. Figure taken from [50].
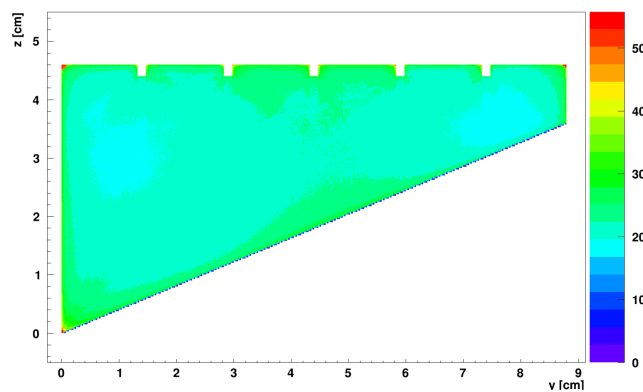
Figure 7.3: The photon distribution in a trapezoidal scintillator is presented, simulated by the described Monte Carlo simulation. The geometry of the trapezoid and the position of the grooves correspond to the design of the first prototype presented in chapter 6. Figure taken from [50].

7.1.2   Simulation of Light Propagation in a Plastic Scintillator

A second approach for understanding and improving the light propagation in the scintillator was a self-developed Monte Carlo Simulation. The simulation focuses on the creation of scintillation light and on the propagation of photons within the scintillator. This simulation does not describe the light collection of WLS-fibers and the guiding of photons towards the SiPM. Further details about the simulation are presented in Reference [50].

In Figure 7.3 the photon distribution in a trapezoidal scintillator is presented, simulated by the Monte Carlo simulation, for incoming muons. The geometry of the trapezoid and the position of the grooves correspond to the design of the first prototype presented in chapter 6. The simulation can be used to describe the result of the wrapping study properly.

The simulation showed a mxaimum of light in the corners of the trapezoid in particular the rectangular corner at the thick side, see Figure 7.3.

7.1.3   Comparison of Measurement and Simulation
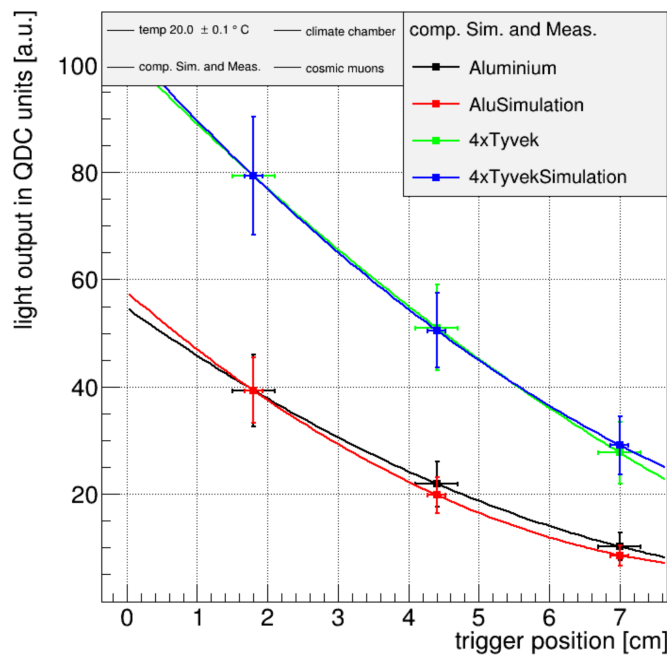
Figure 7.4: Comparison of simulated and measured amount of detected light: For the detected amount of light for a scintillator wrapping with Tyvek and aluminum foil, the measured data are presented with the simulated data. For both cases, measurement and simulation are in agreement. Figure taken from [50].

In Figure 7.4 the measurements for the aluminum wrapping and the multi Tyvek wrapping are presented in combination with the results of the Monte Carlo simulation, described in section 7.1.2.

The simulated amount of detected light is in agreement with the measured amount of light for different trigger positions and wrapping materials.

The reliability of the simulation is shown by the comparison of simulated and measured results. The simulation can be used for studies about an optimized detector geometry or an optimized position of light collecting fibers for further prototypes of the POSSuMUS detector.
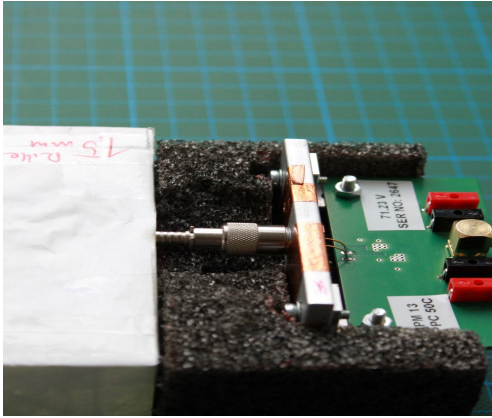
Figure 7.5: Optimizing the detected amount of light by using WLS-fibers with a larger diameter of 1.5 mm in combination with a SiPM with an active area of 3×3 mm. Moreover, the length of the WLS-system is minimized to the smallest possible length. In addition a bending radius of the fiber is avoided.
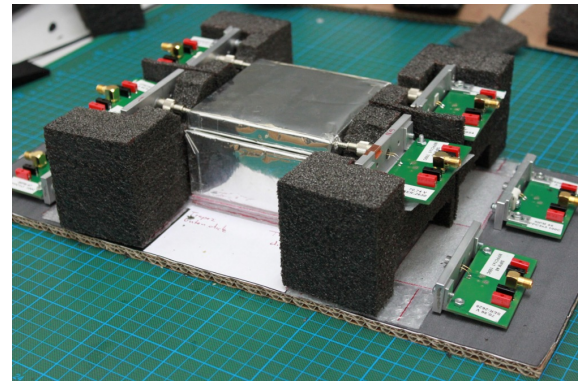
Figure 7.6: A double sided readout of each fiber leads to a factor 2 higher amount of detected light.

7.1.4 Optimizing the Light Detection of WLS-Fiber and SiPM

One starting point to enhance the amount of detected light of a plastic scintillator combined with a WLS-fibers and SiPMs is to increase the sensitive area of the WLS-fiber. Therefore, fibers with a diameter of 1.5 mm, instead of 1.0 mm are used.

To take full effect of the larger light collecting surface of the fiber also SiPMs are used with a larger active area, to ensure the detection of all collected photons of the WLS-fiber.

Moreover, the length of the WLS-fiber is minimized to reduce the loss of absorbed photons on their way to the SiPM, indicated in Figure 7.5. By this setup, also a bending radius is avoided, which can also reduce the amount of detected light.

The third step to enhance the amount of detected light is to realized by a double sided readout of the fiber, as visible in Figure 7.6. This will bring an additional factor 2 for the amount of detected light per event.

7.1.5 Improving the Light Collection of the WLS-Fiber

An additional starting point to enhance the detected amount of light per event is, to vary the depth of the groove, where the WLS fiber is glued into.

In Figure 7.7 the experimental setup for the investigation of different groove depths is presented. A light tight aluminum box is equipped with a Peltier cooling system to keep the temperature within the box at a constant value of 20°C. Since, the gain stabilization system, described in Section 4.2.3, was not ready for operation. The effort of cooling the light tight box is necessary, to work at the same gain value of the SiPM for different measurements. In Figure A.6, see Appendix A, the reproducibility of the Peltier cooling is shown.

To measure with a high rate and a constant light output, we used a pulsed UV-LED to inject light into the scintillator. The LED was connected to an Arbitrary Function Generator (AFG) [79], where the pulse widths, the lengths and frequency of the light pulse can be adjusted.

The amount of emitted light is chosen, such that a Gaussian response of the SiPM is observable, but the SiPM is not saturated. The response of the SiPM is shown in Figure 7.8.

In the light tight box a cuboid plastic scintillator with a groove is mounted. A WLS-fiber is inserted in the groove and a SiPM is connected at one end of the fiber. The bias voltage U_{bias} is adjusted
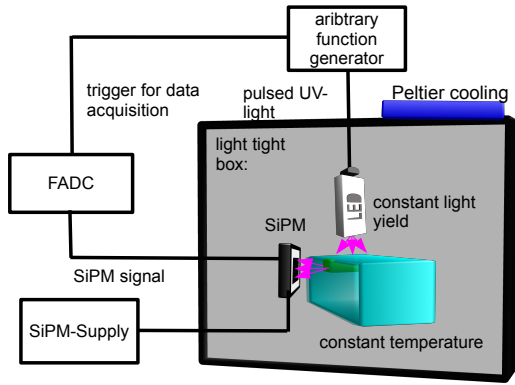
Figure 7.7: Experimental Setup for the measurement of the detected amount of light for scintillator with groove depths. The scintillator cuboids are equipped with grooves from 1.5 mm to 3.5 mm.
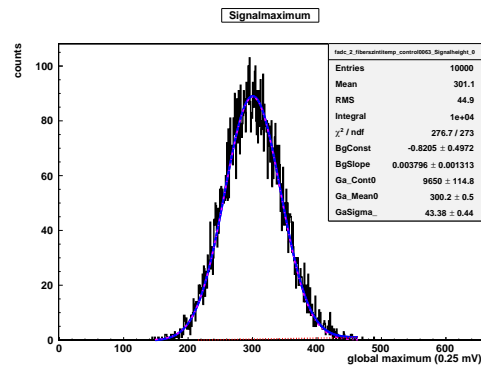
Figure 7.8: Light Response of a SiPM, that is connected to WLS-Fiber located in a groove within a scintillator.

automatically by an EA-power-supply [31] for the range of the over voltage from 0 to 1.8 V. The data acquisition system is a VME-based FADC-readout, described in Appendix A.

For each over-voltage U_{over} the detected amount of light is determined by extracting the mean value and standard deviation for further analysis.

These measurements are repeated for different scintillator cuboids with different groove depths, indicated in Figure 7.9. The groove depth range from no groove, here the fiber is located on the cuboid's surface , to a groove depth of 3.5 mm. The width of each groove is 1.7 mm.
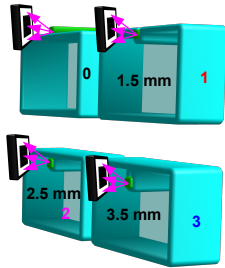
Figure 7.9: Four different scintillator with different groove depth are equipped with the same WLS-Fiber and SiPM. For comparability the Fiber was only air coupled to the scintillator and no glue was used.
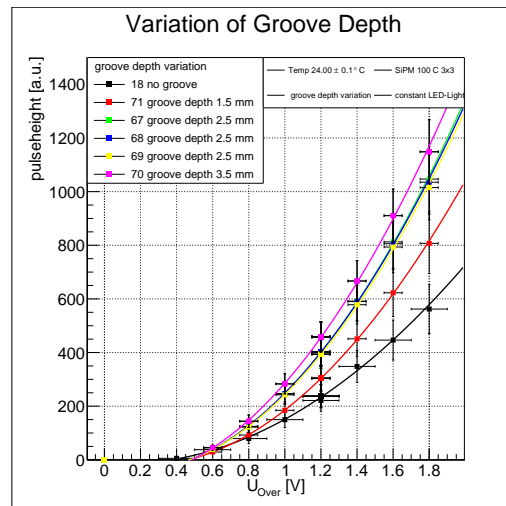
Figure 7.10: Result for testing cuboid scintillators with different groove depth. For increasing the groove depth the detected amount of light increases about a factor 1.4 from 1.5 mm groove (CERN-setup) to 3.5 mm groove depth.

In Figure 7.10 the result of the amount of detected light is presented for different groove depths. The mean values for each over voltage U_{over} are plotted for different groove depth. The mean values for each groove depth are fitted by polynomial of second degree and indicated by different colors.

The lowest amount of detected light is observable for the scintillator with no groove, measurement **1**,

where the fiber is just put on top of the scintillator. Here the light collecting area for the WLS fiber is small, hence the amount of detected light is small.

For all other scintillators with deeper groove depth the amount of detected light increases with increasing groove depth for all applied voltages.

Since all measurements were recorded at the same temperature and at the same over voltages U_{over}, the signal height of the SiPM is comparable for different scintillators. The reproducibility of the measurements is shown, by the measurements of **3**, **4**, **5**, which were recorded on different days and after several changes of the experimental setup.

The measurement **6** corresponding to a groove depth of 3.5 mm reveals a factor two higher light output than measurement **1**, where no groove is present.

The comparison of measurement **2** with a groove depth of 1.5 mm, which corresponds to the setup of the CERN prototype, and the measurement **6** with a groove depth of 3.5 mm propose a 1.4 higher amount of detected light.

7.1.6 Optimizing Coupling between Fiber and SiPM
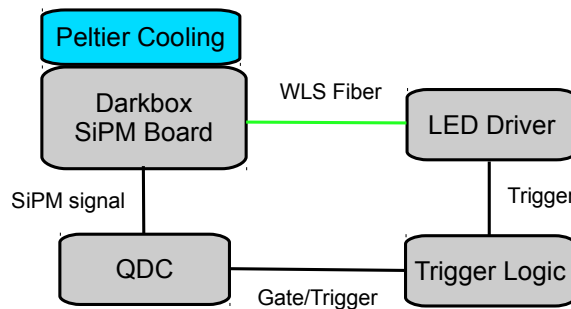
Figure 7.11: Experimental setup for the investigation of different coupling materials with an external LED. The SiPM device is mounted in a temperature controlled light tight box. From a LED [68] light pulses are sent to the sensitive area of the SiPM by using WLS-fiber [34]. The data acquisition system is a standard VME-based QDC-readout. Several coupling material, like silicon pads or optical grease are inserted between Fiber and SiPM and the amount of detected light is measured.

The last point to be investigated for a higher detected amount of photons is the coupling between WLS-fiber and SiPM. For that purpose either optical grease [30] or silicon pads [54] were inserted in between the fiber end and the SiPM. Both materials have the same refractive index as the fiber material. An other starting point is the use of different polishing techniques (higher or lower granularity) at both fiber ends.

This is tested with the following experimental setup. The SiPM is mounted in a temperature controlled box and is connected to a WLS Fiber, via FC coupling. The LED [68] is connected on the other end of the WLS-fiber and sends light pulses to create a Gaussian response at the SiPM (medium photon number, no saturation of the SiPM). The settings at the LED Driver are constant for the whole set of measurements.

The signal response of the SiPM is recorded by a QDC-readout, which was described earlier. To investigate the influence of the coupling material on the amount of detected light, silicon pads of different thickness or optical grease is inserted in between the fiber end and the SiPM. Since the SiPM works in a temperature stabilized environment, the gain value is equal for different measurements. In Figure 7.12 the mean number of photons is presented for different measurement with silicon pads of different thickness. There is no significant increase observable for the amount of detected light is in

comparison to the measurement without any additional material.

  The measurements were repeated for coupling with optical grease or different polishing techniques
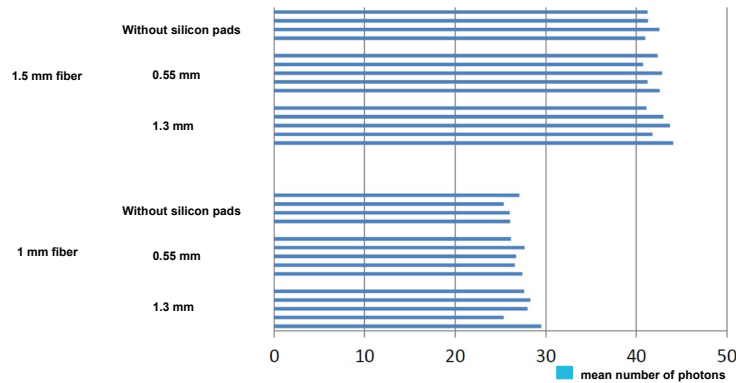
Figure 7.12: Detected amount of light for different silicon pads inserted in between WLS fiber and SiPM. No significant increase of detected photons is observable. Figure taken from Reference [6]

of the fiber end. The corresponding Figure can be found in Reference [6]. There is also no significant increase in the amount of detected light observable, for any kind of coupling.

7.1.7   Summary for different presented Studies

The change from a direct reflecting material to a diffuse reflecting material leads to a factor 2 higher detected amount of light.

The use of WLS-fibers with a larger diameter of 1.5 mm in combination with SiPMs with a larger sensitive area, the minimization of the length of WLS-fiber and the avoidance of a bending radius lead to an expected enhancement of the amount of detected light of about 1.5. A double sided readout of each fiber results in a factor 2 higher amount of detected light.

The use of scintillators with a groove depth of 3.5 mm, in contrast to 1.5 mm of the first prototype, lead to an enhanced factor 1.4 amount of detected light.

The use of coupling materials in between the SiPM and the fiber, showed no significant increase in the amount of detected light.

In total an increased light output of about 4.2 is expected for each SiPM channel in comparison to the first prototype.

Thus, using a double sided readout for a second prototype of the POSSuMUS detector, presented in the following Chapter, an enhanced amount of light of a factor 8.4 is expected.

Chapter 8

Second POSSuMUS Prototype

After studies to enhance the amount of detected light per event for the combination of a plastic scintillator with WLS-fibers and SiPM-readout, described in Chapter 7, a new prototype was built and its characteristics investigated. For this investigation no particle beams with high energetic muons or pions were available at CERN, because of long shutdown 1 (LS1), see Figure 1.4. Therefore, this prototype was tested exclusively with cosmic muons in the laboratory.

8.1 Design and Equipment of the Second Prototype

8.1.1 Detector Design of the Second Prototype
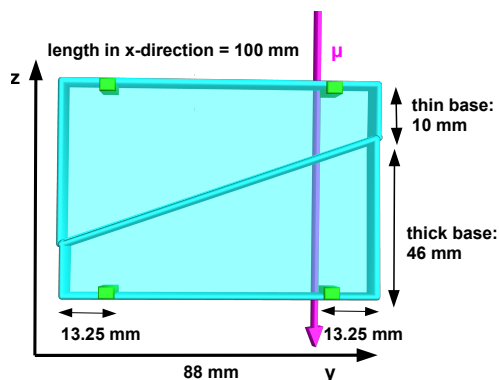
Figure 8.1: Design of the second POSSuMUS prototype: Each trapezoid is equipped with two WLS-fibers along the position sensitive coordinate, located 13.25 mm away from the edges of the trapezoid. The trapezoidal geometry is the same as described in Section 6.1.
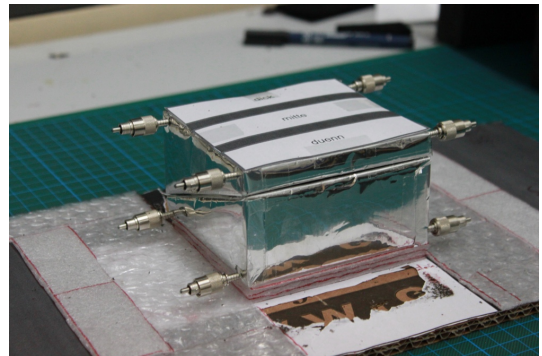
Figure 8.2: Second prototype detector: Both trapezoids are wrapped in three layers of diffuse reflecting Tyvek-material. To insulate the trapezoids optically from each other, the trapezoids are wrapped in a fourth layer of aluminum foil. At both ends of each fiber two FC-plugs are glued, allowing for a double sided readout.

The second prototype detector is built from trapezoidal scintillators, which are of similar proportions as those used in the first prototype detector, except for the length in the x-direction, which is only 100 mm. The position sensitive y-direction has a length of 88 mm. The thin base of the trapezoid is 10 mm and the thick base 46 mm high. The position sensitivity along the x-direction, due to the propagation time of light was tested again in an other experiment, where the setup and results are described in reference [35].

In contrast to the first prototype, the detector was wrapped in three layers of diffuse reflecting Tyvek-material [80] and one layer of aluminum foil to optically insulate the trapezoids from each other. The diffuse reflecting material is chosen, due to a factor 2 higher amount of detected light in comparison

to the directed reflection, presented in Section 7.1.1.

Each scintillator is equipped with two WLS-fibers of 1.5 mm in diameter. The fibers are glued in grooves with a width of 1.7 mm and a depth of 3.5 mm. Each fiber is located 13.25 mm away from the edges of the scintillators. The WLS-fibers of larger diameter are chosen because of an increased sensitive area (factor 1.5), the groove depth is chosen because of the results of Section 7.1.5. All details of the detector are presented in Figure 8.1. The fiber positions at the thick and at the thin base of the trapezoid are identical to those used in the first prototype. The motivation for these fiber position and the reduction of the number of fibers from five to two per trapezoid are the results for the amount of detected light for the first prototype, see Section 6.5. The fibers at the thick side revealed a path length dependent amount of detected light and the fibers at the thin side showed an almost constant light yield to be used for normalization. The other installed fibers in the first prototype showed no clear path length dependent light output and are omitted to reduce the number of readout channels.

The constant amount of detected light for the fiber at the thin side is foreseen to correct the systematic impact for the landau like energy loss of cosmic muons in the scintillator, described in Section 2.1.2. Each fiber end was equipped with two FC-plugs for a double sided readout of each fiber and therefore a factor two increased amount of detected photons per event. In total, the second POSSuMUS prototype has eight readout channels, to determine the path-length-dependent amount of light, see Figure 8.2.

8.1.2 Equipment of the Second Prototype
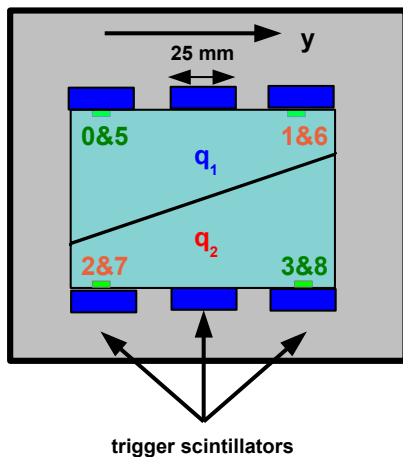
Figure 8.3: The second prototype detector is shown from one readout side, mounted in a light tight box: The double sided readout is indicated by two channel numbers at each fiber. Six trigger scintillators are positioned on top and below the detector. The edges of the trigger scintillator are aligned with the edges of the detector.
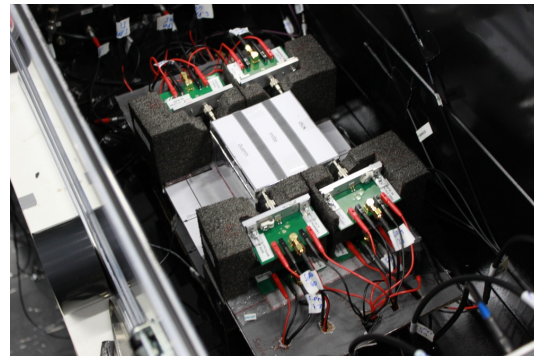
Figure 8.4: The second prototype of the POSSuMUS-detector is equipped with 8 SiPMs for a double sided readout. FC-coupling are visible in silver. The FC-plugs are connected to FC-connectors, which are mounted to the circuit board, where the SiPM is soldered.

The second prototype is equipped with eight Hamamatsu SiPMs [37], located at each fiber end, with a photon sensitive area of 9 mm^2. They are coupled via a FC-Socket to the FC-plug of the detector, see Figure 8.4. The SiPMs are soldered to the circuit board, which is described in detail in Section 5.3.

The SiPM supply voltage of 5 V for the pre-amplifier BGA614 [39], located on each circuit board is provided by the TL 200 power supply [1]. The global bias voltage is provided by a Keithley 2400

source meter [44]. The source meter is connected to the remotely adjustable voltage divider described in Section 4.2.2. Thus, it is possible to adjust the voltages U_{over} at all SiPMs separately and automatically to work with similar gain values at all channels. Moreover this voltage divider is capable to vary separately the voltage U_{Bias} for each channel according to temperature changes of the environment. Hence, the SiPMs can work with constant gain values for the whole measurement time of one week or longer.

To correct the applied voltages for temperatures changes, two sensors located at each readout side of the detector monitor the temperature. The measured temperature profile for one sensor is presented in Figure 8.5. Here the day/night cycles of the temperature are observable. The maximum temperature variation is in the order of 4 °C for this measurement time of one week. The applied voltages U_{Bias} are corrected by the calibration factor for the used SiPMs of 60.8 mV/°K, see details for the determination of the calibration factor in Section 4.4. Details about the gain value profile can be found in the following section.
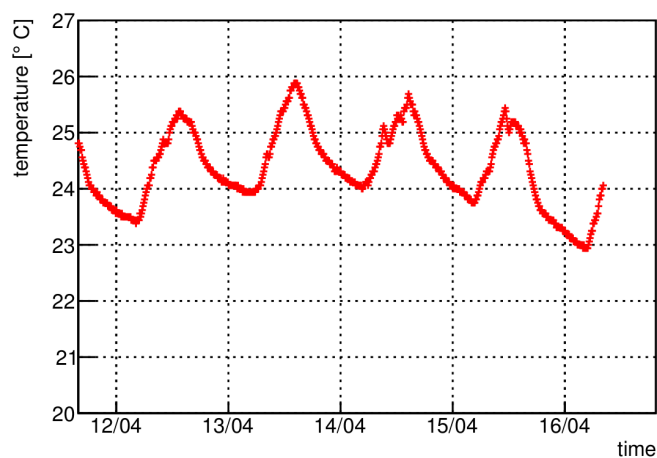
Figure 8.5: Temperature profile for the measurement presented in the section 8.2.2: The temperature variation for the period of on week for one measurement with the POSSuMUS detector. The temperature dependent gain value of SiPMs is kept constant by adjusting the correct over voltage, by using the remotely controllable voltage divider described in Section 4.2.2

.

The POSSuMUS detector is mounted in a light tight box, which is equipped with clutches to provide voltages for all devices in the box. In total six trigger scintillators are used for triggering on cosmic muons. Each of the trigger detectors consists of (100 mm × 25 mm × 10 mm) (Length × Width × Height) plastic-scintillator cuboid, which are glued to a photomultiplier tube [38]. Three trigger modules are located on top of the detector aligned with the three trigger modules installed below the detector. The left and right trigger scintillators are aligned to the edge of detector. All details are presented in Figure 8.3.

8.2   Data Acquisition System

For the second prototype the data acquisition system is supposed to serve two purposes:

- The first task is the recording of the light responses of all eight SiPM-channels for each muon crossing the detector.

- The second task for the system is to check, that the similar gain values are adjusted at each SiPM and to monitor them for the whole measurement period.

8.2.1 Readout of Signal Height and Timing Information
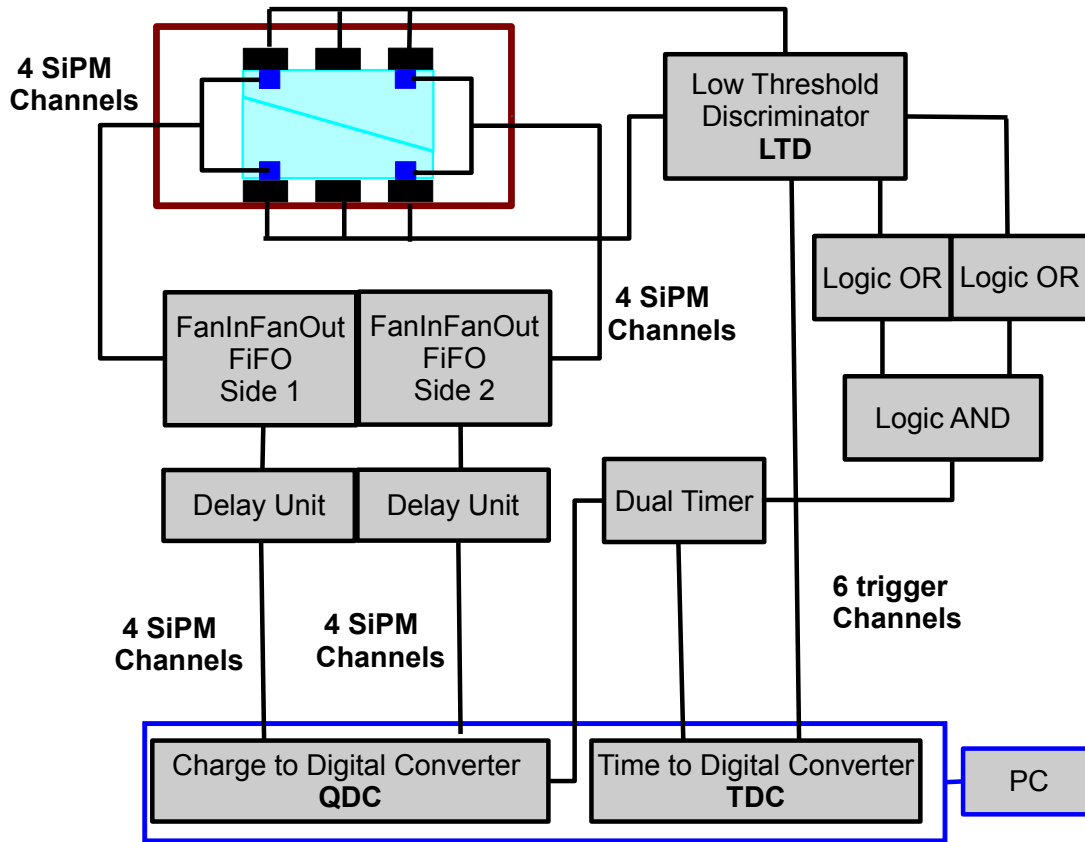
Figure 8.6: Data acquisition system for the second prototype of the POSSuMUS detector: The first task of the data acquisition is to measure the SIPM-signals of all readout channels and and to identify the involved trigger scintillators, to discriminate between vertical and inclined tracks. Therefore a combined QDC-TDC-readout system used.

To record the SiPM-responses and trigger signals a combined QDC-TDC data acquisition system is used, based on a VME readout [77]. The data acquisition system is displayed in Figure 8.6.

All eight SIPM-signals of the detector are given to two Linear Fan in Fan Out (FIFO)-modules [67], each provides four input channels. For each FIFO input channel four output channels of the copied input signal are provided.

One output for each channel is given to a delay unit [66] to shift the signal to the correct position in time for the acquisition window. The signal is then given to the charge-to-digital converter (QDC) [73]. Each signal of the trigger modules is given to one channel of a Low Threshold Discriminator (LTD) module [69]. One discriminator output per channel is given to the TDC module [72] to identify which pair of trigger modules created the coincident signal. Hence, it is possible to discriminate between vertical and inclined tracks of crossing muons.

The discriminator output of the trigger scintillators on the top of the setup are logically ORed, as is also done with the trigger scintillators at the bottom. The output signals of both OR units are provided to an AND logic unit to create a trigger signal, which in turns is given to a dual timer unit [70]. The latter is used to create a trigger signal for the TDC and to create an acquisition window of adjustable width (here 45 ns) for the QDC. By using the mentioned delay units, the rising edge of each SiPM-signal is shifted to a positions 15 ns after the start of the acquisition window, to optimally integrate over the charge signal of each SiPM signal.

8.2.2 Gain Monitoring System
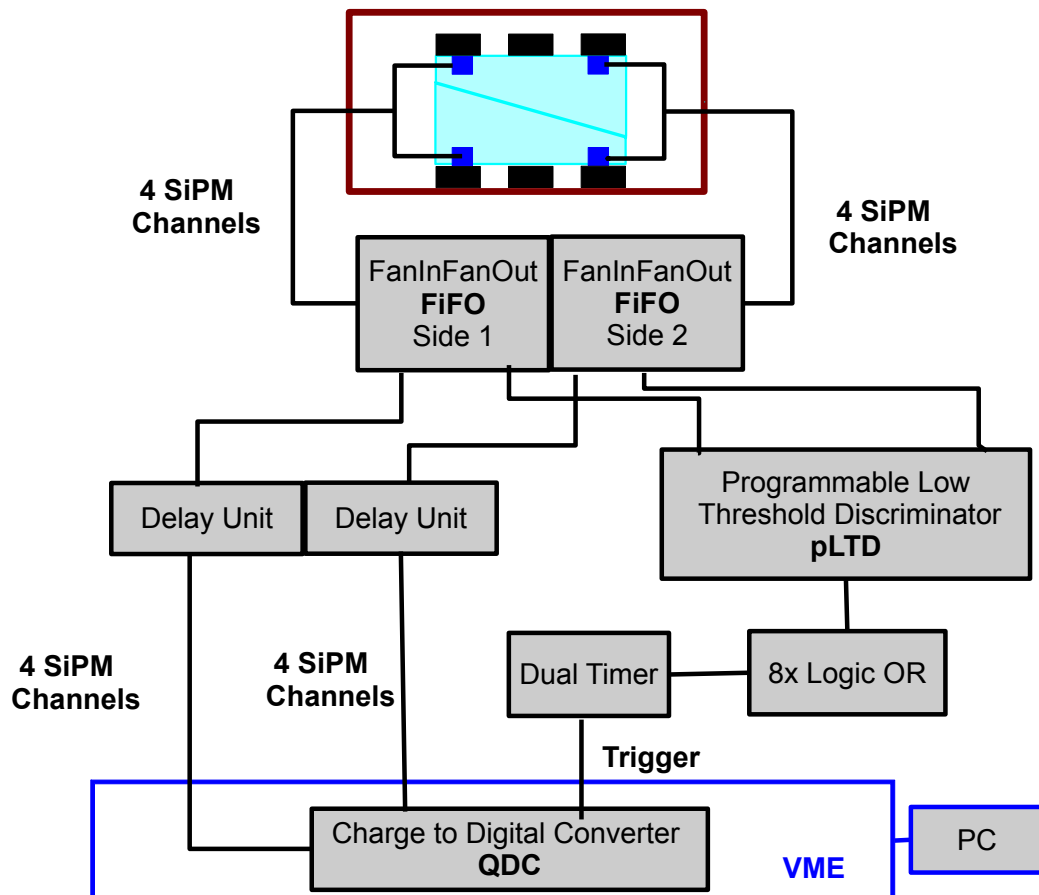
Figure 8.7: Gain monitoring for the second Prototype: To adjust the same gain value at all SiPM-channels and monitor this value over the whole measurement time a second trigger logic is integrated into the data acquisition detailed in Figure 8.6 to trigger on SiPM dark rate events.

As described in Section 8.1.2 the SiPMs of the second prototype work with an automatic voltage adjustment to compensate for temperature changes of the environment. This gain stabilization is needed because of the long measurement time with cosmic muons and gain variations due to temperature changes.

As an example, the variations in the temperature profile shown in Figure 8.5, which corresponds to a measurement time of one week, would lead to a gain variation of 35 % .

To adjust the same gain values at all SiPMs and to monitor the gain value over the whole measurement period a gain monitoring system is installed. For that purpose the same VME-data acquisition system, described in Figure 8.6 is used.

To determine the gain values of each SiPM dark rate events are used, see Section 3.3. To trigger on those events, independently from muon events, a second trigger logic is integrated, see Figure 8.7.

Therefore, one output of each FIFO channel is given to one input channel of a programmable Low Threshold discriminator (pLTD), [74]. The discriminator output of the pLTD is given to a $8 \times$ OR logic unit and finally to a second dual timer, which creates for each dark rate event a acquisition window of 45 ns for the QDC-module [73].

By using the programmable pLTD it is possible to create a trigger signal for one specific channel. This channel is under investigation, while all other channels are disabled and record the corresponding
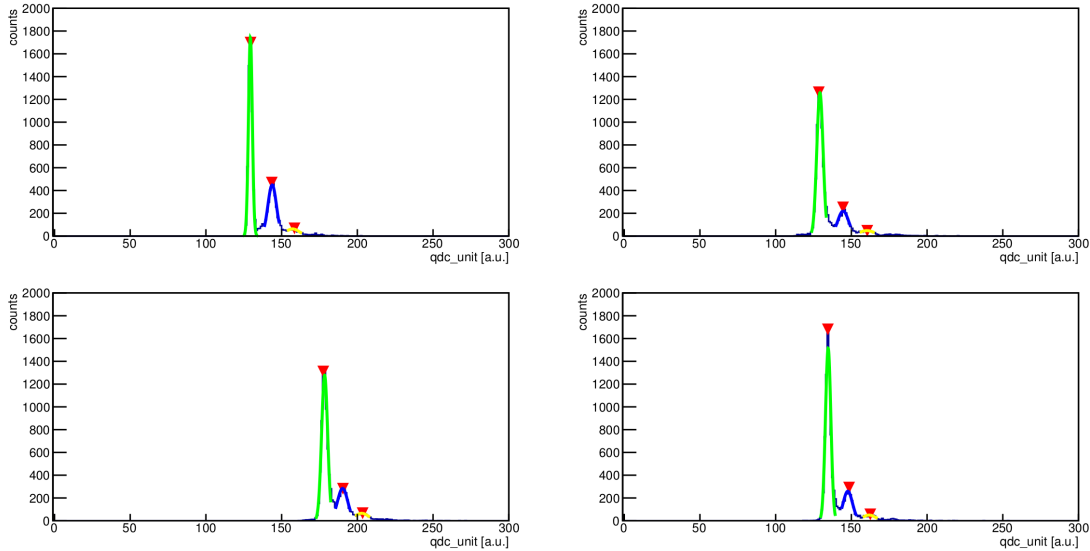
Figure 8.8: Recorded dark rate spectra for SiPMs mounted on one readout side of the second prototype detector: The threshold for the discriminator is set slightly below the first photon peak of the SiPM. Therefore, it is possible to determine the gain by using the first, second, and third pixel peak and the pedestal peak, using the method described in Section 6.4.1.
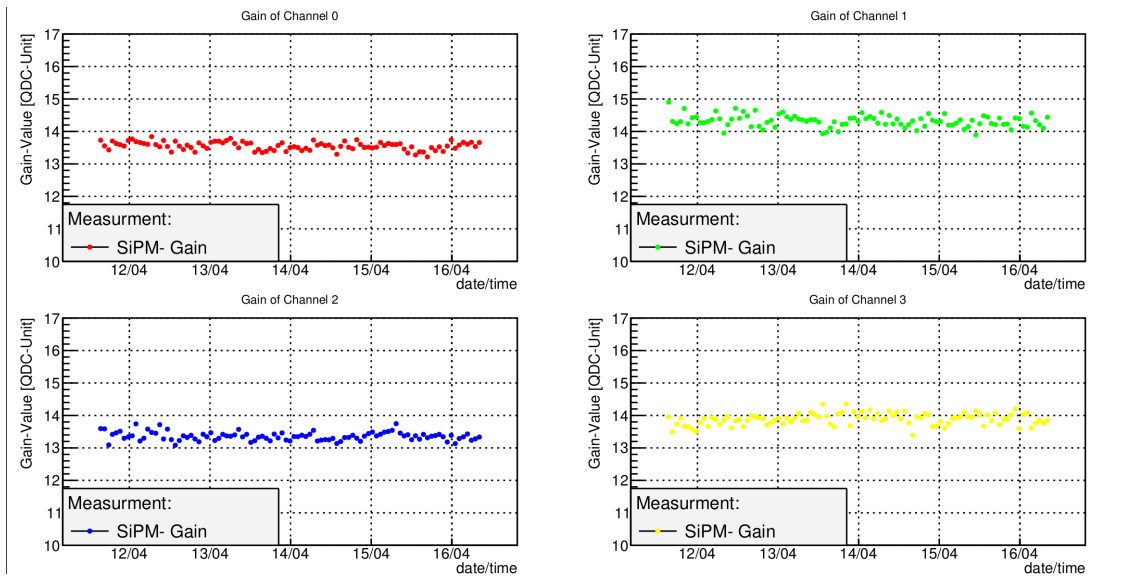
Figure 8.9: Gain values for each channel recorded over the whole measurement period of one week: The temperature variations during the measurement are shown in Figure 8.5. Due to the voltage adjustment by the remotely controllable voltage divider the gain values of all SiPM channels remain stable for the whole measurement period with an accuracy of 5 %.

QDC-pedestal. The discriminator threshold for each channel is set to a value exactly below the first photon peak.

In Figure 8.8, the dark rate spectra of four SiPM channels are shown, located at one readout side of POSSuMUS. For each SiPM, three peaks are observable which corresponds to the number of fired pixels. The gain value is determined, by using the actual pedestal peak and the first, second, and third photon peak, with the method described in Section 6.4.1. The number of entries for the several peaks vary because of different rates for the number of firing pixel. They decrease by one order of magnitude from one pixel to more pixels.

The time to record all eight dark rate spectra is about 30 seconds, and is limited by the readout rate of the data acquisition system.

The gain is monitored over the whole period of the measurement, where the gain values for all channels are determined once per hour. According to the measured temperature, see Figure 8.5, the bias voltage are adjusted by the remotely controlled voltage divider.

The gain values for the whole measurement period are plotted for one readout side in Figure 8.9. Due to the voltage- adjustment by the remotely controlled voltage divider the gain values remain constant over the whole measurement period, with an accuracy of about 5 % for all eight readout channels.

8.3 Position Sensitivity for Vertical Tracks
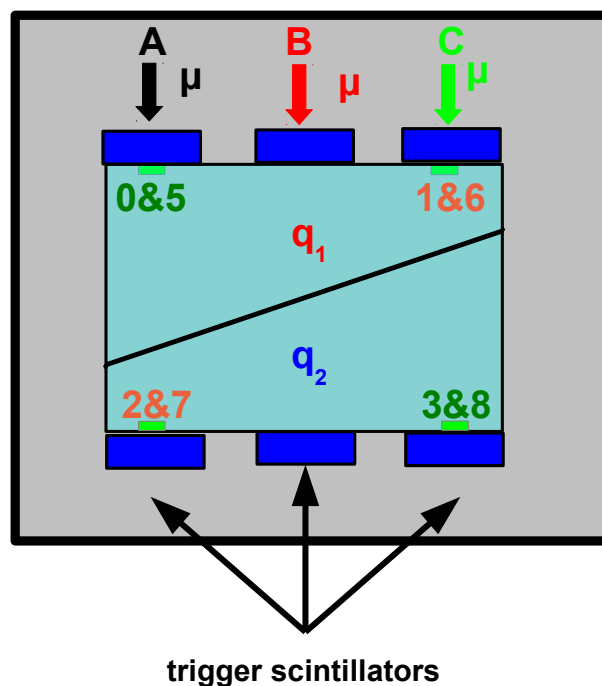
Figure 8.10: View from one readout side at the prototype detector: Three trigger combinations **a**, **b**, and **c** for vertical tracks are used to investigate the position sensitivity and the spatial resolution for muons traversing the detector.

In Figure 8.10 the detector is displayed with four readout Ch0, Ch1,Ch2,Ch3 located at one readout side. The other channels installed are at the opposite readout side. In this section only vertical trigger combinations are considered, discriminated by the 3-fold-segmented trigger scintillators. The vertical muon tracks are indicated by **a**, **b**, and **c**.

The measurement time is about a week to collect at least 10000 muons.

In Figure 8.11 the signal height spectra, recorded by 4 channels located at one readout side, are shown, separately for the three vertical trigger combination **a**, **b** and **c**. All spectra are corrected for different pedestal and gain values, which are determined as detailed in Section 8.2.2 separately for each channel.

Each of the spectra is fitted by a convoluted Landau-Gaussian-function, which is used to determine the MPV-value for further analysis, as described in Section 6.4.2.

As expected from the results of the first prototype channels, the channels located at the thin base,
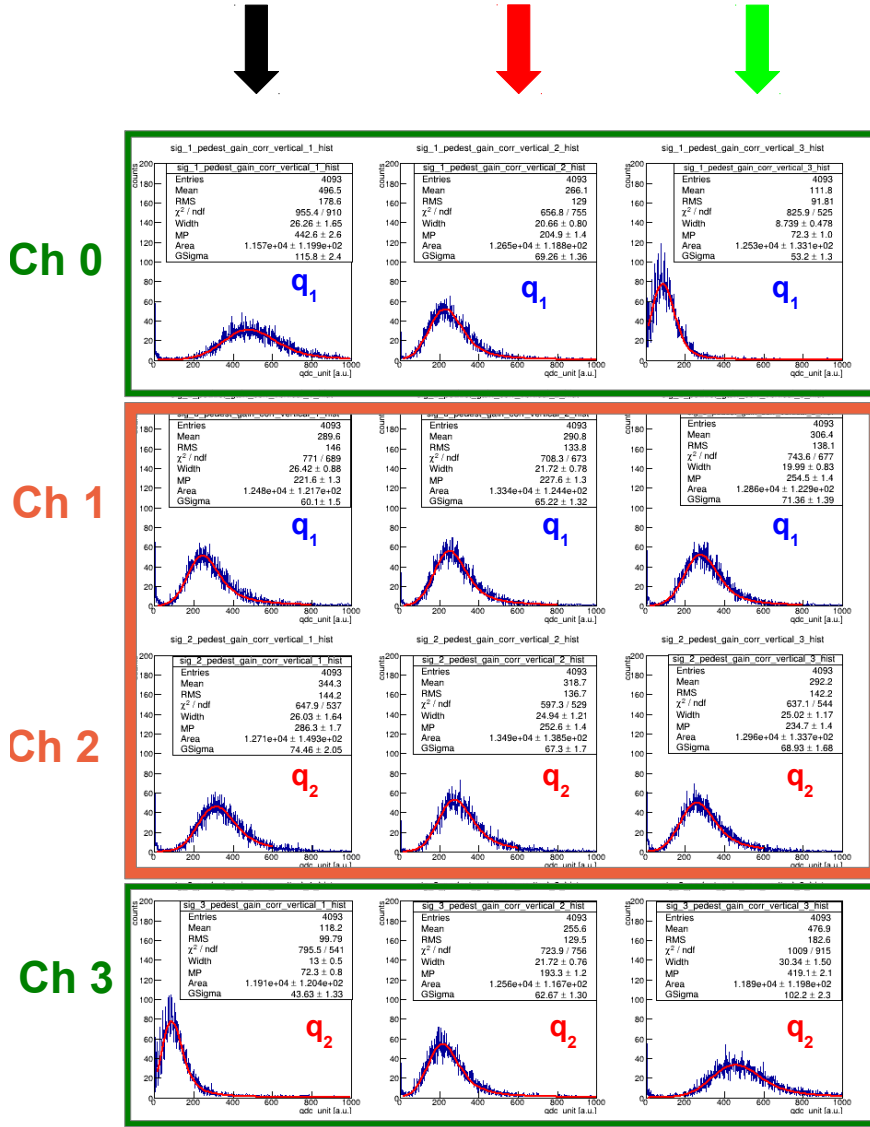
Figure 8.11: Signal height spectra for all channels of POSSuMUS for three different trigger positions **a**, **b**, and **c**: All spectra are fitted with a convoluted Landau Gaussian distribution, to determine the the MPV-value of each spectra. In the first and forth row, the path length dependent amount of detected light for channel zero in trapezoid q_1 and channel three in trapezoid q_2 is observable. In contrast, channel two in trapezoid q_1 and three in trapezoid q_2 reveal no path length dependent amount of light.

namely Ch1 in q_1 and ch2 in trapezoid q_2, reveal no path length dependent amount of detected light, see the second and third rows of Figure 8.11.

In contrast, for Ch0 in trapezoid q_1 and Ch3 in trapezoid q_2 a path length dependent amount of light is observed for the three trigger positions **a**, **b**, and **c**, shown in the first and last row of Figure 8.11. The opposite readout side reveals consistent results.

8.3.1   Light Yield per Channel

The most probable values of the fitted Landau Gaussian function to the signal height spectra in Figure 8.11 are divided by the determined gain values for the corresponding channel, see Figure 8.8, to evaluate the number of detected photons for each channel of the second prototype. The results are

light yield per channel
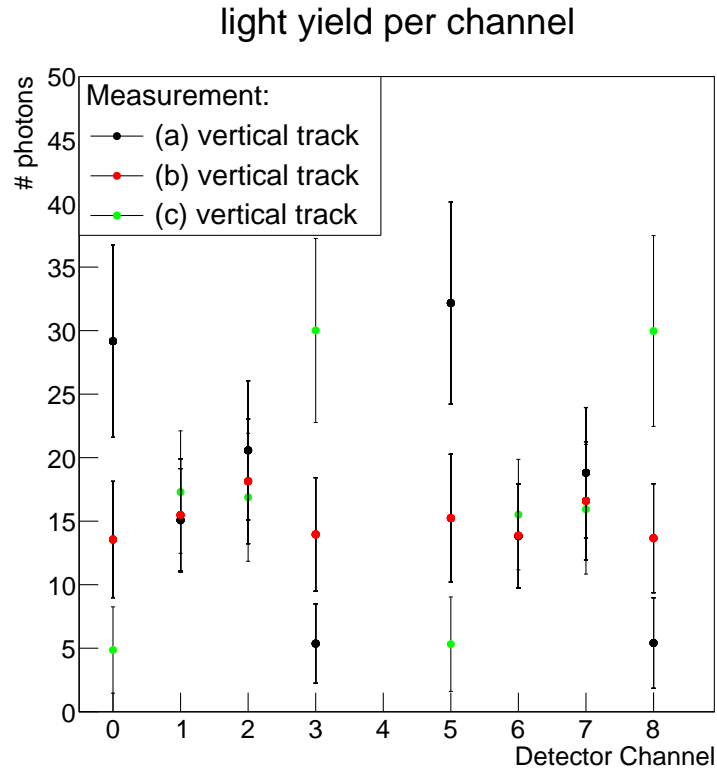
Figure 8.12: Detected amount of light for all channels of the second prototype: For Ch1, Ch2, Ch6, Ch7, connected to the thin base of each trapezoid, the detector reveals a detected number N of 17 photons and almost no variation due to the varying path length of trigger combinations **a**, **b** and **c**. The channels connected to the fiber located at the thick base of the trapezoid exhibit a path length dependent amount of light. The number of photons N ranges from 5 to 30 photons. In comparison to the first prototype, the mean number of detected photons is increased by a factor 3.5 per channel. Error bars for each light yield are calculated from $\sqrt{N}$.

displayed in Figure 8.12 for the vertical trigger positions **a**, **b** and **c** .

In the following discussion, the amount of detected light for each channel is compared with the results of the first prototype, see Figure 6.20 for the measurement with 120 GeV pions and Figure 6.30 for the measurement with cosmic muons.

The channels one and six located in trapezoid q_1 and two and seven located in trapezoid q_2 at the thin base of each trapezoid reveal a light yield of about 17 photons, whereby the fiber located in the trapezoid q_2 detects slightly more light. The variations between the trigger positions **a**, **b** and **c** are in the order of few photons, whereby the highest amount of photons is detected for the shortest path length in the corresponding scintillator. Thus, no path length dependent amount of light is observable. This behavior is comparable with the channels located at the thin base of the first prototype (channel zero and five) and the position insensitivity is in accordance with result for the first prototype detector. The channels zero and four in trapezoid q_1 and five and eight in trapezoid q_2 at the thick base of each trapezoid reveal a path length dependent light yield according to the trigger positions **a**, **b** and **c**.

For trigger position **b**, where the path length is similar in both trapezoids, about 15 photons are detected for all position sensitive channels.

For trigger positions of maximal path length in the corresponding trapezoid the light yield is in the order of 30 for all position sensitive channels. In contrast, for trigger positions with the minimal path length the amount of detected light is 5 photons for position sensitive channels.

The mean number of detected photons for position sensitive channels is enhanced by a factor 3.5. This factor is slightly lower than the expected value from the light enhancement studies described in

Chapter 7. By taking the double sided readout into account, the detected light yield for the position sensitive channel is increased by a factor 7, in comparison to the first prototype.

8.3.2   Detection Efficiency of Prototype II
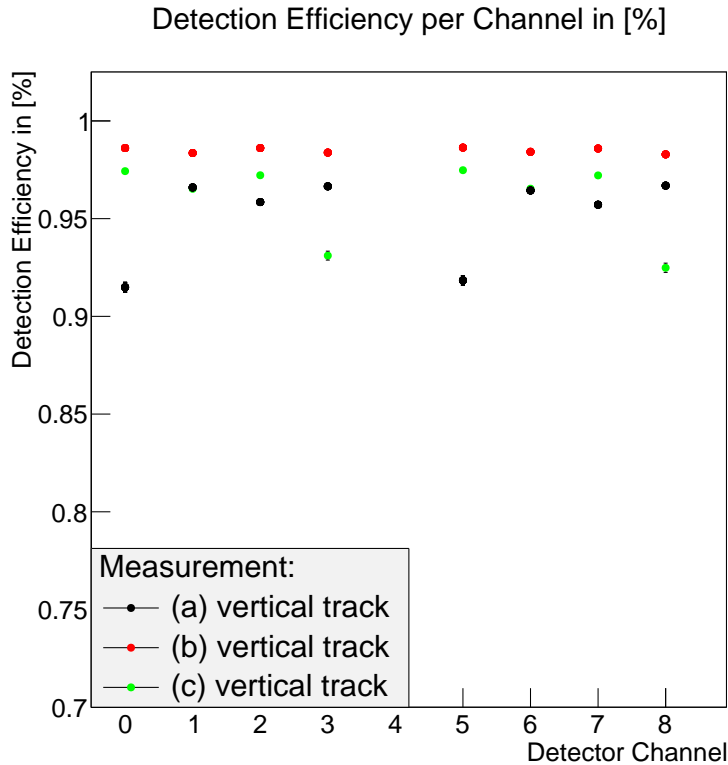
Figure 8.13: Detection efficiency of second POSSuMUS prototype: At least two detected photons are required to count. Due to the enhanced light yield the detection efficiency is for almost all channels and trigger positions above 95 % despite of the tighter criteria of at least two detected photons per event. Only for channels at the thick base of the trapezoid a drop below 95% is observable.

In Figure 8.13 the detection efficiencies for all channels and three trigger position **a**, **b** and **c** are plotted. The detection efficiencies and the error for the detection efficiencies are determined in the same manner as described in Section 6.5.2. In contrast to the first prototype, at least two detected photons per event are required. This is reasonable to reduce the influence of non light events, created by dark rate events in this measurement. The dark rate for two firing pixels is about 100 kHz and thus one order of magnitude smaller than for one firing pixel. Therefore, the probability for a measured non light event in the QDC-acquisition window of 45 ns reduces from 4.5% to about 0.45%.

Despite of the requirement of at least two detected photons per event, the detection efficiencies for all channels and trigger positions are above 90 %, because of the enhanced amount of detected light. In comparison to the detection efficiencies of the first prototype detector for 120 GeV pions. see Figure 6.22, and cosmic muons, see Figure 6.31, the results are comparable despite of different cut criteria. For position insensitive channels the detection efficiencies are always above 95 %, whereby the differences between several trigger positions arise from an imperfect coverage of the trigger scintillators for positions **a** and **c** with the sensitive area of the detector. Therefore the center position **b** has for sure the best coverage and therefore reveals the highest detection efficiencies of all channels.

For position sensitive channels one and six in trapezoid q_1, and three and seven in trapezoid q_2 the detection efficiencies are also above 95 % for the center position and for the maximal path length

position. Similar to the first prototype, see again Figure 6.22 and 6.31, a drop of the detection efficiency is observable for short path lengths in the corresponding trapezoids. The mean number of detected photons for this trigger and fiber-location combination is not sufficient despite of the enhanced amount of detected light.

8.3.3 Position Sensitivity of the Detector

Position Sensitive Fibers
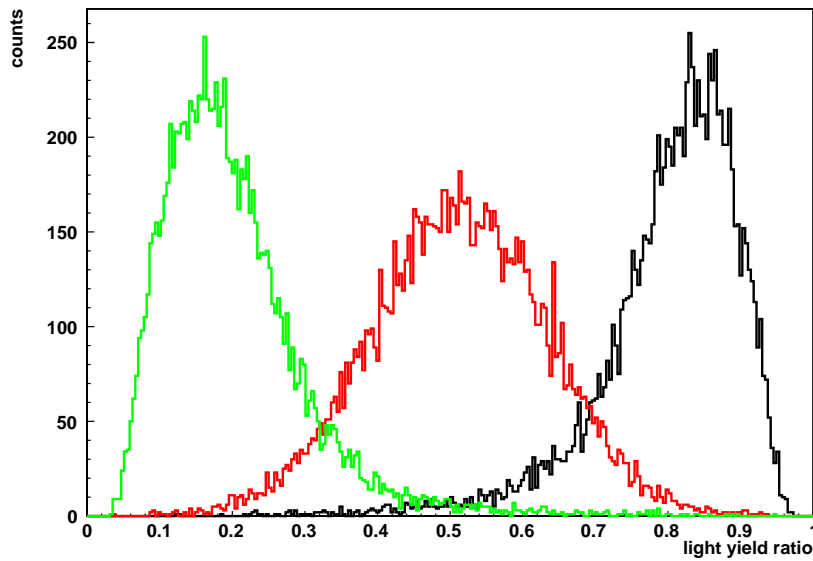
Figure 8.14: Light ratios for vertical tracks of trigger combinations **a**, **b**, and **c**: The position sensitivity of the detector is shown by the separation of the three distributions. The mean values and standard deviations are presented in Table 8.1.

The position sensitivity of the second prototype detector is determined in the same manner as described in Section 6.5.3, with the known equation for the light ratio:

$$\mathrm{pos(y)} \;=\; \frac{\mathrm{q_1(y)}}{\mathrm{q_1(y) + q_2(y)}} \tag{8.1}$$

whereby $\mathrm{q_1(y)}$ is the amount of detected light in trapezoid $\mathrm{q_1}$ and $\mathrm{q_2(y)}$ is the amount of detected light in trapezoid $\mathrm{q_2}$. The amount of detected light is determined by the light yield of the position sensitive channels at the thick base of each trapezoid, namely channels zero and five in trapezoid $\mathrm{q_1}$ and three and eight in trapezoid $\mathrm{q_2}$ to determine the position of traversing muons. The position insensitive channels are not included in the position determination.

In Figure 8.14 the light ratios for vertical tracks are displayed for trigger combinations **a**, **b** and **c**, indicated in Figure 8.10. The detector reveals its position sensitivity by the separation of the three light ratios $\mathrm{pos(y)}$. The mean value and the standard deviation for trigger position **b** is determined by the fit of a Gaussian distribution. For the asymmetric shape of the distributions for trigger positions **a** and **c** the Crystal Ball-Function is used, defined in Appendix A.3, to determine the mean value and the standard deviation, an example is presented in Figure 8.15. The asymmetric shape arises from the experimental setup, that the edges of trigger scintillator and detector are in overlap and the light ratios $\mathrm{pos(y)}$ is cut off due to the end of the detector.

The results of all fits are presented in Table 8.1, in combination with the detection efficiencies for the three vertical trigger combinations and the expected values for the path length ratio in both trapezoids, with the assumption of a linear correlation between path length and amount of detected light.
In the last column of Table 8.1 the detection efficiencies for three vertical trigger combinations are
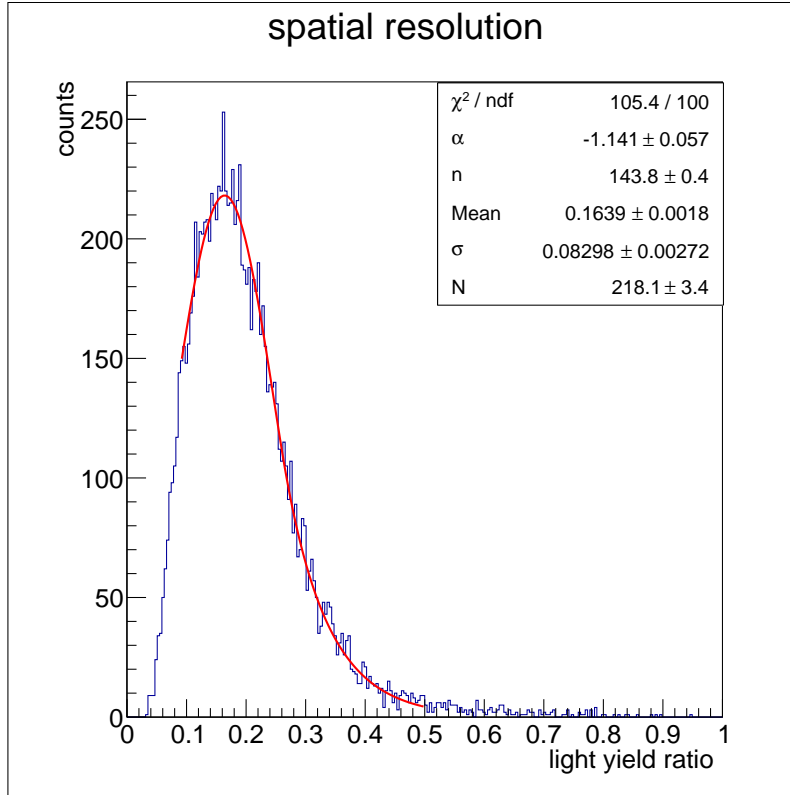
Figure 8.15: The crystal ball function is used to describe the asymmetric shape of the distribution of trigger combination **c**, and to determine the mean value and the standard deviation.

pos(y):	expected value	measured value	σ	detection efficiency
measurement **c**	0.27	0.16	0.08	89.2 %
measurement **b**	0.50	0.51	0.12	97.8 %
measurement **a**	0.73	0.85	0.09	87.5 %

Table 8.1: The expected values are presented for a linear correlation of the path length with the amount of detected light. In the second and third column the mean values and the standard deviation of the distributions in Figure 8.14 are shown. The expected values and the measured values differs due to a non linear correlation between path lengths in the trapezoid and amount of detected light. In the last column the detection efficiencies are displayed. The efficiencies for position **a** and **c** are smaller due to a drop in the detection efficiency when the muon crosses the detector at the thin base and the light is collected at the thick base of the trapezoid.

presented. As expected from the channel efficiencies in Figure 8.13, the highest detection efficiency is observed for trigger combination **b**. For trigger combinations **a** and **c** a drop in detection efficiency is observable because of the decreasing amount of detected light for muons traversing at the thin base of each trapezoid and the scintillation light is collected by the position sensitive channels at the thick base of the trapezoid.

In the second and third column the expected and measured values for the trigger combinations are presented. The measured value of the light ratio pos(y) of trigger combination **b** is 0.51 and corresponds to the expected value. Since the path length of crossing muons are equal in both trapezoids

and therefore the amount of detected light is similar for both trapezoids.

The measured values of the light ratio pos(y) for trigger combination **a** and **c** differ from the expected values for the light ratios with the assumption of a linear correlation between path length and amount of detected light.

This difference of expected and measured value for the light ratio pos(y) arises due to the non-linear
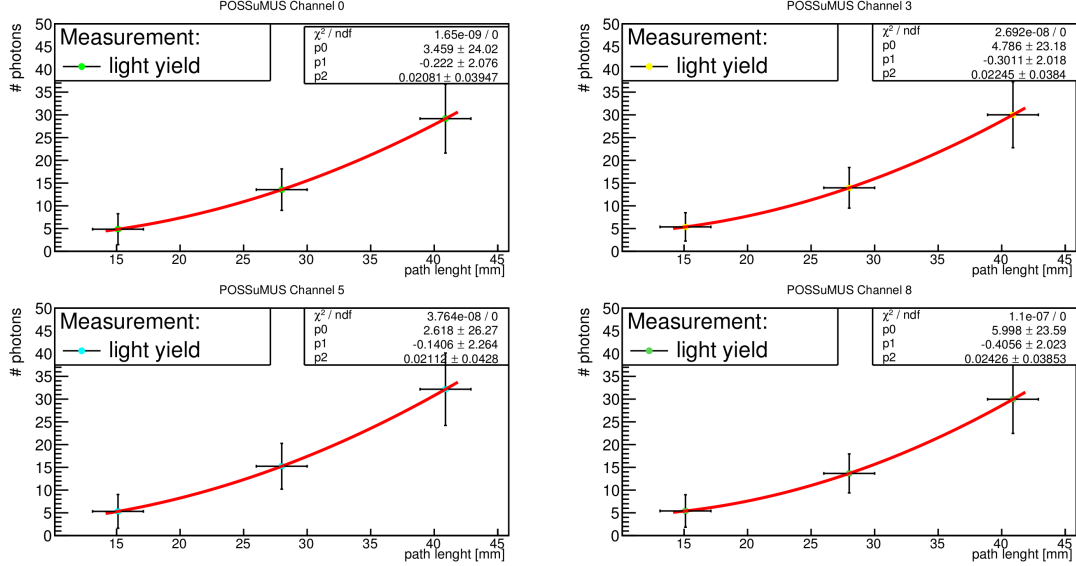
Figure 8.16: The amount of detected light for is displayed against the path length in the trapezoid for the position sensitive channels at the thick side of the trapezoid: To guide the eye a parabola fit is used to visualize the non-linear behavior of the amount of detected light.

correlation between path-length in the scintillator and amount of detected light.

This is presented in Figure 8.16, where the amount of detected light is plotted against the path length in both trapezoids for all position sensitive channels and the three trigger combinations **a** at $y = 12.5$ mm, **b** at y = 44 mm and **c** y = 75.5 mm. Due to the trigger width of 25 mm more data points are not possible. The error bars for the x-axis correspond to the width of the trigger scintillators. The error bars of the y-axis correspond to the standard deviation of the convoluted Landau Gaussian distribution in Figure 8.11. For visualizing the non-linearity of the amount of detected light the data points are connected by a quadratic function.

The path length x of vertical traversing muons can be described by using the following parametrization

$$x_{q_1(y)} = \text{offset} - (m \cdot y - a) \tag{8.2}$$

$$x_{q_2(y)} = \quad \text{offset} + m \cdot y \tag{8.3}$$

whereby:

- offset is the thickness of the thin base of the trapezoid (10 mm)

- a is the thickness at the thick side of the trapezoid (36 mm)

- m is the slope of the inclined side of the trapezoid (m = 0.41)

- y is the width of the detector, $y \in [0, 88\text{mm}]$

Therefore, the detected amount or light can be described by the following equations, 8.4 and 8.5, dependent on the path length of the muon in each trapezoid and a quadratic term to take the non-linear behavior into account, presented in Figure 8.16:

First for the upper trapezoid, the amount of detected light is q_1 :

$$q_1(y) \; = \; a_1 + b_1 \cdot x_{q_1} + c_1 \cdot (x_{q_1})^2 \tag{8.4}$$

and for the lower trapezoid, the amount of detected light is q_2 :

$$q_2(y) \; = \; a_2 + b_2 \cdot x_{q_2} + c_2 \cdot (x_{q_2})^2 \tag{8.5}$$

The light ratio pos(y) reads again:

$$pos(y) \; = \; \frac{q_1(y)}{q_1(y) + q_2(y)} \tag{8.6}$$

The constants in equation 8.4 and 8.5 are determined by the mean values of the parabola parameters for Channel 0 and Channel 5 in trapezoid q_1 and for Channel 3 and Channel 8 in trapezoid q_2 for a_1, b_1 and c_1, and a_2, b_2 and c_2, see Figure 8.16. In this calibration, the error bars are not taken into account. Therefore:

- $a_1 = 3.0$ $a_2 = 5.4$

- $b_1 = -0.18$ $b_2 = -0.35$

- $c_1 = 0.021$ $c_2 = 0.023$

The expected values of the light ratio pos(y) are calculated with the assumption of a quadratic rise of the amount of detected light with the path length. In Table 8.2, the expected values are presented together with the measured values. By using the calibration of the parabola fit values, the measured

pos(y):	expected value	measured value	σ
measurement **c**	0.15	0.16	0.08
measurement **b**	0.52	0.51	0.12
measurement **a**	0.85	0.85	0.09

Table 8.2: The expected values of the light ratio pos(y) are calculated with the assumption of a quadratic rise of the amount of detected light with the path length. The measured values correspond well to the expected values.

values pos(y) for the trigger combinations **a**, **b** and **c** corresponds well to the expected values of the light ratio pos(y).

With the assumed quadratic behavior of the amount of detected light, the range of values of the light ratio pos(y) is:

$$pos(y) \in [0.08, 0.90] \tag{8.7}$$

whereby $y \in [0, 88mm]$ and corresponds to the width of the detector.

A change of 1 mm in the y-direction of a vertical muon track corresponds a variation of 0.0093 for the value of the light ratio pos(y), therefore the standard deviation of 0.12 for trigger combination **b** corresponds to a spatial resolution of 12.9 mm. For trigger position **a** and **c** the standard deviations of the light ratio pos(y) corresponds to a spatial resolution of 9.7 mm and 8.6 mm.

In comparison with the first prototype the spatial resolution is almost a factor two better, see Table 6.3 in Section 6.6.

8.4 Position Sensitivity for Vertical and Inclined tracks

In Figure 8.17, the experimental setup for the investigation of vertical and inclined tracks are presented. In contrast to the first setup, see Figure 8.10, the trigger scintillators are tilted by $90°$. Hence, the coincidence area decreases for vertical tracks from $(250 \text{ mm})^2$ per trigger position to $(100 \text{ mm})^2$. The trigger scintillators are located at the central position of the detector (**B**) because of the symmetric position to both position sensitive fibers and equal path length in both trapezoids and 3 cm away from this center position for trigger position **A** and **C**. With this setup vertical and inclined tracks and the influence of the trigger module's width on the spatial resolution of the POSSuMUS detector are investigated. The event rate for cosmic muons is 0.09 Hz in total, this comprises inclined and vertical tracks, and a rate of 0.008 Hz for vertical tracks. Therefore the measurement time increases to at least two weeks to collect sufficient statistics for all possible trigger combinations. The inclined trigger combination are presented in Figure 8.19, 8.21 and 8.23. In the beginning only vertical tracks are
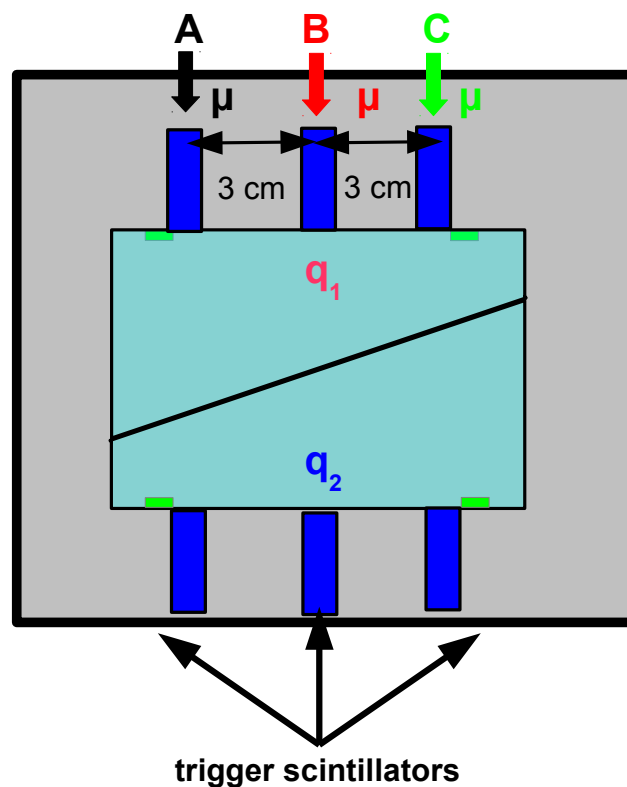
Figure 8.17: View from one readout side on the second prototype, located in a light tight box: The trigger detectors are tilted by $90°$ and the trigger position **B** is located at the center position of the detector, symmetric to both sensitive fibers and equal with path length in both trapezoids. The trigger scintillators for trigger combinations **A** and **C** are located 3 cm away from the central position. With this setup vertical and inclined tracks and the influence of trigger module's width on the spatial resolution are investigated.

investigated for this measurement. The light ratio pos(y) for traversing muons is determined in the same way as described in Section 8.3.3. Hence, only position sensitive channels at the thick base of the trapezoid are used. The expected value for the light ratio pos(y) are determined with the assumption of a quadratic correlation between the amount of detected light and the path length of cosmic muons in the trapezoid.

In Figure 8.18 the light ratio pos(y) is displayed for three different trigger combinations **A**, **B**, and **C**. The position sensitivity of the detector is visible by the separation of the distributions of pos(y). In Table 8.3 the expected values for the light ratio, the mean values and standard deviations for all
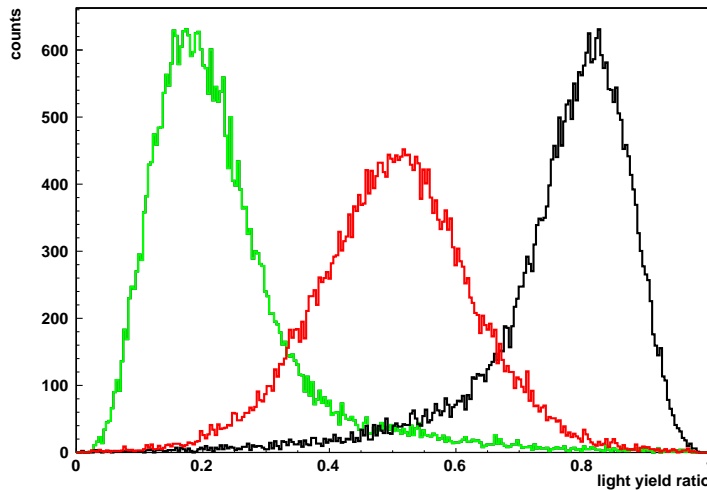
Figure 8.18: The Light ratios pos(y) for three trigger combination for vertical muon are presented, indicated by **A**, **B** and **C** in contrast to the first measurement the trigger width is 10 mm. This measurement investigates the influence of the trigger width on the spatial resolution of the detector.

three trigger combinations are presented, whereby the distribution of trigger position **B** is fitted by a Gaussian and trigger position **A** and **C** with the crystal ball function.

The measured values for all trigger combinations corresponds to the expected values for the light

pos(y)	expected position	mean-value	standard deviation	detection efficiency
measurement **A**	0.16	0.18	0.08	92.6%
measurement **B**	0.51	0.49	0.12	98.1%
measurement **C**	0.84	0.81	0.07	91.9%

Table 8.3: The expected values of the light ratio for a quadratic behavior of the amount of detected light are presented, in combination with the measured values for trigger combinations **A**, **B**, and **C** and the standard deviation. In the last column the detection efficiencies are presented.

ratio pos(y). The spatial resolution reveals similar results as for the experimental setup with trigger scintillators of 25 mm. The spatial resolution for the center position is about 12.9 mm, whereby the position resolution for the outer trigger positions are 8.6 mm for **A** and and 7.5 mm for **C**. The influence of the trigger width on the spatial resolution is not observable. Hence, one conclusion is that the observed resolution corresponds to the intrinsic spatial resolution of the detector. This observation needs to be further investigated.

The detection efficiency for trigger combination **B** is in the same order as for the first measurement, see Table 8.3. The detection efficiencies for trigger combinations **A** and **C** are slightly higher due to trigger positions, which lead to a higher amount of detected light, due to a longer path length within the scintillator.

8.4.1 Position Sensitivity for Inclined Muon Tracks

Beside the presented trigger combinations for vertical tracks of cosmic muons also inclined tracks can be investigated. In the following section all possible trigger combinations with different inclination angles are investigated.

First Set of Inclined tracks
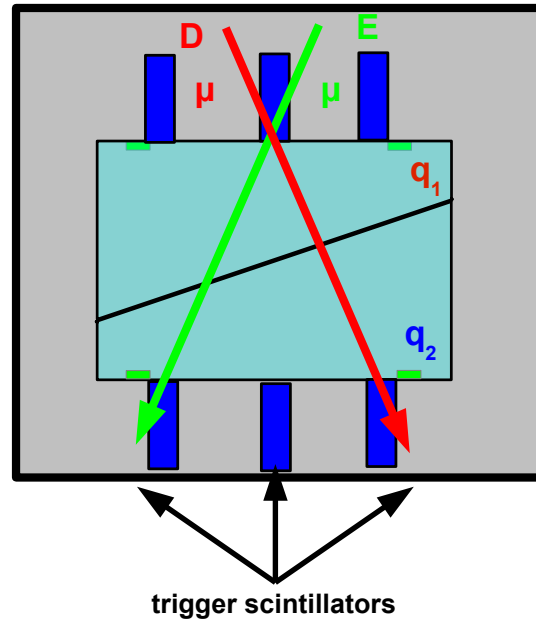
Figure 8.19: View from one readout side on the second prototype for the investigation of inclined tracks: The trigger combinations **D**, and **E** have the same inclination angle and of 29°. Therefore, the sum of path lengths in both trapezoids is equal. The path length in both trapezoids are different for both trigger combination. Hence the value of the light ratio pos(y) are not symmetric.

The first set of trigger combinations for inclined tracks is displayed in Figure 8.19, named as trigger combinations **D** and **E**. The triggered muons crossed the central trigger module on top of the detector and either the lower left trigger module or the lower right trigger module. The inclination angle for both trigger combinations is 29° Due to the same inclination angle, the sum of path lengths in both trapezoid is equal for both trigger combinations. In contrast, the path lengths in trapezoid q_1 and in trapezoid q_2 are different for both trigger combinations respectively. Therefore, the expected values for the light ratio pos(y), see Equation 8.1, reveal non-symmetrical values with respect to the position **B** with the expected value of 0.5.

In Figure 8.20 the light ratio pos(y) for the mentioned trigger combinations **D** and **E** are presented. The mean values and the standard deviation are determined by the fit of a Crystal ball function and presented in Table 8.4 as measured values. The position sensitivity of the POSSuMUS Detector for inclined muon tracks is observable, by the separation of the light ratios for both trigger combinations. Therefore, the detector concept to determine the position of traversing muons, because of the path length dependent amount of detected light in both trapezoids is also proven for inclined tracks. The expected values for the light ratios corresponds to the measured values within the error of the standard deviation. The position resolution is in the same order of magnitude as for vertical tracks. Thus, the spatial resolution is about 12 mm. The detection efficiencies for both inclined tracks are in the same order of magnitude as for vertical tracks, whereby the low value for trigger combinations **E** arises, because of the shorter path length in the upper trapezoid q_2 and a track farer away from the collecting fiber.
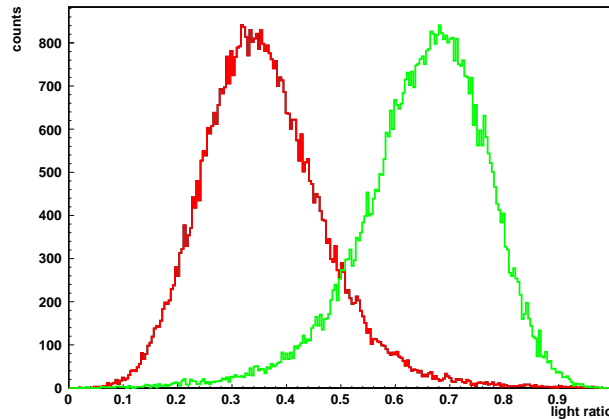
Figure 8.20: The position sensitivity of the POSSuMUS detector for inclined tracks is shown by the separation of the light ratio pos(y) for trigger combinations **D** and **E**. Both trigger combinations have the same inclination angle of 29°, but due to different path lengths in the trapezoids the light ratios pos(y) are not symmetrically located to each other.

pos(y)	expected positions	mean-value	standard deviation	detection efficiency
measurement **D**	0.34	0.34	0.10	95.4%
measurement **E**	0.76	0.68	0.11	85.4 %

Table 8.4: Light ratios for trigger combinations **D**, and **E**. The expected values of the light ratio for a quadratic behavior of the amount of detected light are presented, in combination with the measured values for trigger combinations **D**, and **E** and the standard deviation. In the last column the detection efficiencies are presented. The inclination angle is 29° for both tracks.

Second Set of Inclined Tracks

The second set of trigger combinations is formed by either the left or the right trigger module located on top of the detector and the central trigger module below the detector, named as trigger combination **K** and **L**, indicted in Figure 8.21. The inclination angle for both trigger combinations is again 29°. The distributions of the light ratios pos(y) for trigger positions **K**, and **L** are presented in Figure 8.22. The mean values and standard deviations are determined for both trigger combinations by the fit of a Crystal ball function and presented with the expected values in Table 8.5. The measured positions

pos(y)	expected positions	mean-value	standard deviation	detection efficiency
measurement **K**	0.69	0.67	0.10	95.0%
measurement **L**	0.25	0.32	0.10	92.7%

Table 8.5: Light ratios pos(y) for trigger combinations **K**, and **L**. The inclination angle is 29° for both tracks. The expected values of the light ratio for a quadratic behavior of the amount of detected light are presented, in combination with the measured values for trigger combinations **K**, and **L** and the standard deviations. In the last column the detection efficiencies are presented.

of the mean value are close to the expected values. The spatial resolution is in agreement with the previous results. The detection efficiency for both trigger positions **K** and **L** is in the expected order of magnitude.
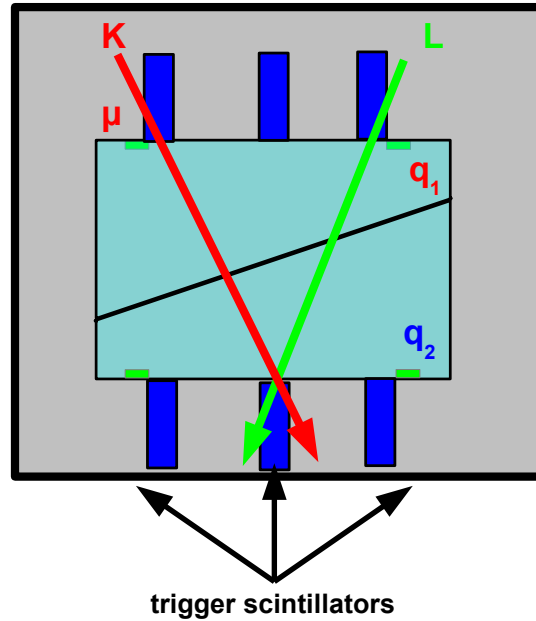
Figure 8.21: View from one readout side on the second prototype for the investigation of inclined tracks: The trigger combinations **K**, and **L** have the same inclination angle of 29°. Therefore, the sum of path lengths in both trapezoids is equal. The path length in both trapezoids are different for both trigger combination. Hence the value of the light ratio pos(y) are not symmetric to each other.
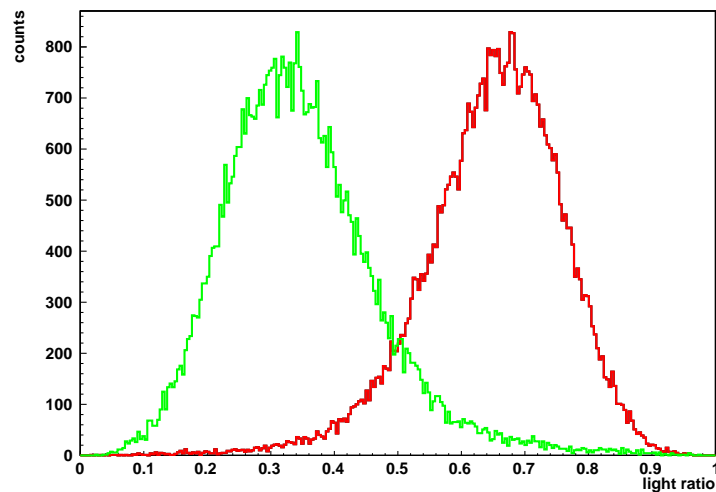
Figure 8.22: The position sensitivity of the POSSuMUS detector for inclined tracks is shown by the separation of the light ratio pos(y) for trigger combinations **K** and **L**. Both trigger combinations have the same inclination angle of 29°, but due to different path lengths in the trapezoids the light ratios pos(y) are not symmetrically located to each other.

The Third Set of Inclined Tracks

The third set of investigated inclined muon tracks is presented in Figure 8.23 and has an inclination angle of 49° . The first trigger combinations is formed by the left trigger module on top of the detector and by the right trigger module below the detector and is named as **G**. The other trigger
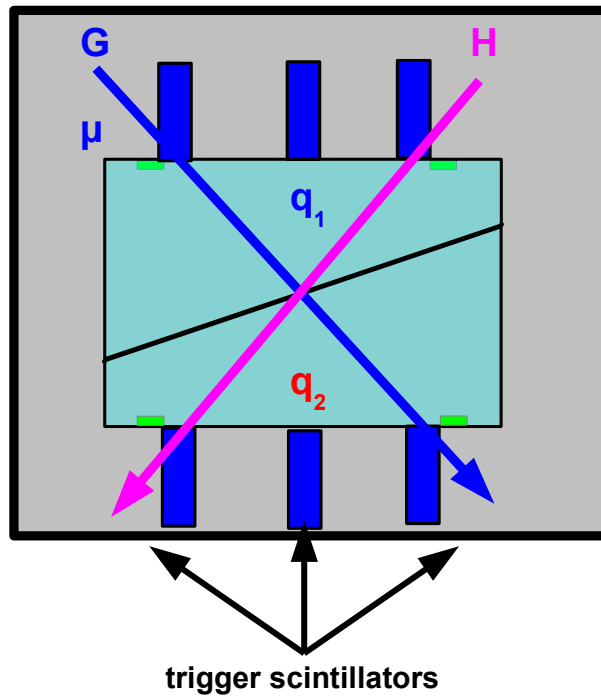
Figure 8.23: View from one readout side on the second prototype for the investigation of inclined tracks: The trigger combinations **G**, and **H** have the same inclination angle of 49°. Therefore, the sum of path lengths in both trapezoids is equal. Due to the symmetry, the path Length in both trapezoids are equal, this is valid for both trapezoids. Therefore the value of the light ratio pos(y) is expected to be 0.5.

combination is formed by the right trigger module on top of the detector and by the left trigger module below the detector and is named **H**.
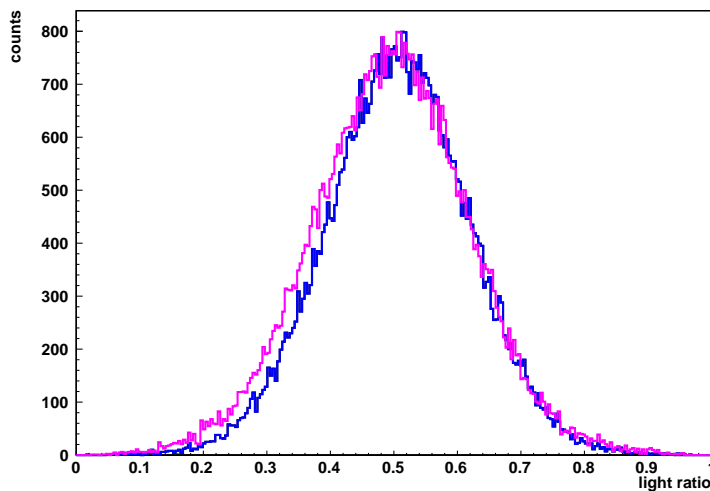
Figure 8.24: Position sensitivity of inclined tracks of 49°. Both trigger combinations lead to equal path length in trapezoid q_1 and q_2. When calculating the light ratio of both trapezoids the value 0.5 is expected.

In Figure 8.23 the light ratio pos(y) for both trigger combinations **G** and **H** are presented. The mean value and standard deviation is determined by a Gaussian fit to the distributions. The measured values for the light ratio pos(y) are displayed in Table 8.6 together with the standard deviation and the detection efficiency. Both tracks are symmetric to each other and have the same path length in

pos(y)	expected values	mean-value	standard deviation	detection efficiency
measurement **G**	0.51	0.51	0.11	97.3 %
measurement **B**	0.51	0.50	0.12	98.2 %
measurement **H**	0.51	0.49	0.12	94.9 %

Table 8.6: The expected light ratio is 0.5 because of equal path length in both trapezoids. The influence of the quadratic light behavior cancels out due to the symmetry to both light collecting fibers. The position sensitivity of the POSSuMUS detector for inclined tracks is shown by the overlap of the light ratio pos(y) for trigger combinations **G**, and **H**. Both trigger combinations have the same inclination angle of 49° and due to the symmetry the path length is equal in both trapezoids for both trigger combinations.

both trapezoids. Moreover, the tracks are symmetric in both trapezoid, meaning that they are both either closer to the position of the sensitive fiber or farer away. Due to the same path length in both trapezoids the expected value for the light ratio, see Equation 8.6, is 0.5. Therefore these trigger combination are comparable with the vertical track **B** discussed in the previous section 8.3.3, where the path length in both trapezoid is also identical.
As expected from the equal path length in both trapezoids, the determined mean value corresponds to expected value of 0.5. The effects of the non linear behavior of amount of detected light cancel out for both tracks due to symmetric configuration. The spatial resolution is again around 13mm, as expected from the previous results. The detection efficiencies are comparable with the value of trigger combination **B**.

Chapter 9

Summary and Outlook

In this thesis the development of the POSSuMUS detector concept is presented. POSSuMUS is a scintillation detector with silicon photomultiplier (SiPM) readout, capable to determine the position of traversing particles in two dimensions and suitable for large area applications. The detector consists of two trapezoidal shaped scintillators which form one rectangular module. The scintillation light is collected by wavelength shifting (WLS) fibers and the amount of light is measured by SiPMs. The concept is based on a modular system, hence combining several detectors allows for large area applications (up to m^2) with few readout channels. Hence, POSSuMUS provides a cost effective detector concept.

The thesis starts with detailed studies on the characterization of SiPMs. Important properties of SiPMs, like the breakdown voltage U_{bd} and the temperature dependent variation of U_{bd} are determined with a self developed characterization setup. In addition, in the course of this work a multiple voltage source for SiPMs with automatic gain stabilization is developed. This system provides stable gain conditions for measurements with SiPMs in a temperature changing environment over a period of weeks.

The first POSSuMUS detector is tested during a beam time with 120 GeV pions at CERN in 2012. A position sensitivity of the detector is shown for two space dimensions. In the transverse y-direction along the trapezoidal geometry, the position is determined due to the path length dependent amount of light collected in both trapezoids. The position sensitivity is observable over the whole detector area. The spatial resolution in y-direction is in the order of 20 mm. In the perpendicular x-direction along the scintillator, a position sensitivity is observable due to the propagation time of light. The spatial resolution for the x-direction is about 10 cm and is mainly limited by the propagation of light in the scintillator.

After the proof of principle by the first prototype test, the development of the detector concentrated on the enhancement of the amount of detected light per event. For this purpose, several aspects like wrapping material of scintillators, WLS-fiber positions and coupling of WLS-fiber and SiPM are investigated. Implementing the results of these studies in the construction of the second prototype an increase of the detected light of at most a factor of 4.2 is expected.

The second prototype of the POSSuMUS detector is investigated with cosmic muons, whereby stable SiPM gain conditions are provided by the mentioned multiple automatic voltage source. The amount of detected light per event is enhanced by a factor of 3.5 in comparison to the first prototype. A position sensitivity in y-direction due to the ratio of detected light in both trapezoids is observed, for straight and in contrast to the first prototype also for inclined tracks. The spatial resolution is in the order of about 13 mm, significantly improved with respect to the first prototype.

At this stage of development the POSSuMUS detector concept can be further investigated by an experiment with a localized beam of minimum ionizing particles allowing to gain larger insight in the properties of the detector such as spatial resolution and detection efficiency.

The next step in the development of the POSSuMUS concept is to combine several modules of the de-

tector for a large area detector and measure for example the small angle scattering of cosmic muons in the Cosmic Ray Facility in Garching [28]. The spatial resolution in y-direction is sufficient to resolve the small angle scattering of cosmic muons in an energy range from 1 GeV to 9 GeV, see Table 1.1. In x-direction the spatial resolution is in the order of 10 cm and therefore the small angle scattering of cosmic muons with energies larger than 1 GeV cannot be resolved with the present design. Another application is the combination of a POSSuMUS detector with a large area precision detector, where the POSSuMUS detector provides trigger information with a two dimensional position information for the detector under test.

For a further improvement of the detector properties it is essential to increase the amount of detected light per event. For this purpose, the area for collecting scintillation light can be increased. This can be achieved by positioning several WLS-fibers beside each other or one uses wavelength shifting bars of appropriate size. Another aspect to be investigated is the variation of the trapezoidal geometry of the scintillator for a more favorable geometry. Using larger area for collecting scintillation light, the spatial resolution in x-direction can be slightly improved. By maximizing the detected amount of light per event and optimizing the trapezoidal geometry the spatial resolution due the light ratio (y-direction) can be further improved by approximately a factor of two.

Bibliography

[1] TL 200. *Data Sheet for DC power Supply TL200.* 2014.

[2] arduino. *Arduni Uno.* www.arduino.cc, 2014.

[3] M. Balkanski and R.F. Wallis. *Semiconductor Physics and Applications.* Springer Verlag, 1994.

[4] W.H. Barkas and M.J. Berger. *Nuclear science series report 39.* 1964.

[5] J.B. Birks. *The Theory and Practise of Scintillation Counting.* Pergamon Press Ltd, 1964.

[6] A. Bollu. *Characterization of silcion photomultiplier noise and optimazation of light detection through coupling wiht optical fibers.* Bachelor Thesis, LMU, 2014.

[7] P. Buzhan and B. Dolgoshein. *An advanced Study of Silicon Photomultiplier.* IFCA Instrumentation Bulletin, 2001.

[8] J. Caron. *The LHC injection complex.* LHC-PHO-1993-008, CERN, 1993.

[9] CERN. www.atlas.ch/detector.html, 2014.

[10] CERN. hilumilhc.web.cern.ch/HiLumiLHC/index.html, 2014.

[11] CMS Collaboration. *CMS Physics : Technical Design Report Volume I: Detector Performance and Software.* Tech. Des. Rep. CERN-LHCC-2006-001, CERN, 2006.

[12] ALICE collobaration. *ALICE : Technical proposal for A Large Ion Collider Experiment at the CERN LHC.* LHC Tech. Proposal CERN-LHCC-95-71, CERN, 1995.

[13] ATLAS Collobaration. Tech. Des. Rep. CERN-LHCC-96-042, CERN, 1996.

[14] ATLAS Collobaration. *ATLAS liquid argon calorimeter: Technical Design Report.* Tech. Des. Rep. CERN-LHCC-96-041, CERN, 1996.

[15] ATLAS Collobaration. *ATLAS inner detector: Technical Design Report.* Tech. Des. Rep. CERN-LHCC-97-016, CERN, 1997.

[16] ATLAS Collobaration. *The ATLAS experiment at the CERN LHC.* JINST, 3:S08003, 2008.

[17] ATLAS Collobaration. *Observation of a new particle in the search for the standard model higgs boson with the ATLAS detector at the LHC.* Phy. Lett. B, 716(1):1-29, 2012.

[18] ATLAS Collobaration. *New small wheel Technical Design Report.* Tech. Des. Rep. CERN-LHCC-2013-006, CERN, 2013.

[19] CMS Collobaration. *Observation of a new new boson at a mass of 125 GeV with the CMS Experiment.* Phy. Lett. B, 716(1):1-30, 2012.

[20] LHCb collobaration. *LHCb Technical Design Report.* Tech. Des. Rep. CERN-LHCC-2006-004, CERN, 1998.

[21] LHCf Collobaration. *LHCf experiment: Technical Design Report. Proposal.* CERN-LHCC-2006-004, CERN, 2006.

[22] MoEDAL Collobaration. *Technical Design Report of the MoEDAL Experiment.* Tech. Des. Rp. CERN-LHCC-2009-006, CERN, 2009.

[23] TOTEM Collobaration. *Total cross section, elastic scattering and diffraction dissociation at thr Large Hadron Collider at CERN.* TOTEM Technical Design Report Tech. Des. Rep. CERN-LHCC-2004-002, CERN, 2004.

[24] Laser Component. *FC connector system.* www.lasercomponents.com, 2014.

[25] Laser Component. *Polishing Disc FC.* www.lasercomponents.com, 2014.

[26] S.M. Sze C.R. Crowell. *Temperature Dependence of Avalanche Multiplication in Semiconductors.* Applied Physics Letters 9, 1966.

[27] Analog Devices. *digital potentiometer AD5263.* Analog Devices, 2014.

[28] Biebel et al. *A Cosmic Ray Measurement Facility for ATLAS Muon Chambers.* arxiv-physics0307147, 2003.

[29] J. E. Gaiser. *Charmonium spectroscopy from radiative decays of the $\frac{J}{\psi}$ and ψ^0.* PhD thesis, Stanford Linear Accelerator Center, Stanford University, August 1982.

[30] Carl Roth Gmbh. *optical grease, Siliconöl M 500000.* datasheet, 2014.

[31] Eletkro-Automatik GmbH. *Laboratory Power Supply Series PSI 8000 T.* Eletkro-Automatik GmbH, 2011.

[32] Saint Gobain. *Data Sheet for BC 400.* www.crystals.saint-gobain.com, 2014.

[33] Saint Gobain. *Data Sheet for BC 600.* www.crystals.saint-gobain.com, 2014.

[34] Saint Gobain. *Data Sheet for WLS Fiber BCF 98.* www.crystals.saint-gobain.com, 2014.

[35] J. Grossmann. *Optimization of a scintillation detector with wave length shifting fibres and SiPM readout.* Master Thesis LMU in preperation, supervised by the author, 2014.

[36] Hamamatsu. *Hamamatsu MPPC S12571-050C.* www.hamamatsu.com, 2012.

[37] Hamamatsu. *Hamamatsu MPPC S12572-100C.* www.hamamatsu.com, 2012.

[38] Hamamatsu. *Hamamatsu R4124.* www.hamamatsu.com, 2012.

[39] Infineon. *Data Sheet for BGA 614.* www.infineon.com/, 2011.

[40] Brüning O. Collier P. Lebrun P. Myers Ostojic R. Poole J. and Proudlock P. editors. *LHC Design Report Vol. I - The LHC main Ring.* Report CERN-2004-003-V-1. CERN, 2004.

[41] Brüning O. Collier P. Lebrun P. Myers Ostojic R. Poole J. and Proudlock P. editors. *LHC Design Report Vol. II - The LHC infrastructure and general services.* Report CERN-2004-003-V-2. CERN, 2004.

[42] Brüning O. Collier P. Lebrun P. Myers Ostojic R. Poole J. and Proudlock P. editors. *LHC Design Report Vol. III - The LHC injector chain.* Report CERN-2004-003-V-3. CERN, 2004.

[43] J.Bortfeldt. *Development of floating Strip Micromegas Detectors.* Phd thesis, Ludwig Maximilians Universität, 2014.

[44] Keithley. *Model 2400 General-Purpose SourceMeter.* www.keithley.de, 2012.

[45] Keithley. *Model 6514 Programmable Electrometer.* www.keithley.de, 2012.

[46] O. Kortner. *Schauerproduktion durch hochenergetische Myonen und Aufbau eines Höhenstrahlungsprüfstandes für hochauflösende ATLAS Myonkammern.* Phd thesis, Ludwig Maximilians Universität, 2002.

[47] L. Landau:. J.Phys (USSR) 8,201, 1944.

[48] W. Leo. *Techniques for Nuclear and Particle Physics Experiments.* Springer Verlag, 1994.

[49] Memmert. *Climate Chamber ICH 256.* 2012.

[50] R. Müller. *Development of a Position Sensitive Scintillating Muon Detector with Silicon Photo Multiplier Readout.* Mater Thesis, LMU, supervised by the author, 2013.

[51] EPOTEK 353 ND. *EPOTEK 353 ND.* www.epotek.com, 2014.

[52] O.Biebel. *'Physik der Teilchendetektoren'.* Lecture, Ludwig Maximilians Universität, 2010.

[53] M. E. Oreglia. *A study of the reactions* $\psi^0 \mapsto \gamma\gamma\psi$. PhD thesis, Stanford Linear Accelerator Center, Stanford University, December 1980.

[54] Silicon Oxid. *DS18B20 Programmable Resolution 1-Wire Digital Thermometer.* www.dalsemi.com, 2014.

[55] BC-620 Reflector Paint. *Data Sheet for BC-620 Reflector Paint for Plastic Scintillators.* www.crystals.saint-gobain.com.

[56] PDG. *Radiation Length of Iron.* pdg.lbl.gov/2011/AtomicNuclearProperties/, 14.9.2014.

[57] PDG. *Stopping Power od positive muon in copper.* www.pdg.lbl.gov, 14.9.2014.

[58] K. Prothmann. *Comparative Measurements of Silicon Photomultipliers for the Readout of a Highly Granular Hadronic Calorimeter.* Diploma thesis, Technische Universität München, 2008.

[59] F. Rauscher. *Untersuchung des Verhaltens von Driftrohren bei starker Bestrahlung sowie Vermessung von Driftrohrkammern mit Hilfe von Myonen der kosmischen Hohenstrahlung.* Phd thesis, Ludwig Maximilians Universität, 2005.

[60] D. Renker. *Geiger mode avalanche photodiodes, history properties and problems.* NIM 567, 2006.

[61] A. Ruschke. *Spatial resolving SiPM-detector for cosmic muons.* PoS(EPS-HEP 2013)045, 2013.

[62] P. Schwegler:. *High-Rate Performance of Muon Drift Tube Detectors.* Phd thesis, Technische Universität München,, 2014.

[63] Dallas semiconductor. *DS18B20 Programmable Resolution 1-Wire Digital Thermometer.* www.dalsemi.com, 2014.

[64] M.J. Berger: S.M. Seltzer. *Studies in the Penetration of Charged Particles in Matter.* National Acadamy of Sciences Publication 1133, Nuclear Science Series Report No. 39, 1964.

[65] C. Soldner. *Scintillator Tile Uniformity Studies for a Highly Granular Hadron Calorimeter.* Diploma thesis, Technische Universität München, 2009.

[66] CAEN S.p.A. *Technical Information Manual Mod. N108A, Dual Delay.* www.caen.it, 2010.

[67] CAEN S.p.A. *Technical Information Manual Mod. N625, Fan In Fan Out.* www.caen.it, 2010.

[68] CAEN S.p.A. *Technical Information Manual Mod DS2477 LED driver,.* www.caen.it, 2011.

[69] CAEN S.p.A. *Technical Information Manual Mod. N844/N844P/N845, Low Threshold Dircriminator.* www.caen.it, 2012.

[70] CAEN S.p.A. *Technical Information Manual Mod. N93B Dual Timer.* www.caen.it, 2012.

[71] CAEN S.p.A. *Technical Information Manual Mod V1729 Sampling ADC.* www.caen.it, 2012.

[72] CAEN S.p.A. *Technical Information Manual Mod. V775N Time to Digital Converter (TDC).* www.caen.it, 2012.

[73] CAEN S.p.A. *Technical Information Manual Mod. V792 QDC, Charge to Digital Converter (QDC).* www.caen.it, 2012.

[74] CAEN S.p.A. *Technical Information Manual Mod. V814, programmable Low Threshold Discriminator.* www.caen.it, 2012.

[75] CAEN S.p.A. *Technical Information Manual Mod. V977 I-O register.* www.caen.it, 2012.

[76] R.M. Sternheimer and R.F. Peierls. *General expression for the density effect for the ionization loss of charged particles.* Phys. Rev. B, 3(11):3681-3692, 1971.

[77] struck innovative systems. *SIS 3100.* www.struck.de/pcivme.htm, 2014.

[78] BC 642 PTFE Reflector Tape. *Data Sheet for BC 642 PTFE Reflector Tape.* www.crystals.saint-gobain.com, 2014.

[79] Tektronics. *Data sheet fot AFG3000C.* tek.com, 2012.

[80] Tyvek. *Tyvek material.* www.tyvek.de, 2012.

[81] T.O. White. *Scintillating Fibers.* NIM A273, 1988.

[82] A. Zibell:. *High-Rate Irradiation of 15 mm Muon Drift Tubes and Development of an ATLAS Compatible Readout Driver for Micromegas Detectors.* Phd thesis, Ludwig Maximilians Universität, 2014.

Appendix A

A.1 Middle Position and Right Position
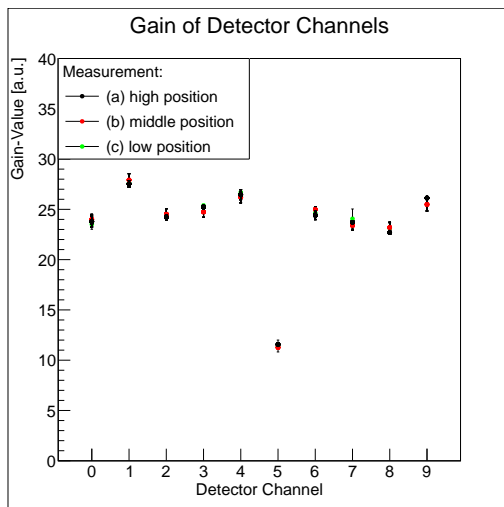
Figure A.1: Determined gain values for three measurement points at the center of the first POS-SuMUS detector.
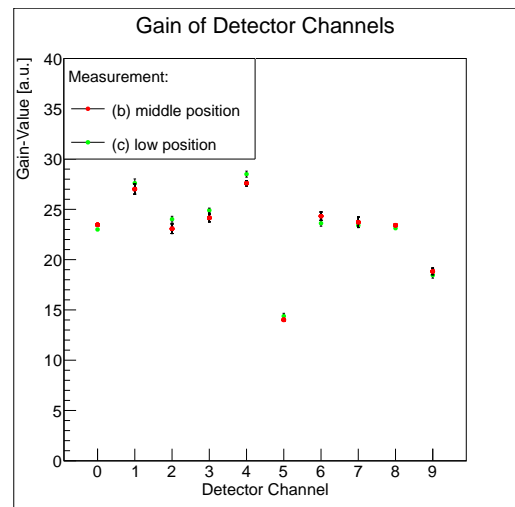
Figure A.2: Determined gain values for two measurement points at the right edge of the first POS-SuMUS detector.
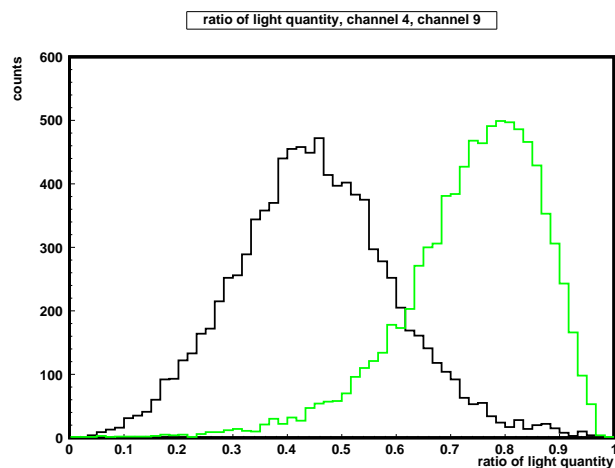
Figure A.3: Position sensitivity of the first POSSuMUS prototype at the left edge of the Detector: At this detector side only two measurement points were recorded. The position sensitivity is also visible for this detector position with reference to the beam.

A.2   QDC readout for Cosmic Measurement with POSSuMUS I
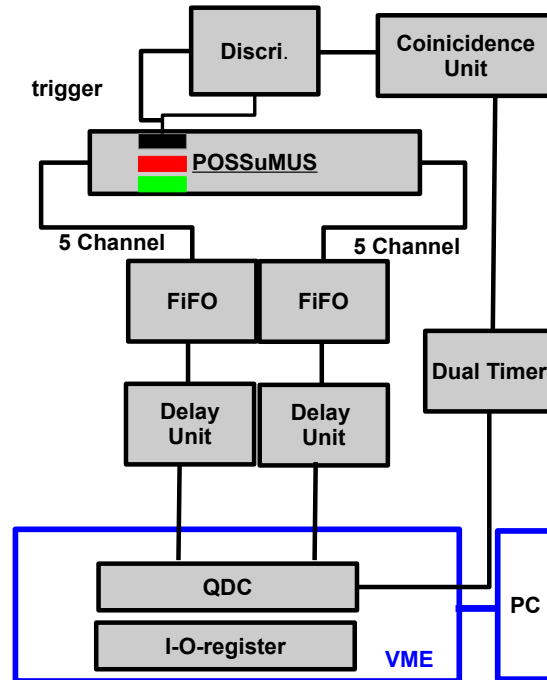
Figure A.4: Schematic for the QDC-readout for the test of the first POSSuMUS prototype with cocmis muon

The principle of an QDC-readout is explained by Figure A.4. This data acquisition system is used for the test of the first Prototype detector with cosmic muon. All ten signal of the POSSuMUS Prototype are given to a Linear Fan In Fan out [67] and then to delay Unit. Here the Signal are delayed to fit in the QDC-data acquisition gate, which ich created by the dual timer, when a muon crosses on of the trigger combinations **a**, **b** and **c**. The QDC-data are readout by the VME-system and recorded at a PC.

In Figure A.5 the determined gain values are presented for the measurement of the first prototype detector with cosmic muons.
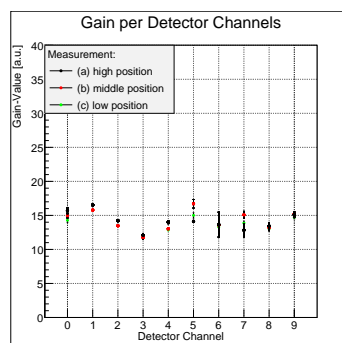
Figure A.5: Determined gain values for all Channels of POSSuMUS I for the Cosmic muon measurement, the gain values are determined by fitting a Gaussian distribution to the peaks and calculating the difference. Channel 5, which had shown a malfunction for test with 120 GeV pions, no shows normal behavior

A.3 Crystal Ball Function

The Crystal Ball function, named after the Crystal Ball Collaboration (hence the capitalized initial letters), is a probability density function commonly used to model various lossy processes in high-energy physics. It consists of a Gaussian core portion and a power-law low-end tail, below a certain threshold. The function itself and its first derivative are both continuous. The Crystal Ball function is given by: [53] [29]

$$
f(x; \bar{x}, \sigma, \alpha, n, S) = S \cdot \begin{cases} \exp(-\frac{(x-\bar{x})^2}{2\sigma^2}, & \text{for } \frac{x-\bar{x})}{\sigma} > \alpha \\ A \cdot (B - \frac{x-\bar{x})}{\sigma})^{-n}, & \text{for } \frac{x-\bar{x})}{\sigma} \leq \alpha \end{cases} \tag{A.1}
$$

where

$$
A = (\frac{n}{|\alpha|})^n \cdot \exp(-\frac{|\alpha|^2}{n}) \tag{A.2}
$$

$$
B = \frac{n}{|\alpha|} - |\alpha| \tag{A.3}
$$

The Crystal ball function is used for fitting the asymmetric distributions which arises at the edge of the detector, an determine the spatial resolution for this trigger positions.

The Crystal Ball function with an exponential correction factor below or above a certain value of the parameter α:

- Positive values of α corresponds to an exponential correction on the lower tail of the Gaussian distribution.

- Negative values of α corresponds to an exponential correction on the the upper tail of the Gaussian distribution.

The parameter n controls the rate of decay. Both the function and its derivative are continuous.

A.4 Peltier Cooling Aluminum Box

Example for the cooling process for the measurements for enhancing the detected amount of light.
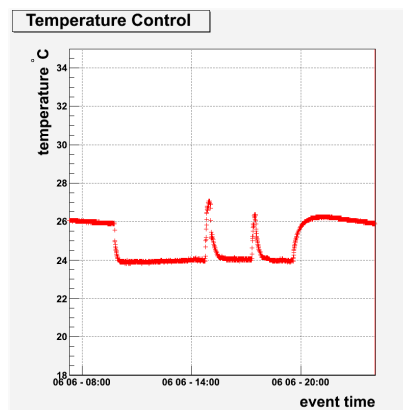
Figure A.6: Example of the Peltier cooling system for one day of measurment

List of Figures

List of Tables

Appendix B

Acknowledgments

Am Ende meiner Doktorarbeit will ich mich bei allen bedanken, die mich bis hierher begleitet haben, leider kann ich nicht alle erwähnen, aber an euch gedacht ist auf jeden Fall:

- bei Otmar Biebel, der mir die Möglichkeit und das Vertrauen gegeben hat eine Promotion mit einem eigenen Thema zu beginnen und die Arbeit mit großem Freiraum selbst zu gestalten.

- bei Thomas Nunnenmann, der mich im ersten Jahr meiner Promotion betreut hat.

- bei Dorothee Schaile, dass ich an ihrem Lehrstuhl promovieren konnte.

- bei Wolfgang Dünnweber für das erstellen des Zweitgutachtens.

- bei Katia Parodi und Jochen Weller für die Teilnahme an meiner Prüfungskommission.

- bei Ralf Hertenberger, für die vielen lehrreichen Lektionen, Ratschläge und seinen Humor in den letzten 5 Jahren.

- bei Atilla Varga, für die unendlich vielen Kabel, Platinen und die ausdauernden Gepräche über Fußball.

- bei der mechanische und elektronischen Werkstatt, für die Unterstützung beim Bau von POS-SuMUS.

- bei Frank Simon und Christian Soldner vom MPI für das Überlassen der ersten SiPMs und die Starthilfe am Beginn meiner Promotion.

- bei meinen fast 5-jährigen Bürogenossen Jona Bortfeldt für die unglaublich vielen Witze und Diskussionen im Büro und bei Andre Zibell für die vielen Zigarettenpausen, Gedanken und Erklärungen.

- bei meinen beiden Masteranden, Ralph Müller und Johannes Grossmann, die mit mir gemeinsam POSSuMUS in den letzten 3 Jahren entwickelt habe.

- bei dem Rest der Hardware-Gruppe von Anfang bis zum Ende, Albert Engl, Nicola Tyler, Philipp Lösel, Samuel Moll, Helge Danger, Bernard Fierl und Elias Pree.

- bei dem Rest des Lehrstuhls für die gute Atmosphäre und die gemeinsamen Aktivitäten während meiner Zeit in Garching.

- bei meiner WG, für das Vorträge anhören und das ertragen meiner schlechten Laune, speziell am Ende meiner Doktorarbeit.